Title
Dynamics of H{sub 2} Elimintation from Unsaturated Hydrocarbons

Author
Cromwell, E.F.

Publication Date
1991-02-01

LBL-30363

Lawrence Berkeley Laboratory
UNIVERSITY OF CALIFORNIA

Materials & Chemical
Sciences Division

Dynamics of H_2 Elimination from Unsaturated Hydrocarbons

E.F. Cromwell
(Ph.D. Thesis)

February 1991

Prepared for the U.S. Department of Energy under Contract Number DE-AC03-76SF00098

DISCLAIMER

LBL-30363

DYNAMICS OF H_2 ELIMINATION FROM UNSATURATED HYDROCARBONS

Evan Francis Cromwell

Department of Chemistry
University of California

and

Chemical Sciences Division
Lawrence Berkeley Laboratory
Berkeley, CA 94720 USA

February 1991

This work was supported by the Director, Office of Energy Research, Office of Basic Energy Sciences, Chemical Sciences Division, of the U.S. Department of Energy under Contract No. DE-AC03-76SF00098.

DYNAMICS OF H_2 ELIMINATION FROM UNSATURATED HYDROCARBONS

by

Evan Francis Cromwell

Abstract

State-of-the-art laser and molecular beam techniques are used to study the dynamics of H_2 elimination from 1,4-cyclohexadiene and ethylene. Information on the transition state configurations and the dynamics of the dissociation processes for these reactions is reported. A brief introduction to these studies is presented in Chapter I.

An ultrahigh-brightness laser system, developed to study the spectroscopy and dynamics of molecules and clusters from the vacuum ultraviolet (VUV) and extreme ultraviolet (XUV) to the near infra-red spectral regions is described in Chapter II. The laser utilizes pulse amplification of a single-mode ring dye laser, frequency doubling, and four-wave mixing in a pulsed jet. Pulse energies of >120mJ in the visible, >35mJ in the uv, >15mJ in the infra-red, and $>10^{11}$ photons/pulse in the VUV-XUV have been obtained. The bandwidth of the laser has been measured to be 91MHz in the visible and 210MHz in the XUV.

In Chapter III a comprehensive study of the dynamics of H_2 elimination from 1,4- and 1,3-cyclohexadiene is reported.

Rotational and vibrational quantum state distributions as well as translation energy distributions for the H_2 product are measured. State specific detection of H_2 is accomplished with a transform limited vuv-xuv laser system via (1+1) REMPI. Rate constants for the H_2 elimination and 1,4 to 1,3 isomerization reactions are derived. A (v,J) correlation for H_2 with $\mathbf{v} \| \mathbf{J}$ primarily is observed from anisotropy in the Doppler profiles. A clear picture of the transition state configuration of 1,4-cyclohexadiene is provided from the information obtained.

A study of the dynamics of H_2 elimination from ethylene is presented in the last Chapter. A complete H_2 product energy distribution is obtained. The distribution of energy in H_2 product from the dissociation of 1,1-d_2 ethylene is also presented. Two separate H_2 elimination channels are observed, a 1,1 elimination and a 1,2 elimination, in the dissociation of C_2H_4. Differences in the vibrational, rotational and translational energies for these two channels are extracted. The D atom elimination from C_2D_4 is examined and kinetic energy distribution for this product is measured.

TABLE OF CONTENTS

LIST OF TABLES

LIST OF FIGURES

Chapter IV.

Perhaps my closest collaborations over the years have been with Marc Vrakking. I have benefitted greatly from his attention to minute details, which can make or break an experiment, and from his ability calculate nth order polynomials in his head (can you say polynomial?). All those trips to Roma/Strada to discuss the happenings of the world were very beneficial and needed diversions. It has also been great fun to watch the Batmachine come together. I wish you the best of luck with your experiments.

I have also had the pleasure of working with some excellent post-docs. Di-Jia Liu, with whom I did the cyclohexadiene experiment, was always a hard worker and a source of many stimulating discussions. Albert Stolow has been my most recent collaborator. Over the summer of '90 we were able to get H_2 detection down to an art. The exciting results from the ethylene experiments are due in a large part to his work and ideas (and to Flint's). Albert is one of the most creative thinkers that I have worked with. I hope those ideas pay off for you in the future.

There are many other Lee groupies whom I will miss. The beer drinking/softball playing/chaos talking trio of John Price, Jim Myers and Matt Côté were a source of many hours of amusement. My old and new office mates, Gil Nathanson, Eric Hintsa, and Deon Anex, were always willing to answer questions or get into lengthy discussions at a moments notice. I would also like to thank Pam, Barb, Bob

C., Floyd, Doo Wan, Kim and any others that I have not mentioned for making my years at Berkeley enjoyable. A special note to the first years: Allan, Simon and Laura. There is light at the end of the proverbial tunnel!

No acknowledgement from the Lee group would be complete with out the necessary homage to the person who keeps everything rolling, Ann Weightman. I appreciate everything that you have done for me over the past four and a half years. Congratulations on your marriage and I wish you a happy early retirement.

The person most responsible for this thesis is my father. He made my education one of his top priorities and provided me opportunities to excel. I will always be grateful for his support. The last note of appreciation goes to my wife, Mary. Since we met that fateful Friday at the keg my graduate career has been much happier. We both suffered through disappointments but I think we are the better for it. Your loving support has helped me keep my scientific life in perspective. To 126 more years.

Oh, and by the way, this work was supported by the Director, Office of Energy Research, Office of Basic Energy Sciences, Chemical Sciences Division, of the U.S. Department of Energy under Contract No. DE-AC03-76SF00098.

CHAPTER I

INTRODUCTION

Over the past thirty years progress in the realm of experimental chemical physics has been dominated by two factors: the development of molecular beams and the advent of novel laser light sources. The technology behind molecular beams and the theory of supersonic expansions had been worked out long before this time but it was not until the 1960's that scientists began applying these methods towards the study of chemical reaction dynamics. Since that time many others have joined in the application of molecular beams to various areas of chemical physics.[1,2] The advantages offered by an atomic or molecular beam are well documented.[3] A major one of these advantages is that by crossing an atomic or molecular beam with a second such beam, or with a beam of photons, one can study single reactive events. In addition, the rotational and vibrational cooling of molecular species in a supersonic expansion allows a much better determination of the initial conditions in a reaction as well as clears out much of the congestion that is normally present in molecular spectra.

The development of lasers for use in studying chemical systems is a somewhat different story. The potential uses of a powerful, tunable, coherent light source for spectroscopy as well as studies of reaction dynamics was immediately realized. However, the experiments had to wait while the technology became available not only to generate the light at the needed wavelengths but also to be able to

adequately control that light whether it be temporally or spectrally. Advances in laser light sources since the development of the Ruby laser have been significant.[4] Lasers are now available with temporal widths from a continuous output down to a laser with pulses 6 femtoseconds in duration. One can vary the wavelength nearly continuously from the far infra-red to the extreme ultraviolet and even into the soft x-ray region. The maximum energies commercially available range up to >1 joule/pulse and/or $>1x10^{14}$ watts and experimental systems can deliver >10 kJ/pulse. Even more promising light sources will soon be available with the advent of free electron lasers and the development of new solid-state lasers.

The experiments to be described in the following chapters combine both state-of-the-art laser systems and molecular beams. A laser system was developed in order to be able to generate nanosecond pulses of high power radiation with a transform limited frequency bandwidth that would be tunable from the near infra-red to the extreme ultraviolet.[5] The applications of this system, varying from high resolution spectroscopy to probing products from chemical reactions, are tremendous. In conjunction with the laser system a molecular beam chamber was set-up with a high through-put pulsed valve[6] that would maximize the signal-to-noise obtainable for any given experiment. Care was taken through out the set-up of the experimental apparatus

to make sure that the highest sensitivity could be realized for any experiment that might be undertaken.

I. LASER SOURCES

Techniques used for the generation of vacuum ultraviolet (vuv) light (106nm to 200nm) and extreme ultraviolet (xuv) light (<106nm) have been improved greatly over the past ten years. The first methods utilized discharge lamps filled with helium, xenon or other gases.[7] The Helium-Hopfield continuum lamp was probably the most widely used of these. While these sources emitted significant fluxes of photons the light was not coherent and the resolution achievable was limited to that of traditional vacuum monochromators. Typically bandwidths of approximately 1Å were used. The intensity of the usable light suffered greatly going to higher resolutions.

Laser sources in the vuv region came about primarily with the development of non-linear mixing techniques. A main reason for this is that there are numerous difficulties in trying to make a laser whose fundamental operating frequency is in the vuv. Possibly the most stringent requirement is finding appropriate molecular or atomic emission lines for which a population inversion can be achieved. All lasing mediums to date in the vuv have been gaseous. This means that the medium will have to be

contained by a chamber with windows. The choice of window materials in the vuv is very limited and can be very expensive. Complications arise from the need for good transmission and potential corrosion of the windows. Once a possible lasing transition has been isolated then an efficient means of pumping the gain medium has to be found. For a VUV laser this is generally either an electron beam or an electric discharge. The reason for this is that the photon energy, or frequency, of the pump needs to be greater than the frequency of the laser; flashlamps, or other pump sources, often do not produce enough intensity at these short wavelengths. For a practical "laboratory" laser an electric discharge is the only reasonable pumping scheme. When it is not possible to sustain a uniform discharge in the lasing medium an electron beam is the only other alternative.

The most common lasers to operate in the vuv are the F_2 and ArF excimer lasers whose fundamental frequencies are 157nm and 193nm respectively. While good powers can be obtained with these systems they are very limited as far as tunability and generally have a broad frequency bandwidth. It is possible to shift the output of excimer lasers using Stokes and Anti-Stokes Raman processes which extends the range of frequencies that they can cover.[8,9,10,11] Another type of vuv laser which has been reported is an anti-Stokes Raman shifted laser.[12] This laser utilizes group VI atoms

(in particular Se) and requires a two laser pumping scheme. In a typical laser of this type a 193nm photon is used to dissociate COSe which creates a population inversion in the Se product. A second laser, a tunable "pump" laser, extracts gain at the anti-Stokes shifted frequency of that laser. This system has produced radiation at 158.7nm and 167.5nm. There has also been published reports by Stoicheff et. al. which describe a pulsed discharge Ar_2 excimer laser which produced 20mJ of radiation at 126nm.[13]

A more attractive technique for generating coherent short wavelength radiation is to start with visible and/or infra-red lasers and then use frequency upconversion to get into the vuv. For example, if one started with a pulsed dye laser operating with Rhodamine 640 dye at 600nm (16,667cm^{-1}) then by frequency doubling in a KDP crystal and frequency tripling in Argon gas one would be able to obtain laser radiation at 100nm (100,000cm^{-1}). This light would have nearly the same characteristics both spectrally and temporally as the initial laser pulse. Another method besides four-wave-mixing that is effective for generating short wavelength radiation is anti-stokes stimulated Raman scattering in H_2 gas mentioned above. This is most effective when the pump laser is an excimer or a frequency quadrupled Nd:YAG laser.

The biggest disadvantage of the above techniques is that they are inherently inefficient. Straight tripling in

rare gases rarely exceeds conversion efficiencies of 10^{-5}. This can be greatly enhanced through the use of resonant mixing but that tends to limit the tunability of the system to the width of the resonance which for atomic systems can be on the order of the bandwidth of the laser. Raman scattering is more efficient, especially for the first few anti-Stokes orders which can be up to 5% efficient, but this is only line tunable. In order to get to 130nm by anti-Stokes Raman shifting an ArF excimer laser in H_2 gas one must get to the 7th or 8th order. At this point the efficiency is not much better than resonant four wave mixing. However, if one started with an F_2 excimer (which are commercially available with outputs of 100mJ) much larger powers should be obtainable at the shorter wavelengths.

Two key aspects behind the design of the laser system reported in Chapter II of this thesis were versatility and reliability. The tremendous amount of time, effort and resources that went into the development and construction of the system dictated that it should not be a "single experiment" laser. Similarly, the complexity of the apparatus meant that all the components would have to be extremely reliable in order for experiments to be done on any reasonable time scale. The laser needed to be an experimental tool, not an experiment itself.

The basic philosophy behind the system was to start with a continuous wave (cw) single-mode ring dye laser pumped by an Argon ion laser to provide narrowband, tunable laser radiation throughout the visible spectrum with good spatial characteristics and beam quality. This would then be pulsed amplified through a series of dye amplifier cells which would provide a high power, transform limited bandwidth pulse which retained the beam quality of the original source. The combination of both good beam quality and power would allow the use of non-linear mixing techniques with high efficiency to generate ultra-narrow bandwidth radiation from the near infra-red to the extreme ultraviolet.

When it was possible, proven commercial equipment was utilized in the design. The cw ring dye laser (Coherent 699-29), while finicky at times, is powerful instrument for generation of tunable narrowband radiation. The flashlamp pumped Nd:YAG (Quantel 581C), used as the pump source for the amplifier chain, is perhaps the most reliable source for high power pulsed energy in the near infra-red or the visible. Since there was no commercially available amplifier chain at the time the laser was built that met the desired specifications regarding overall output power and beam quality a "home-built" system was designed. This system used a series of prism dye cells, modeled after a system built by R. Falcone,[14] to pulse amplify the cw beam.

While many of the techniques utilized in this system had been developed previously, no one had combined them all into a single laser system.

II. CHEMICAL APPLICATIONS

The possible applications of the laser system described above towards the study of chemical systems are wide and varied. The author himself has been a part of projects which involved looking for new molecular species (H_4), probing the hyper-fine splitting in Kr,[15] preparing state-specified ions (N_2^+),[16] high-resolution photoionization spectroscopy of H_2O,[17] and high-resolution overtone spectroscopy of Benzene.[18] One of the capabilities of the system as a whole that has been developed over the past years is the ability to detect H_2 with an extremely high sensitivity. The measured detection sensitivity of the laser/ion detection system is $\approx 10^4$ molecules/state/cm^3 within the bandwidth of the laser (210 MHz in the XUV). At the time of this writing this is the highest known sensitivity for detection of H_2.

The method of H_2 detection involves (1+1) resonance enhanced multi-photon ionization (REMPI) of H_2[19] followed by extraction of the H_2^+ through a 1m time-of-flight mass spectrometer and detection by a Daly type ion detector. The resonant transitions used in the REMPI scheme are from

specific (v",J") levels of the H_2 ground electronic state, $X^1\Sigma_g^+$, to specific (v',J') levels of either the $B^1\Sigma_u$ or $C^1\Pi_u$ excited electronic states of H_2. These single photon transitions lie in the VUV to XUV region of the spectrum. The residual uv light from the four-wave mixing process which generates the resonant radiation is used as the ionizing photon source in the (1+1) REMPI. The ion optics are believed to collect the generated H_2^+ with near unit efficiency. The ion detector is sensitive enough to detect a single ion transported through the t.o.f mass spectrometer.

With the tremendous capability of highly sensitive state-specific H_2 detection it was natural to probe the internal energy distribution in H_2 product from various reactions. Initial attempts were made to observe H_2 formed from the reaction of hot H atoms with HI. This reaction was accomplished in a single molecular beam of HI by dissociating a fraction of the HI in the beam to create H atoms with high kinetic energy which would then collide with the residual HI and react. H_2 product was observed and its rotational and vibrational energy distribution was measured. However, it was determined that this product came from reactions occurring in large clusters of HI. The amount of H_2 rotational energy was less than that measured by CARS in separated experiments[20] which is in accord with observations from Wittig's group that product rotational

energy is cooled when reactions occur in clusters.[21]

There are many interesting experiments that can be done with clusters. However, one of the limitations of experiments involving neutral clusters has been the inability to categorize the size of the clusters being studied. The pulsed valve used in the experiments described here can produce neutral clusters, $(A)_n$, of a known size that are well separated temporally in the molecular beam for up to n=3 or 4.[22] This opens up many possibilities for studying the properties of clusters of a specific size.

With the failure of the H+HI experiment to yield any measurable non-cluster dependent H_2^+ signal we chose to study a unimolecular reaction which would produce H_2. A prime candidate for this was 1,4-cyclohexadiene (CHDN). It was shown in previous experiments that there was a single H_2 elimination channel in the unimolecular decomposition of 1,4-CHDN.[23] There was also a fair amount of data already accumulated about this reaction.[24] Using the laser and molecular beam system described in this thesis the rotational and vibrational energy distribution in the H_2 product from this reaction was measured. In addition, the distribution of H_2 translational energy in each quantum state was measured through the Doppler profiles associated with each transition scanned. The results of this study are presented in Chapter III of this thesis.

The state-specific probing of H_2 product provides a very detailed, "microscopic" look at the dynamics of the reaction process. The previous experiments, which involved photo-fragment translational energy spectroscopy, gave a much more "macroscopic" look at the H_2 elimination process. These two experiments are very complementary. They not only fill in missing pieces of information that the other experiment is not able to gain but they also provide checks on the interpretation of the experimental data. The ability to compare results between these experiments, not only for the 1,4-CHDN work but also for the ethylene project,[25] was invaluable in forming a clear picture of the dynamics involved in the reaction processes.

The results of the cyclohexadiene experiment provided information about the concerted elimination of H_2 from an unsaturated hydrocarbon through a 6-centered transition state. The six "centers" involved are the 3 and 6 H's and the four carbons (C_6-C_1-C_2-C_3 or C_3-C_4-C_5-C_6) which complete the reactive ring structure found in the transition state region of this concerted decomposition. The next molecule studied, ethylene, provided an opportunity to observe H_2 formed from the dissociation of an unsaturated hydrocarbon via both a 3-centered and a 4-centered elimination channel. The results of this experiment are given in Chapter IV of this thesis.

The study of the decomposition of ethylene provided several challenges. The first was the absorption cross section of C_2H_4 at 193nm ($<10^{-19}cm^2$). It was not known whether one could dissociate enough C_2H_4 so that sufficient H_2 would be generated in order to measure the vibrational and rotational energy distribution of the H_2 product. A further complication arose from the presence of two channels for the formation of H_2: the 3-centered 1,1 elimination and the 4-centered 1,2 elimination. There were doubts whether the rotational, vibrational, and/or translational energy imparted into the H_2 product from the two channels would be significantly different enough to allow resolution of these channels with the expected signal to noise ratio of experiment. As related in Chapter IV, the experimental set-up was improved to the extent that full coverage of the H_2 (v",J") distribution was possible and the various energy distributions clearly indicate the presence of the two H_2 elimination channels.

III. SUMMARY

The question should be asked whether any trends are observable in the pattern of energy distribution in the reactions reported in this thesis. If one were to estimate how the amount of H_2 translational energy gained would vary from a 3-centered to a 6-centered reaction complex one might

expect it to decrease, given comparable ΔH's and total energies available for the reactions, because the product molecules would be formed farther away from each other. In a concerted decomposition, the release of translational energy is dominated, in general, by the repulsive potential energy between the closely placed product molecules. If the products are formed farther away from each other they should feel less repulsion and gain less kinetic energy. This is not the case for the decompositions of 1,4-CHDN and C_2H_4 where the kinetic energy for H_2 formed from 1,4-CHDN is higher than that of H_2 formed from C_2H_4. This shows that there are many other complicating factors involved, such as involvement of excited electronic states and the formation of high energy intermediates, in determining how energy is released in a given reaction. These complexities make comparisons between the different reactions based on the size of the reaction centers less fruitful.

A more useful comparison to make with the data obtained is to high level calculations of the structures found in the transition state regions for each of these reactions. The measurement of the distribution of energy in the H_2 product from a given reaction provides a wealth of information about the critical configuration at the transition state of that reaction. Translational energy helps determine the distance between the product molecules formed, vibrational energy indicates the H-H distance in the critical configuration,

and rotational energy gauges the anisotropy in the repulsion between the two H atoms from the transition state region. For 1,4-CHDN such a calculation has already been done and is reported in Chapter III.[26,27] There is very good agreement between the calculated transition state structure and the structure expected from the experimental results. Hopefully a similar calculation for the transition states of ethylene will be forthcoming.

REFERENCES

1. R.B. Bernstein, Chemical Dynamics Via Molecular Beam and Laser Techniques (Oxford University Press, New York, 1982).

2. Y.T. Lee, Science **236**, 793 (1987).

3. G. Scoles, Ed., Atomic and Molecular Beam Methods, Vol. 1 (Oxford University Press, New York, 1988).

4. See Conference on Lasers and Electro Optics, 1989 Technical Digest Series, Vol. 7 (Optical Society of America, Washington D.C., 1990).

5. E. Cromwell, T. Trickl, Y.T. Lee, and A.H. Kung, Rev. Sci. Inst. **60**, 2888 (1989).

6. D. Proch and T. Trickl, Rev. Sci. Inst. **60**, 713 (1989).

7. C.Y. Ng, Molecular Beam Photoionization Studies of Molecules and Clusters, Adv. Chem. Phys. **52**, 263 (1983).

8. H.F. Döbele and B. Rückle, Appl. Opt. **23**, 1040 (1984).

9. G.F. Faris, M.J. Dyer, W.K. Bischel, D.L. Huestis, "VUV Stimulated Raman Scattering of and ArF Laser in D_2 and HD," CLEO 1989 Technical Digest Series, Vol. 7 (Opt. Soc. Am., Washington D.C., 1990), pg. 268.

10. D.J. Brink and D. Proch, J. Opt. Soc. Am. **73**, 23 (1983).

11. T.R. Loree, R.C. Sze, D.L. Barker, and P.B. Scott, IEEE J. Quantum Elec. **QE-15**, 337 (1979).

12. H. Welling, K.Ludewigt, H. Schmidt, T. Dierking, and G. Wellegehausen, Laser Spectroscopy VII, **Proc. 7th Int. Conf. on Laser Spec.**, Eds. T.W. Hänsch and Y.R. Shen (Springer-Verlag, New York, 1985), pg. 183.

13. T. Efthimiopoulos, B.P. Stoicheff, and R.I. Thompson, Opt. Lett. **14**, 624 (1989).

14. R. Falcone, private communication.

15. T. Trickl, M.J.J. Vrakking, E. Cromwell, Y.T. Lee, and A.H. Kung, Phy. Rev. A **39**, 2948, (1989).

16. T. Trickl, E.F. Cromwell, Y.T. Lee, and A.H. Kung, J. Chem. Phys. **91**, 6006 (1989).

17. M.J.J. Vrakking, (to be published)?

18. D.-J. Liu, A. Stolow, M.J.J. Vrakking, E.F. Cromwell, A.H. Kung, and Y.T. Lee, (to be published).

19. A.H. Kung, T. Trickl, N.A. Gershenfeld, and Y.T. Lee, Chem. Phys. Lett. **144**, 4795 (1989).

20. P.M. Aker, K.D. Tabor, G.J. Germann, and J.J. Valentini, J. Chem. Phys. **90**, 4795 (1989).

21. S. Buelow, M. Noble, G. Radhakrishnan, H. Reisler, C. Wittig, and G. Hancock, J. Phys. Chem. **90**, 1015 (1986).

22. A. Stolow, E.F. Cromwell, Y.T. Lee, (to be published).

23. X. Zhao, R.E. Continetti, A. Yokoyama, E.J. Hintsa, Y.T. Lee, J. Chem. Phys. **91**, 4118 (1989).

24. See references in Chapter III.

25. B. Balko, J. Zhang, and Y.T. Lee, (to be published).

26. M. Page, private communication.

27. K.N. Houk, private communication.

CHAPTER II

VUV-XUV LASER SYSTEM

I. INTRODUCTION

The intent of this chapter is to describe in some detail the different components of the vuv-xuv laser system that is utilized in the experiments reported in this thesis.[1] The basic technique used in the construction of this laser system is pulse amplification of a single-mode dye laser. This approach was first demonstrated by Salour[2] using a nitrogen laser as the pump laser. Megawatt power in the visible was later achieved using the second harmonic of a Nd:YAG laser as the pump source.[3] The initial design of the laser system described below was done by A.H. Kung. Where possible, proven (and reliable) commercial systems were utilized in order to minimize the amount of development time. The main, non-commercial unit in the system is the dye amplifier chain which was assembled and tested by the author. A schematic of one leg of the laser system is shown in Figure 1. The complete system consists of two, nearly identical, such subsystems for generating visible radiation.

This chapter will be divided into two parts. In the first section a description of the individual components of the laser system will be given. There are five lasers utilized by the system as well as a variety of non-linear optical mixing techniques. A brief account of each of the lasers (their lasing mediums, resonator configurations, etc.) and other specifics of the laser system operation will be presented. References will be given which will hopefully

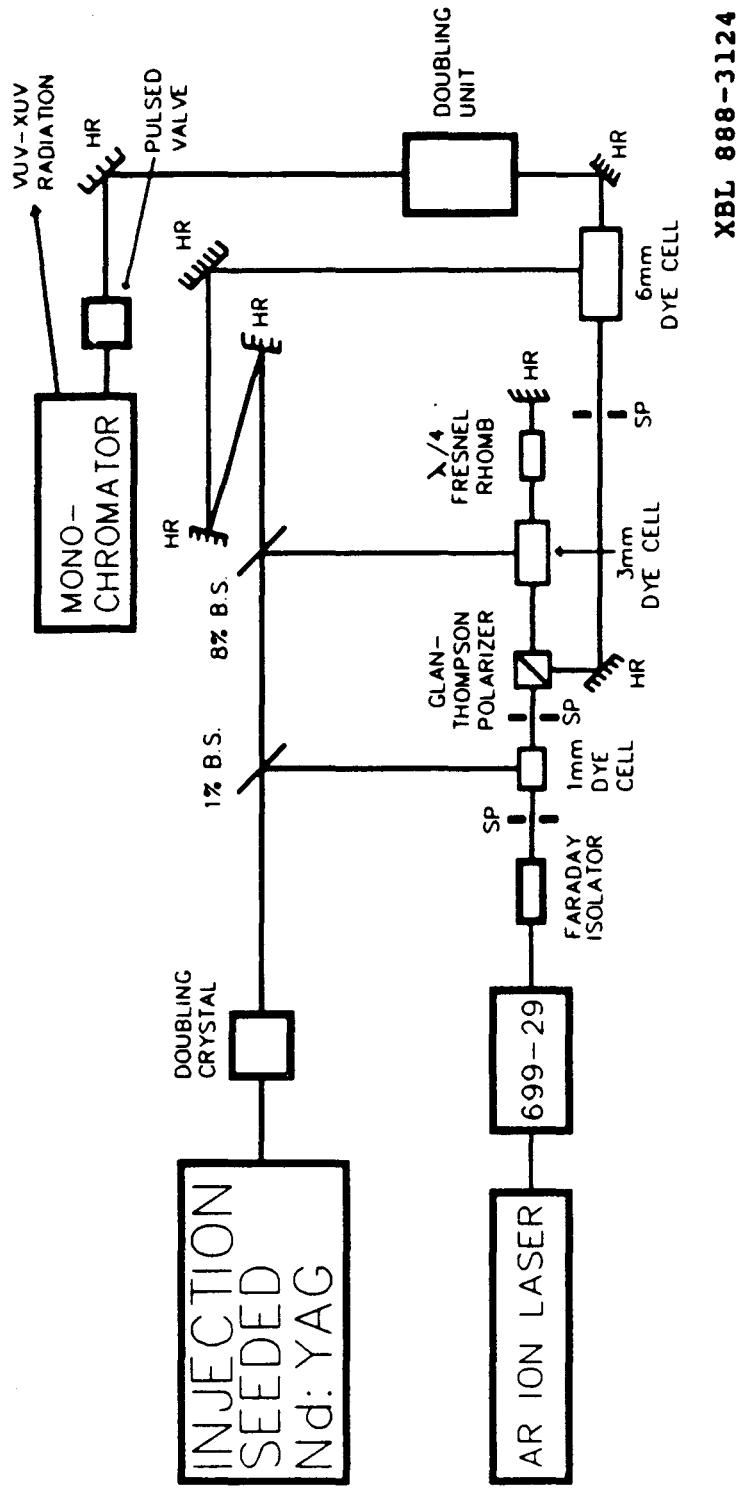

Figure 1. Schematic of one leg of the pulsed dye laser system. SP=spatial filter, HR=high reflectance mirror, BS=beam splitter.

contain any information the reader desires that is not presented below. The second section will deal with the results and performance of the laser system. This will cover the output energies that have been obtained from the infra-red to the xuv. The different frequency generation schemes that have been utilized and those that can be used in the future will also be discussed.

II. THE LASER SYSTEM

A: THE PHOTON SOURCE

The heart of the laser system is the Coherent 699-29 ring dye laser.[4] This laser is capable of emitting a continuous wave of radiation (cw) at nearly any visible wavelength. The laser is capable of operating on a single longitudinal cavity mode and is frequency stabilized by a servo-loop referenced to an external confocal étalon cavity. A two-stage wavemeter external to the cavity is used to measure the laser's wavelength to a high degree of precision. The specifications are for a bandwidth of <1MHz, a resetability of 50Mhz and an absolute frequency accuracy of <200MHz.[5]

The pump source for the 699 laser is a Coherent Innova 100 Ar^+ laser. In an Ar ion laser the lasing medium is created by a high current dc electric discharge (≈700 Amperes/cm^2) through a long tube made of a glass or ceramic

material filled with an Ar gas mixture. The tube is encased in a strong magnetic field in order to confine the plasma to the tube axis. Collisions between electrons and Ar atoms populate many Ar^+ excited states.[6] The most common lasing transitions are between the $(^3P)4p^2S_{1/2}$, $(^3P)4p^2P_{3/2,1/2}$, $(^3P)4p^2D_{5/2,3/2}$, and $(^3P)4p^4D_{5/2,3/2}$ states of odd parity and either the $(^3P)4s^2P_{1/2}$ or $(^3P)4s^2P_{3/2}$ state of even parity.[7] The upper state lifetimes average around 5ns while the lower states are rapidly depopulated to ground electronic state of the ion.[8] The only rigid selection rules are for parity flip and for $\Delta l=\pm 1$. The common lasing transitions are shown in Figure 2. The laser can be operated in two modes: all lines or single line. In the all lines mode the laser cavity consists of two broadband reflecting mirrors: a flat high reflecting rear mirror and a concave partially transmitting (≈5%) output coupler with a radius of curvature of 5-15m. In this mode the largest Ar+ lasers can deliver up to 30 Watts of power. In the single line mode a dispersive prism is inserted into the cavity in order to be able to select a single lasing transition. There is little competition between the different lines in an Ar^+ laser which makes the amount of output power at any given wavelength roughly the same in the two modes of operation. However, the total output power is reduced in the single line mode with typical energies of 10-12 watts on the strongest lines (488nm and 514nm) being obtainable. The

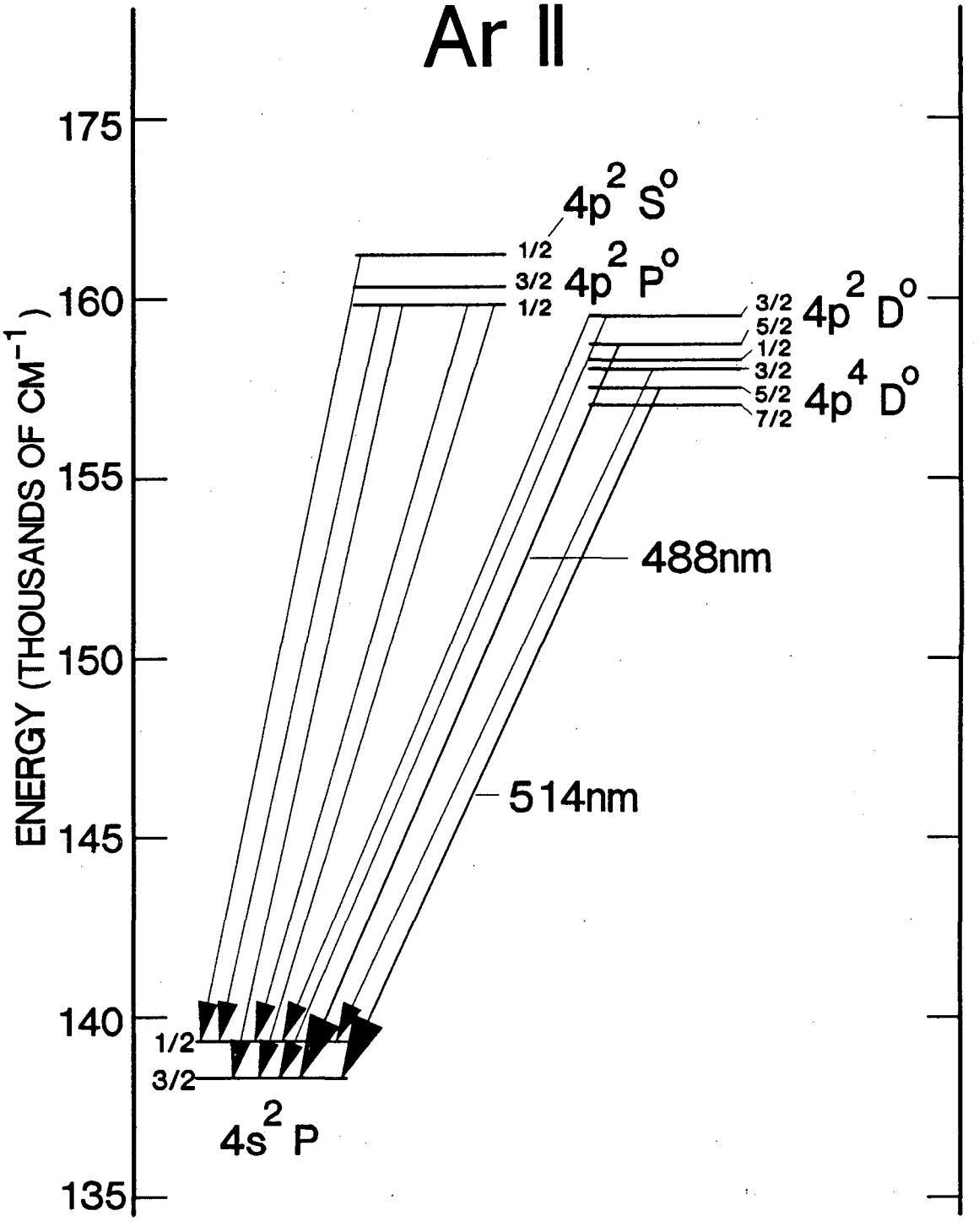

Figure 2. Some of the visible lasing transitions in the Ar^+ laser (taken from Ref.6). The two strongest lasing transitions are indicated. Energy levels are approximate.

single line cavity is shown in Figure 3. In the laser system described below the Ar+ laser is set for single line operation on the $(^3P)4p^4D_{5/2} \rightarrow (^3P)4s^2P_{3/2}$ transition at 514.532nm.

In the 699 dye laser the lasing medium is a jet of ethylene glycol (or benzyl alcohol for DCM dye) into which is dissolved various organic dyes, depending on the output wavelength desired. The laser is pumped with the output from the Ar^+ laser. Typically 6 watts of 514nm light in a TEM_{00} mode is focused onto the jet. Approximately 80% of this radiation is then absorbed by the dye molecules providing the population inversion for the lasing action. The lasing transitions occur between the lower vibrational levels of the first excited singlet level and the upper vibrational levels of the ground electronic state. Singlet-triplet transitions are important because of the detrimental effect they have on the number of molecules in the upper state. Triplet quenchers can be introduced (e.g. COT) in to the dye mixture in order to improve the performance of the laser if necessary.

The jet is the most critical aspect in the laser with regard to achieving stable operation. The width of the jet where the lasing occurs is only $\approx 100\mu m$. It is imperative that this region be extremely stable with regard to fluctuations in pointing or width. Precautions that need to be taken to insure this are cooling the dye solvent, keeping

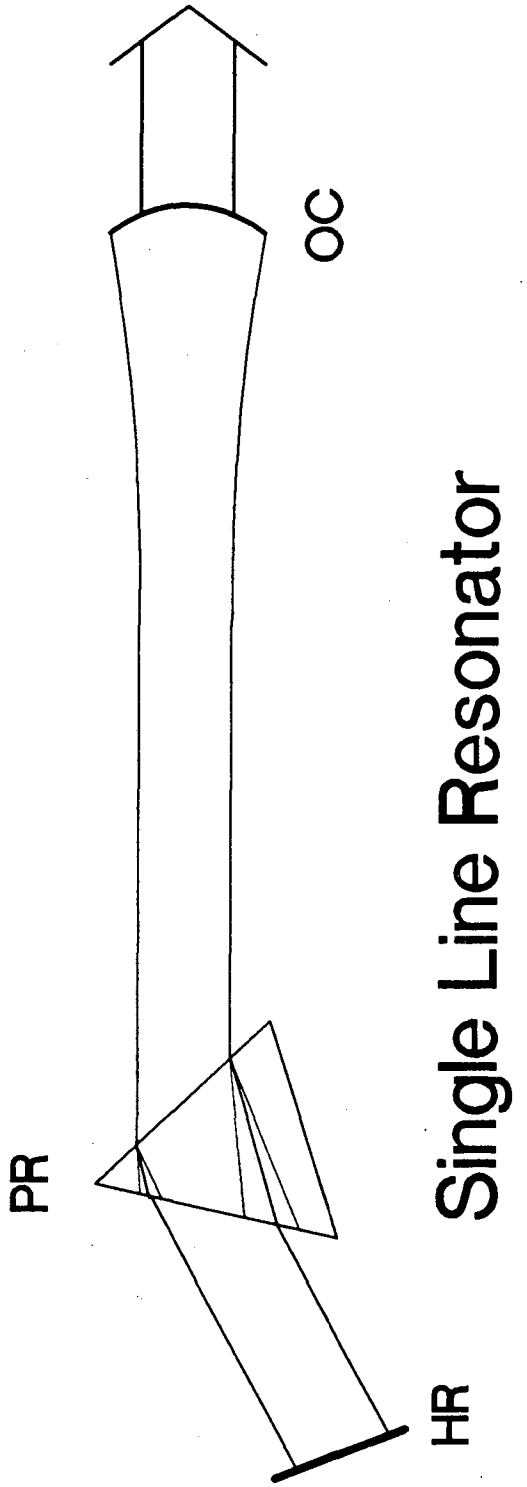

Figure 3. Laser cavity configuration for single line operation in the Ar^+ laser. HR=high reflectance mirror, PR=dispersive prism, OC=output coupler.

the nozzle clean and removing sources of vibration (such as the dye pump module) from contacting the laser.

For coherent build up of radiation in a laser cavity it is required that after one round trip through the cavity the radiation must be in phase with itself.[9,10,11] For a standing wave cavity this means that there will be nodal planes, or destructive interference, every 1/2 of a wavelength (see Figure 4a). This becomes very important in the region of the lasing medium because it causes spatial hole burning in the gain profile. If a laser tried to operate on a single longitudinal mode in a standing wave cavity the gain would be depleted only where the waves interfere constructively.[12] As one tried to pump the laser harder (to extract more energy from the laser) these regions would saturate and other cavity modes, which would utilize the gain in the areas where destructive interference of the first mode occurs, would be promoted and eventually lase. This phenomenon, known as hole-burning, makes it extremely difficult to stabilize the frequency of the laser. In a traveling wave cavity (see Figure 4b), such as is found in a ring laser, the gain is depleted uniformly allowing one to extract all the available energy in a single longitudinal cavity mode. Ring lasers are inherently easier to stabilize on a single longitudinal mode than standing wave lasers.

In a ring laser there is inherently no preferred direction for lasing. In order to force the laser to

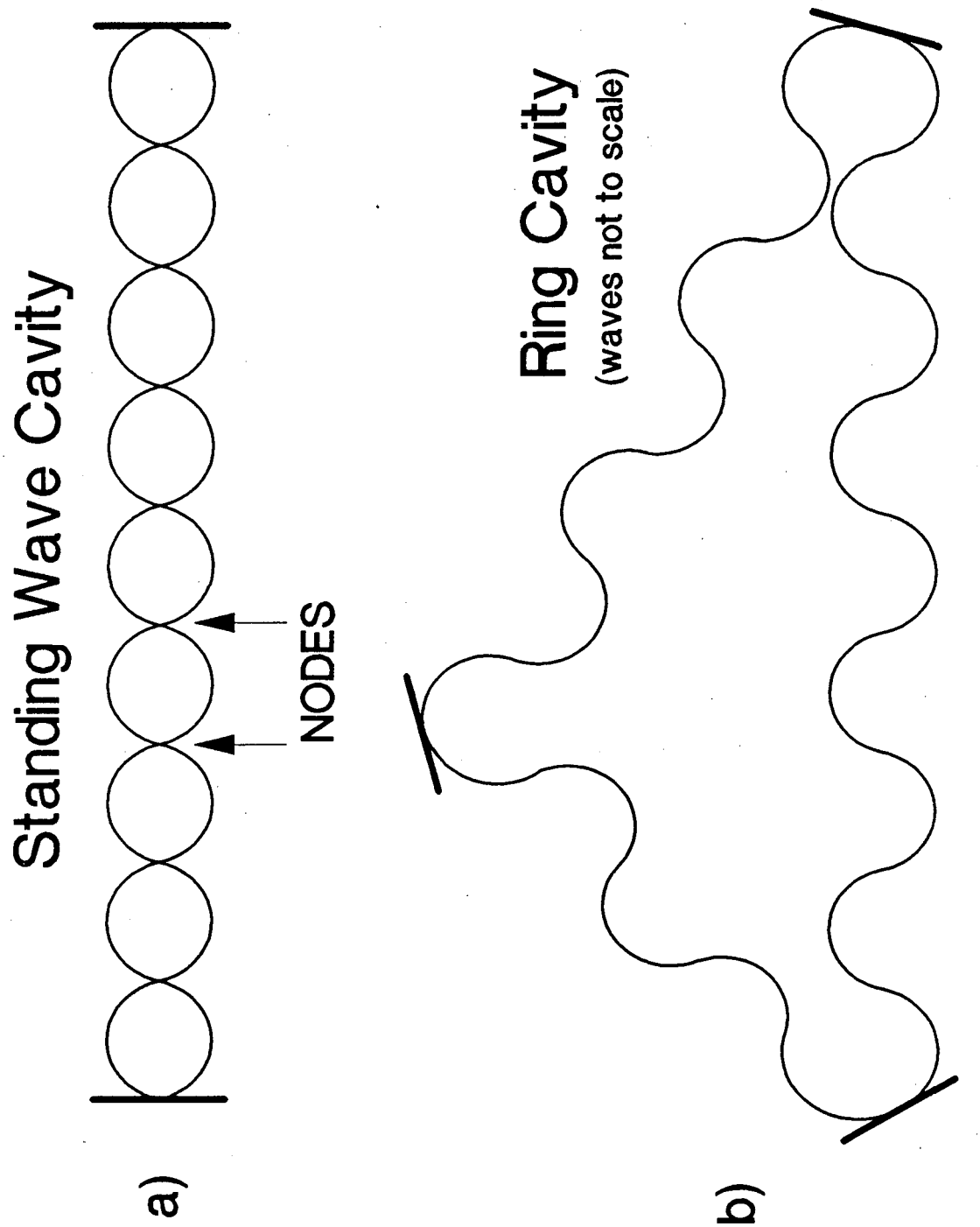

Figure 4. a) Standing wave laser cavity (with nodal points indicated). b) Traveling wave laser cavity.

operate in a single direction an optical diode assembly is inserted into the cavity. The basic idea is to incur more loss to one direction of lasing than to the other direction. A difference of only a few percent or so is usually sufficient because the exponential gain in the preferred direction will deplete the gain medium so fast that the other direction will not be able to lase. In the 699-29 polarization rotation is used to select one direction of operation (the forward direction). All the elements in the cavity are set to prefer vertically polarized light. This is accomplished by setting all non-mirror surfaces (rhombi, dye jet, etc.) at Brewster's angle for vertically polarized light thus minimizing transmission losses due to changes in the index of refraction at the surfaces of these elements. The optical diode consists of a Faraday Rotator and a piece of birefringent material. In the forward direction the two polarization rotations caused by these elements cancel each other out and the forward light remains vertically polarized. In the reverse direction, because the Faraday Rotator is a nonreciprocal polarization rotator (i.e. the direction of rotation changes for the forward and backward directions) while the birefringent material is not, the polarization rotations add up and the light ends up elliptically polarized. Thus the net effect is to discriminate against the reverse lasing direction.

In the 699 cavity there are three elements which limit the bandwidth of the laser: a birefringent filter, a thin étalon and a thick étalon. Each one of these elements successively limits the number of cavity modes lasing at any given time, by transmitting a limited frequency range, till lasing occurs on only a single longitudinal mode. In order to assure that only one longitudinal mode is resonant with the three filter elements at any given time two requirements must be fulfilled. First the spacing between the orders of one of the elements must be larger than the bandwidth of the previous element. For the birefringent filter this spacing must be larger than the bandwidth of the dye. For the two etalons the free spectral range (FSR), given by FSR=c/2L (where c=speed of light and L=width of the étalon), must be larger than the bandwidth of the previous element (the birefringent filter for the thin étalon and the thin étalon for the thick étalon). The second requirement is that the bandwidth of the most narrowband filter (in this case the thick étalon) must be less than the cavity mode spacing. A diagram showing how this selection occurs is shown in Figure 5. The bandwidth of an étalon is described by its Finesse ($\mathcal{F}$) where $\mathcal{F}$=FSR/FWHM. The finesse is dependent on the reflectivity and on the parallelness of the étalon surfaces. The higher the finesse of an étalon the narrower of a bandwidth it will pass through. A high finesse also means less transmission through the étalon which is a very

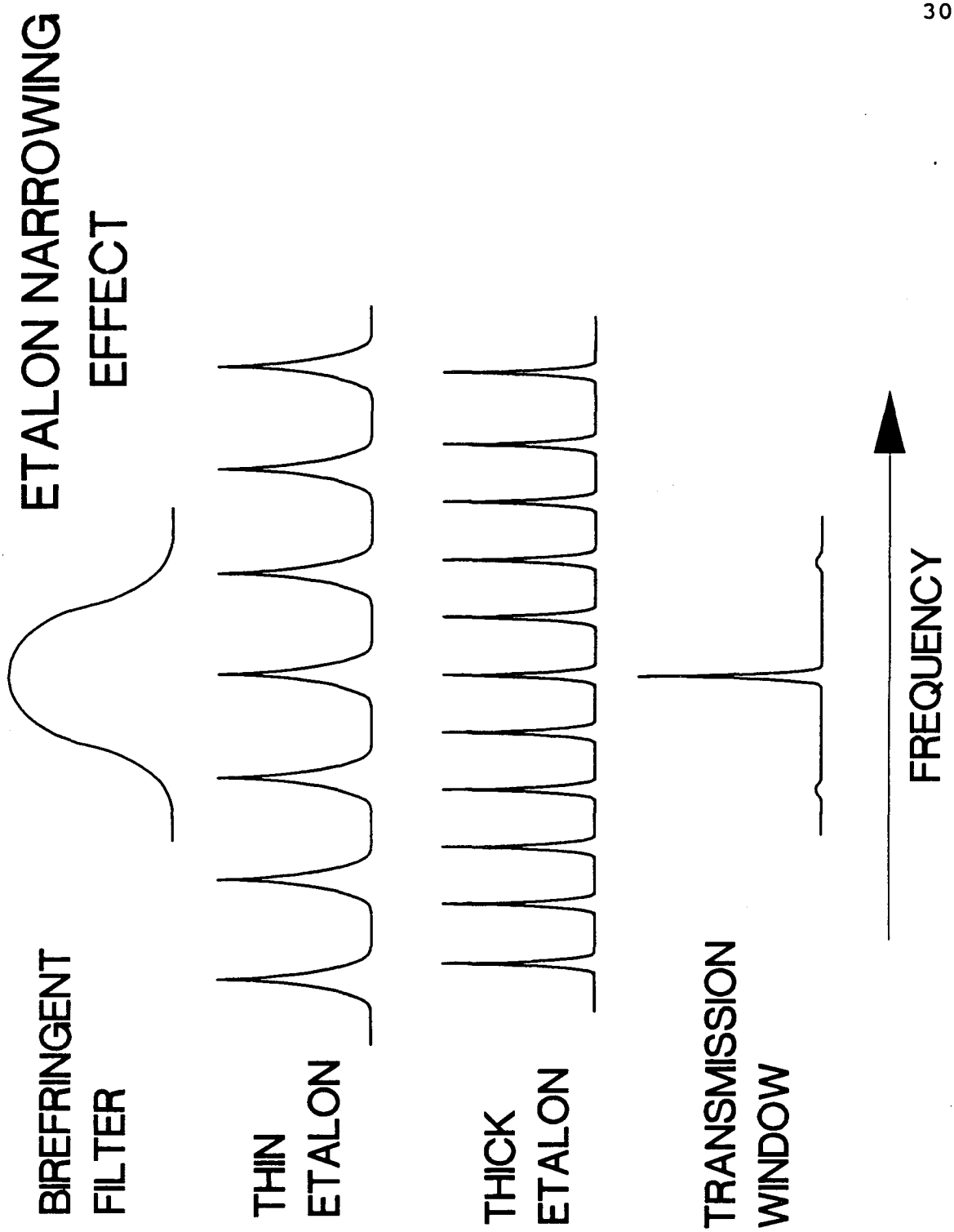

Figure 5. Depiction of process for single-longitudinal-mode selection in the 699-29 laser. Shown are the transmission versus frequency curves for the three tuning elements and the total transmission curve for those elements.

important consideration in designing a laser cavity. Thus the optimum design is one which selects a single longitudinal mode while incurring the least amount of cavity loss.[13,14] For the 699 laser the thin étalon has a FSR=10cm^{-1} and the thick étalon has a FSR=0.5cm^{-1}. Both are low finesse étalons with their surfaces coated for only ≈20% reflectivity.

For more information on the 699-29 laser the reader is referred to the laser manual[5] and to the previously referenced papers which contain information about the servo-loop used to stabilize the laser, the scanning mechanism, and the wavemeter.

B: THE SOURCE ISOLATION

There are two elements in the laser system between the 699-29 and the amplifier chain which are necessary to isolate the two lasers. The first is a Faraday Rotator optical diode[15] and the second is a pinhole spatial isolator. Each of these will be described below.

The Faraday Rotator is necessary to prevent amplified spontaneous emission (ASE) in the amplifier chain from getting back into the 699-69 and affecting the frequency stabilization. Since the amplifier chain is essentially lined up on axis with the 699 cavity, ASE from the three amplifier heads is directed into the 699 cavity and can disrupt the photodiode signals used to run the 699-29 laser.

The Faraday isolator provides four orders of magnitude of rejection of the ASE which is sufficient to let the 699 laser operate properly.

The isolator utilizes the Faraday effect where a polarization rotation is realized for light passing through certain mediums in the presence of a strong magnetic field. A measurement of how much polarization rotation occurs in a given medium is given by the Verdet constant of that medium. One of the most efficient of these mediums, and the one used in our system, is FR-5 glass (Hoya Corporation). This glass combines a very high Verdet constant with excellent transmission in the visible and near infra-red. The amount of polarization rotation is dependent on the strength of the magnetic field, the Verdet constant (which is wavelength dependent), and the interaction length. For a given wavelength the polarization rotation (θ) is calculated as follows:[16,17]

$$\theta = \int V * B_z \, dz \qquad (1)$$

where V=Verdet Constant, B_z=Position dependent magnetic field strength along the z-axis (the axis of propagation), and the integral is over the length of the glass. The amount of rotation can be controlled by either varying the strength of the magnetic field inside the glass or by varying the length of glass that the light passes through in the magnetic field. The latter method is utilized in the

laser system. Unlike the Faraday Rotator in the 699 laser which rotates the polarization only a few degrees, for optimum isolation from feedback one requires a 45° rotation of the polarization. This can be accomplished for visible light with <1cm of FR-5 glass in a 12kGauss magnetic field.

A schematic of the Faraday isolator is shown in Figure 6. The laser beam from the 699-29 passes through a Glan-Taylor (G-T) polarizing prism set to pass vertically polarized light (the polarization of the 699 laser). Next, it passes through the Faraday rotator which rotates the plane of polarization of the light by 45°. It passes through an second polarizing prism which is set to pass that polarization. Finally a half-wave Fresnel Rhomb is used to adjust the polarization of the light back to the desired direction for propagation through the amplifier chain. Light coming in the reverse direction, which in general will be unpolarized, is first filtered by the 45° G-T prism and then its 45° polarization is rotated in the opposite sense of the 699 beam, leaving it horizontally polarized. The light is then completely rejected by the first polarizing prism (set to pass vertically polarized light). The efficiency of rejection is dependent on the quality of the Glan-Taylor prisms and how close the rotation of the light by the Faraday Rotator is to 45°. The bandwidth for sufficient isolation is ≈±10nm at wavelengths around 600nm. Thus, the Faraday isolator requires optimization if the

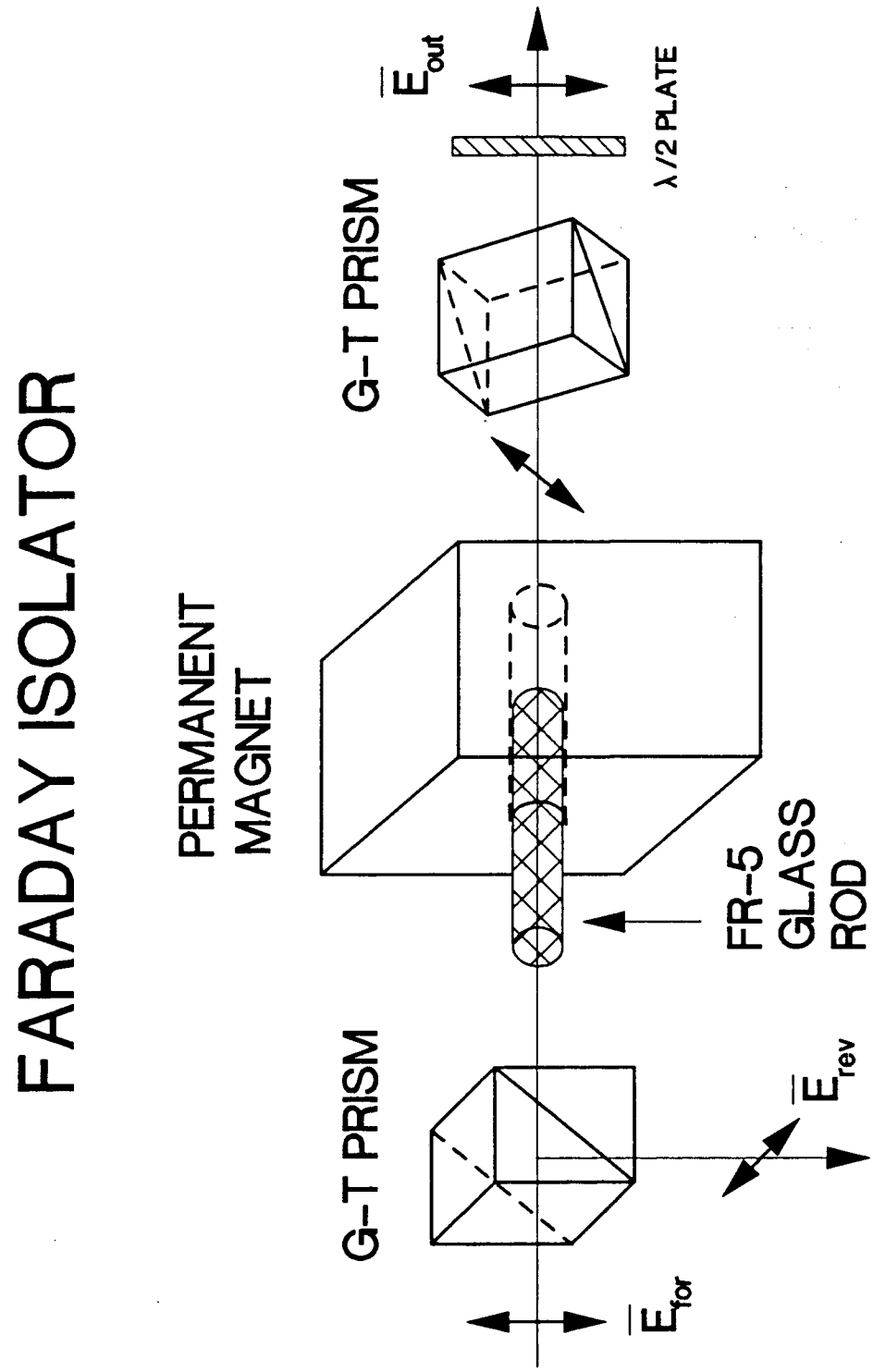

Figure 6. Schematic of the Faraday Optical Isolator. The double arrows represent the direction of polarization for the various waves traveling through the isolator, G-T=Glan-Thompson.

amplifier dye is switched but not while tuning over the gain profile of a single dye. The maximum transmission through the Faraday isolator for the 699-29 beam is ≈62%. This transmission drops off slowly as a function of wavelength to ≈50% at ±20nm from the wavelength for which the isolator has been optimized. Greater transmission could be achieved through the use of anti-reflection (AR) coated surfaces in the isolator.

The next element in the laser system is a pinhole spatial filter. This filter serves two purposes: it decouples the pointing of the 699 beam from the amplifier chain and it sets the beam diameter for the first dye amplifier cell. The isolator consists of a 50mm f.l. achromat which focuses the beam down on to a 50μm pinhole. The pinhole type used through out the system are diamond wire dies (Fort Wayne Wire Die Corp.) which have been drilled with the appropriate diameter hole. A 65mm f.l achromat is then used to recollimate the beam expanding from the pinhole. A schematic of the set-up is shown in Figure 7.

Pointing decoupling can be achieved if the spot size of the laser beam at the pinhole is significantly greater than the diameter of the pinhole. Under these conditions the pinhole acts as a point source of light and the direction of the laser is controlled by the recollimating lens. This necessarily reduces the amount of light transmitted through

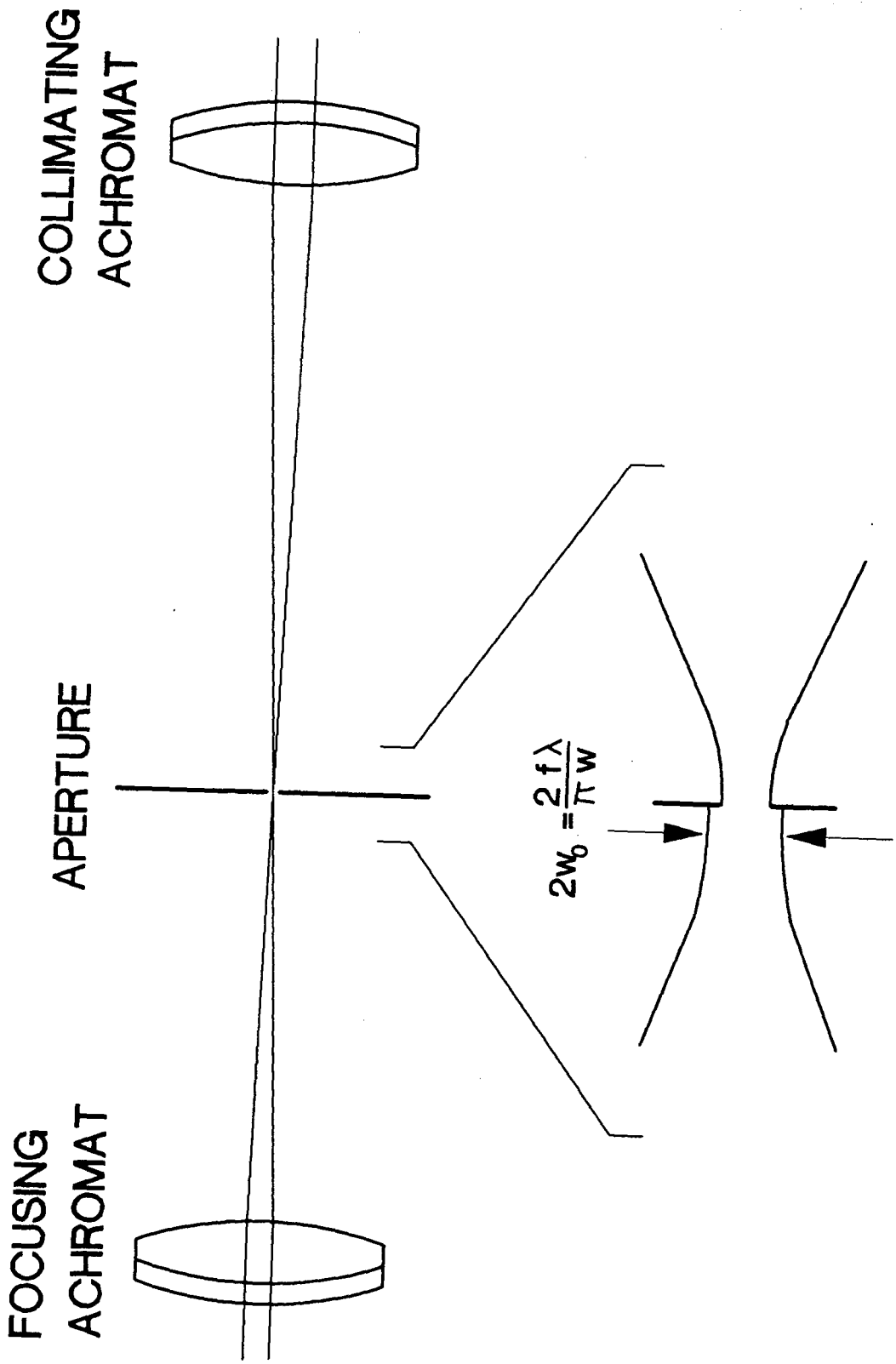

Figure 7. Schematic of the Pinhole spatial isolator (not to scale).

the pinhole. The $1/e^2$ focal spot radius (w_0) for a Gaussian, diffraction limited beam of radius, w, focused by a lens of focal length, f, is given as follows:

$$w_0 = \frac{f\lambda}{\pi w} \tag{2}$$

where λ=wavelength of the light being focused. For a beam radius of 0.5mm, a focal length of 10cm, and a wavelength of 600nm this gives a focal spot radius of 38μm, or a diameter of 76μm, which is ≈50% greater than the 50μm pinhole. In practice, due to the non-Gaussian nature of the laser beam, a 5cm focusing achromat is found to give a better balance than a 10cm lens between spatial isolation by and beam transmission through the filter. The transmission through the spatial isolator measured is ≈60% with the 5cm focusing achromat.

The intensity distribution of the beam propagating from the aperture can be described by an Airy pattern. The functional form of this distribution is given as follows:[18]

$$I_v = I_0 * \left[\frac{2 * J_1(v)}{v}\right]^2 \tag{3}$$

where v is given by:

$$v = \frac{\pi D}{\lambda} * \frac{r}{z} \tag{4}$$

and J_1=1st order Bessel function, I_0=intensity on the beam axis, D=diameter of the aperture, z=distance from aperture (along the beam axis), and r=radial distance from the beam axis.

The first zero of the function I_v occurs at $v = 1.22*\pi$. The choice of the focal length of the second lens in the spatial isolator is dictated by the desired beam diameter at the first dye amplifier cell. Using equation 4, one can calculate that for a diffraction limited beam expanding from a 50μm diameter aperture the radius of the first minimum is 1mm at a distance of 68mm from the aperture. The use of a 65mm f.l. achromat as the collimation lens sets the FWHM of the beam approximately equal to the diameter of the first dye cell (diameter=1mm). This fills the first dye cell completely allowing for efficient energy extraction and good control of the ASE and laser beam quality.

C: DYE AMPLIFIER PUMP SOURCE

The power source for the dye amplifier chain in the laser system is an injection seeded Nd:YAG laser (Quantel model 592). A Nd:YAG laser was chosen because of the high powers obtainable at 532nm, a wavelength readily absorbed by many efficient dyes, and because the pulse duration afforded a good compromise between temporal duration (important when considering peak powers which affect non-linear mixing efficiencies) and frequency resolution. The laser is

capable of emitting >500mJ of doubled fundamental radiation (532nm) although it is typically operated at an output of 450mJ. The pulse has a temporal width of 10ns and is specified for a bandwidth of ≈90MHz at 1064nm. The spatial and temporal profiles are both near Gaussian.

As mentioned above, the Nd:YAG oscillator is seeded with narrowband radiation in order to force the laser to operate on a single longitudinal mode. The seed laser is a diode pumped monolithic Nd:YAG crystal cut in a non-planar ring oscillator (NPRO) configuration (LightWave Electronics model S-100). This design produces a single-mode cw beam of 1064nm radiation with an output power of ≈5mW. A schematic of the seeder laser is shown in Figure 8. The Nd:YAG crystal is forced to lase in a single direction by a dual rotation of the beams polarization during a transit of the ring.[19] One source of rotation comes from an out-of-plane motion realized by the photon beam during a trip through the cavity. The other source is a Faraday rotation induced by an electro-magnet which encases the NPRO crystal. As in the case of the optical diode in the 699 laser described previously the polarization rotations in the forward direction cancel out while those in the reverse direction add up and induce losses at the reflective surfaces. The wavelength of the seed laser is controlled by varying the temperature of the crystal. The seed laser is isolated from feedback from the main oscillator by a Faraday isolator

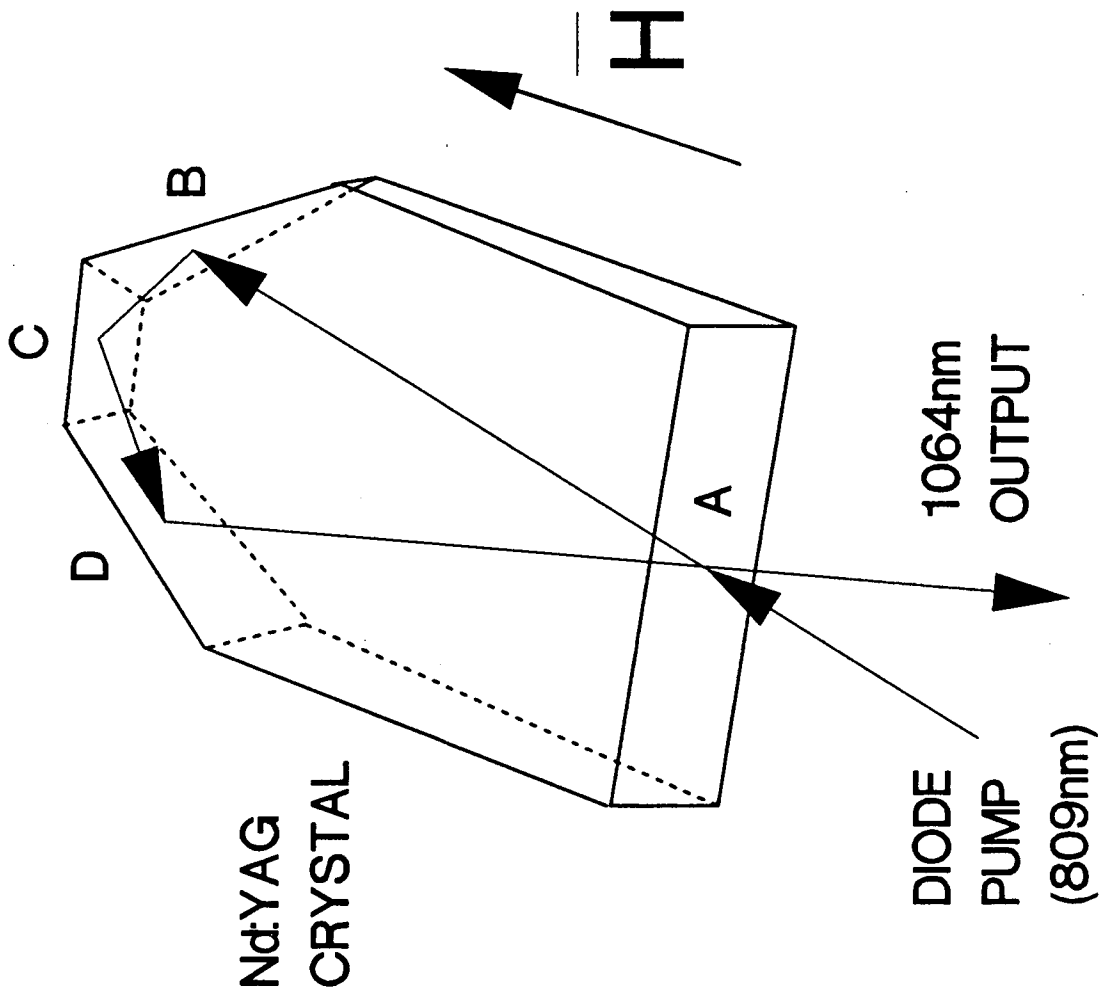

Figure 8. Schematic of the monolithic NPRO Nd:YAG laser. Faraday rotation occurs along paths AB and DA, out-of-plane motion occurs along BCD.

utilizing a temperature controlled electro-magnet.

The seed laser beam is introduced into the oscillator by polarization coupling. The beam is reflected off a beamsplitter, set at Brewster's angle with respect to the cavity's polarization, along the axis of the oscillator cavity. The seed laser polarization is orthogonal to the cavity's polarization. It is necessary to match the wavelength of the seed laser with that of a single longitudinal mode of the oscillator. Furthermore, for stable seeded operation one requires that this frequency be at the peak of the gain of the oscillator.[20] The frequency matching requirements are shown pictorially in Figure 9.

Frequency matching is obtained as follows. First, the wavelength of the seeder laser is set to the maximum of the Nd:YAG oscillator by temperature tuning the monolithic crystal. This is determined by observing the doubled frequency output of the laser in seeded and non-seeded modes through an appropriate étalon (FSR≈1GHz). The cavity length is then adjusted via the rear mirror which is on a piezo-electric (PZT) crystal driven mount. The optimum cavity length is obtained by monitoring the cavity build up time. When the seed laser frequency exactly matches that of a cavity mode the time that is required for lasing to occur after the Q-switch is activated will be a minimum. A photodiode monitors the timing of the laser output at 1064nm and an internal circuit in the seeder laser housing compares

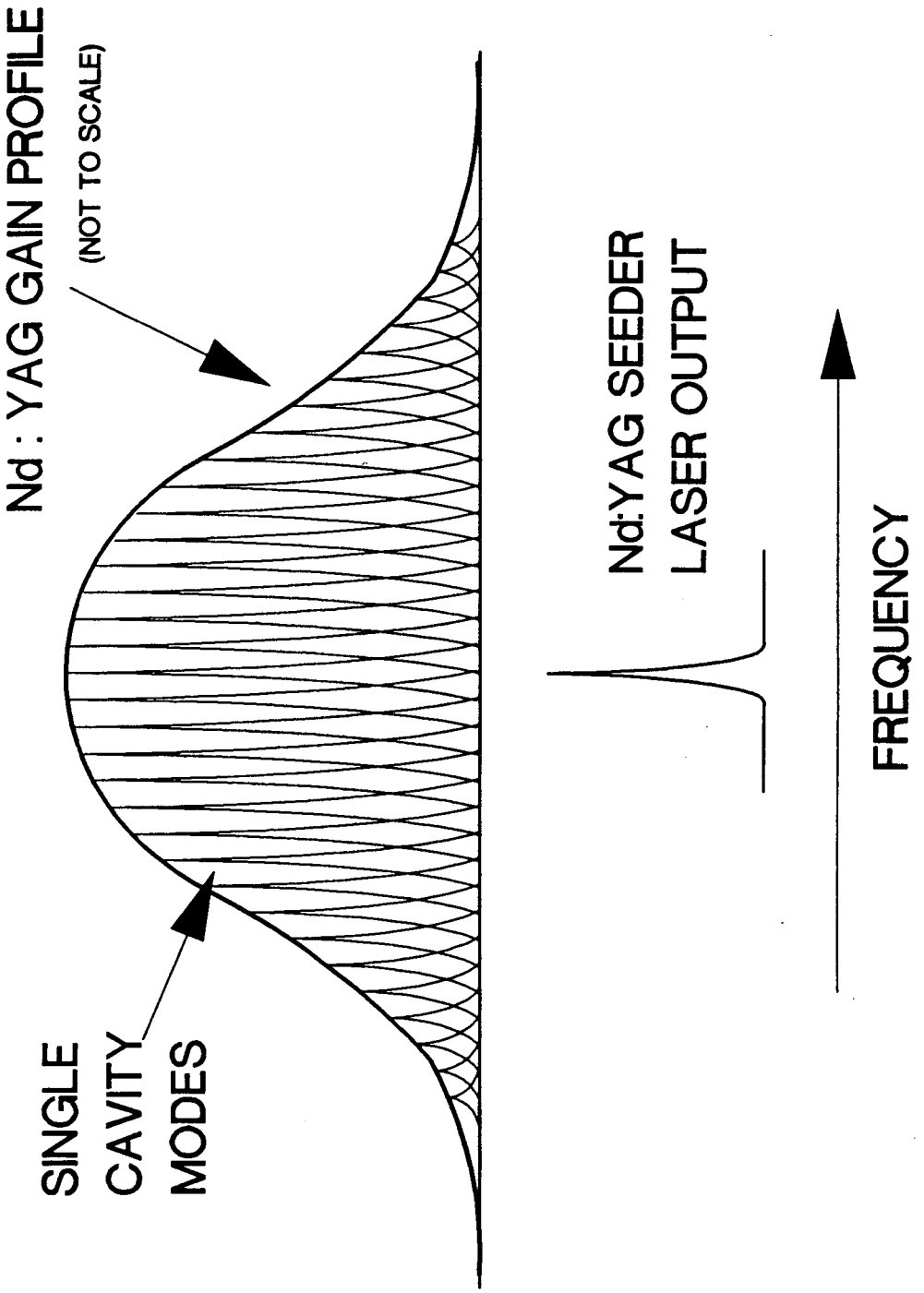

Figure 9. Depiction of single-longitudinal-mode selection in the Nd:Yag laser. Shown are the frequency outputs of a non-seeded Nd:YAG oscillator and the seeder laser and the relative position (in frequency space) necessary for correct seeded operation.

that to the Q-Switch synchronized output and adjust the voltage applied to the PZT crystal on the rear mirror till the timing difference is a minimum. A high frequency oscillation is applied to the pzt crystal in order to provide information on which direction to change the voltage.

Injection seeding of the Nd:YAG oscillator has two important effects on the performance of the laser system: it reduces the bandwidth of the dye laser and diminishes the magnitude of intensity fluctuations for the mixed radiation. The actual spread in frequencies of the Nd:YAG laser does not affect the bandwidth of the dye laser directly because it is decoupled by the fast non-radiative decay in the excited electronic state of the laser dye. However, the temporal profile of the Nd:YAG pulse does affect the dye laser's bandwidth. An important limiting factor on the bandwidth of the system is the temporal profile of the amplified dye laser pulse. This, in turn, is determined mainly by the temporal profile of the pump laser pulse. This coupling is a result of fluctuations in the gain in the dye amplifiers which mimic the intensity fluctuations of the pump pulse due to the relatively short lifetime of the dye's upper excited state and the continuous extraction of energy from the amplifiers by the dye laser pulse. Since the Nd:YAG lases on a single longitudinal cavity mode, there are no mode-beating induced modulations in the temporal profile

of the pump beam and the dye laser's temporal profile is made as smooth as possible resulting in the narrowest bandwidth.

Use of the injection seeded Nd:YAG laser also produces a more stable uv and xuv power. In a multi-mode pulse instantaneous peak powers during the pulse can be much higher than in a smooth single-mode pulse for a given average pulse. Since non-linear processes are proportional to a higher order of the peak intensities present in the pump pulse there is inherently more fluctuation in the mixing efficiency when a multi-mode pump pulse is used. This is because the mode beating pattern, and hence the peak intensities, changes from pulse to pulse. For a train of single-mode pulses (where the pulse to pulse energy fluctuations are the same as for the multi-mode train) the peak intensity is significantly more steady. Hence not only is the doubled Nd:YAG power more stable under single-mode operation, the fluctuation in the uv and vuv output from the dye laser systems is also reduced.

D. THE DYE AMPLIFIER SYSTEM

The dye cells used are similar to the prism cells developed by D.S. Bethune for an excimer pumped dye laser.[21] These are side-pumped cells with the pump beam being internally reflected into the dye off the sides of the prism. A cut-away view of a prism dye cell showing the

pumping geometry is given in Figure 10. Similar systems have recently been used to amplify ultra-short pulses with high gain.[22,23] The prism type dye cell has certain advantages associated with it. The dye is pumped from all sides so the gain can be made uniform to preserve the spatial quality of the seeding beam. There is no window damage by the pump laser because of the large pumping area. Finally, the amplified beam's spatial profile is decoupled from that of the pump beam. This enables the system to be used with pump sources that have very different beam shapes.

Three dye amplifiers are used in our design. The first cell has a bore size of 1mmϕ x 20mm long. The second cell, which is double-passed, has a 3mmϕ x 30mm long bore. The final amplifier is 6mmϕ x 60mm long. We find that by adjusting the dye concentration such that one dye absorption depth at the pump wavelength equals approximately the bore diameter the best output beam profile and power combination are obtained. In this design the amplifier gain is changed by varying the pump beam intensity at each stage.

As mentioned previously, the population inversion that is induced in an organic dye is generally between the lowest ro-vibrational states of the first excited singlet electronic state (S_1) and the upper ro-vibrational states of the ground electronic state (S_0), also a singlet state. Absorption of the pump radiation, which promotes the molecules into high ro-vibrational states of S_1, is followed

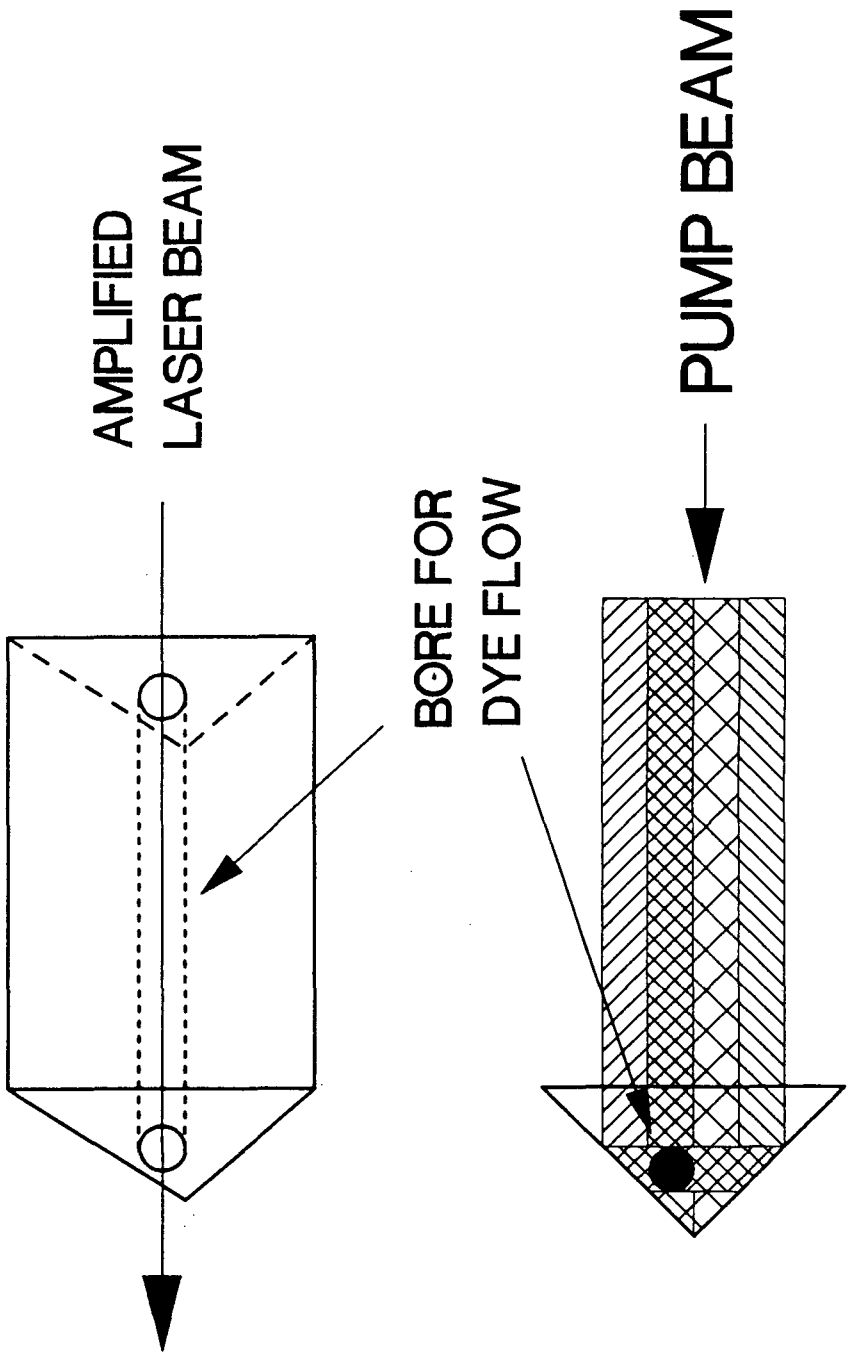

Figure 10. Two views of the prism dye cell utilized in the dye amplifier systems.

by fast non-radiative decay into the lower energy region of the S_1 manifold creating a large upper state population. After radiative decay into the S_0 manifold the lower lasing levels are rapidly depopulated by relaxation of the highly ro-vibrationally excited molecules, again by non-radiative processes, into the lower energy region of the S_0 manifold. In any analysis one also needs to include the first excited triplet state (T_1) which can reduce the upper state population density. A schematic of these energy levels is shown in Figure 11.

The total gain expected in any given cell is a complicated function of the total number of pump photons absorbed, the stimulated emission cross section of the dye (which is wavelength dependent), the excited state lifetime of the dye, position dependent saturation of the gain medium and also the losses present due to absorption, ASE depletion, singlet-triplet transitions, reflections etc. The gain can be estimated with the following differential equation:[24]

$$\begin{aligned}\frac{d[I(x,t,\lambda)]}{dx} &= N_1(x,t)\,\sigma_e(\lambda)\,I(x,t,\lambda) \\ &\quad + \tau^{-1}N_1(x,t)\,E(\lambda)\,g(x) \\ &\quad - \sigma_{01}(\lambda)\,N_0(x,t)\,I(x,t,\lambda) \\ &\quad - \sigma_T(\lambda)\,N_T(x,t)\,I(x,t,\lambda)\end{aligned} \qquad (5)$$

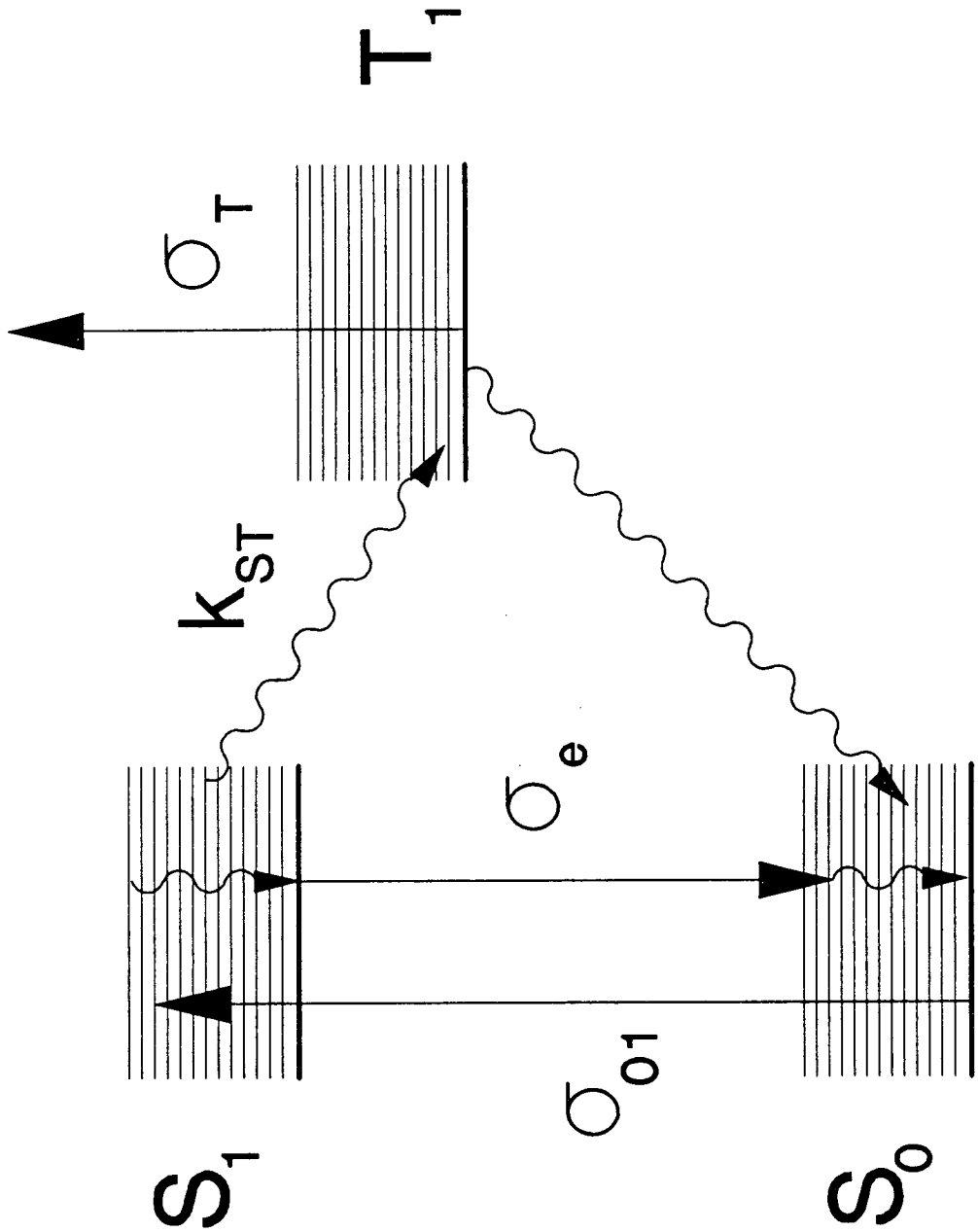

Figure 11. Three main electronic levels involved in a typical organic dye laser and the important transitions. Lasing occurs between S_1 and S_0. S=singlet level, T=triplet level, σ_{01}=absorption cross-section, σ_e=emission cross-section, σ_T=triplet state absorption cross-section.

where $I(x,t,\lambda)$=photon flux per unit wavelength which is a function of the position in the dye cell (x), the time during the pulse (t) and the wavelength of the photon (λ), $N_i(x,t)$ (i=0,1,T)= population density in S_0, S_1, and T_1 respectively, $\sigma_i(\lambda)$ (i=e, 01, T) = cross section for stimulated emission, singlet state absorption and triplet state absorption respectively, τ=natural lifetime of S_1 state, $E(\lambda)$= fluorescence spectrum normalized to the quantum efficiency, and g(x)=geometrical factor determining the amount of spontaneous emission directed through the dye cell. The four terms in (4) describe stimulated emission, spontaneous emission, absorption from the ground state and triplet state absorption respectively.

Telescopes consisting of a lens-pinhole-lens combination and magnifying powers of x1, x3 and x2 are used to shape the c.w. dye laser beam profile to fill the bore of the first, second and third amplifiers respectively. In optimizing the performance it is necessary to fill the dye cells as completely as possible. There are a number of benefits from this. The larger the dye beam the larger the extraction volume will be. Since the total output is dependent on the number of excited dye molecules accessed (N_1) and that number is proportional to the extraction volume a larger dye beam extracts energy more efficiently. A second effect is to reduce saturation in any given dye

cell. The saturated gain is given by:

$$G_{sat} = \frac{G_0}{(1 + I_0/I_{sat})} \qquad (6)$$

Increasing the amplified beam decreases the local I_0 thereby reducing saturation effects. A third, and important, effect is to help deplete the ASE. Fast extraction of energy from the dye cell by the amplified beam reduces the amount of gain available for ASE. If there are areas in a given cell in which no amplified beam is present there is nothing to prevent the ASE from "taking off" and robbing gain from the amplifier beam in the next dye cell. Since the ASE is strongest along the circumference of the dye cells it is necessary that the amplified beam fill all the way to the edges of the dye cells in order to control the amount of ASE present in the final beam.

The pinholes serve as spatial filters to maintain a diffraction-limited profile for the dye beam as well as to control the growth of ASE which could deplete the gain in the amplifiers.[3] The first pinhole has been described previously. The second pinhole and third pinhole are chosen to transmit 99% of the fundamental mode energy and to block higher order modes. This serves to eliminate off-axis growth of ASE.

Double passing of the second dye cell is accomplished through a polarization rotation technique. The horizontally polarized beam is filtered through a Glan-Taylor prism

before going into the dye cell. After passing through the cell the polarization is rotated 45° by a Fresnel Rhomb. The beam is then reflected back on itself by a broadband high reflectance mirror and makes a second pass through the Fresnel Rhomb which changes the plane of polarization to the vertical direction. This vertically polarized beam then makes a second pass through the dye cell and is completely reflected by the Glan-Taylor prism at an angle of ≈60°.

In setting up the double pass arrangement two things proved quite critical. One was to avoid reflecting fluorescence off of the Fresnel Rhomb into the dye cell. If this was not done the amplification of the laser beam in the second dye cell suffered greatly due to gain competition with the reflected light. Second, it was necessary to keep the beam path as short as possible in order to keep the pulse length as long as possible. The fluorescence lifetime of the dye is typically on the order of two to five nanoseconds. For a beam path of two feet (i.e. having the reflecting mirror 1 foot away from the dye cell) there would be a delay of two nanoseconds before the amplified pulse returned to the second dye cell after making its first pass. A geometry such as this would tend to cut off the end of the pulse which in turn would increase the bandwidth of the pulse. Moving the reflecting mirror from 1' to 5" (the minimum length practical) resulted in decreasing the bandwidth from 110MHz to 91MHz for operation with R6G dye.

The methods used for the bandwidth measurements and more complete results will be presented below.

E. UV GENERATION

Second harmonic generation is accomplished with either an INRAD 5-12 autotracking unit or a Quanta-Ray WEX1 utilizing KDP crystals. Extension to shorter wavelengths is achieved by mixing in β-Barium Borate (BBO). There are two basic requirements for non-linear optical mixing of two photons. The first is conservation of energy. The energy, or frequency, of the generated photon must be equal to either the sum or the difference of the frequencies of the two input photons. The second requirement is one of conservation of momentum which is generally referred to as the "phase matching condition". These relations are given as follows:[25]

$$\omega_3 = \omega_1 \pm \omega_2 \tag{7}$$

$$\underset{\sim}{k}(\omega_3) = \underset{\sim}{k}(\omega_1) \pm \underset{\sim}{k}(\omega_2) \tag{8}$$

The magnitude of the wave-vector of a photon, k, is given by:

$$k = \frac{n\omega}{c} \tag{9}$$

Since k is dependent on the index of refraction, n, of the medium the wave-vector matching criterium is satisfied, for collinear propagating beams, if the index of refractions for the different photons are equivalent (i.e. $n_1=n_2=n_3$).

In a normally dispersive and isotropic medium the variation of n with the frequency of light is such that the above criteria cannot be satisfied. However, in a birefringent medium the index of refraction for ordinary (o) and extraordinary (e) rays are different. Furthermore the value of n_e is a function of the angle between the direction of propagation through medium and the optical axis of the medium. For certain birefringent crystals the index of refraction matching criterium for mixing processes can be satisfied over a wide frequency range by varying the angle of the crystal with respect to the incoming radiation provided that one of the photons is polarized orthogonal to the other two. This provides two types of mixing:[26]

$$\textit{Type I}: \quad \underset{\sim}{k}_3^{(e)} - \underset{\sim}{k}_1^{(o)} \pm \underset{\sim}{k}_2^{(o)} \tag{10}$$

$$\textit{Type II}: \quad \underset{\sim}{k}_3^{(e)} - \underset{\sim}{k}_1^{(e)} \pm \underset{\sim}{k}_2^{(o)} \tag{11}$$

The wavelength region covered by any given crystal depends on the angle that the face of the crystal has been cut with respect to the optical axis of the crystal and the acceptance angle of the crystal. The absorption by the crystal at any of the wavelengths used in the mixing process is also important. A standard INRAD KDP crystal, which has a 10mm x 20mm face and is 30mm long can double wavelengths over an ≈60nm range in the visible. For generation of uv wavelengths below 260nm KDP is not very useful because of its strong absorbance. BBO has a transmission window down to ≈190nm and has successfully been used to frequency double to ≈205nm and to frequency mix to ≈191nm.

F. SHORT WAVELENGTH EXTENSION

VUV generation is done via four-wave mixing in a pulsed jet of atoms or molecules. This process has been described in detail previously.[27,28,29,30,31] A schematic of the four-wave mixing chamber is shown in Figure 12. Here we list a few of its features. First, there are no exit windows for the tripled light to pass through so there is no short wavelength cut-off absorption by the window material. Second, the length of the tripling region is not necessarily greater than the confocal parameter of the beam so the tripling medium does not have to be negatively dispersive.[32] Finally, for the shorter wavelengths the problem with self-absorption is reduced.

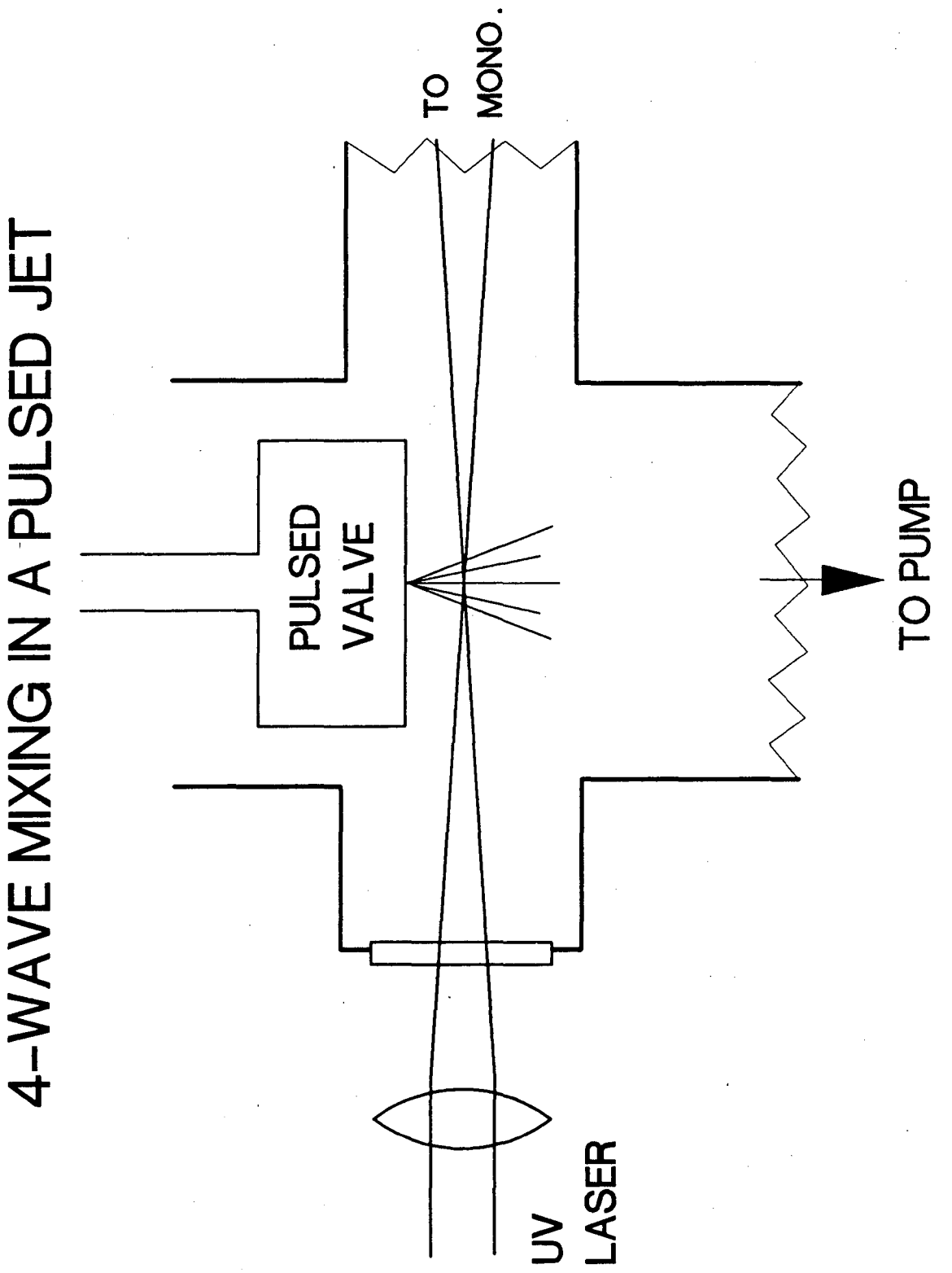

Figure 12. Schematic of set-up used for four-wave mixing in a pulsed jet. Mono.=vacuum monochromator.

In the four-wave mixing process three input photons, or waves, are mixed together to form a single output photon, or wave, hence the term four-wave. There are many variations of this process. One can mix three of the same photons, in which case the process is called straight tripling, or one can take the sum or differences of photons of different wavelengths, in which case the process is called sum or difference frequency mixing. In addition to extensive review articles on vuv and xuv generation[33,34] there are numerous references dealing with straight tripling and sum frequency mixing in metal vapor cells[35,36] and rare gas cells,[37,38,39,40] resonance mixing in rare gases,[41,42] and mixing in the molecular gases CO[43,44,45,46] and NO.[47,48]

The overall efficiency of the tripling process can be described by the polarizability:

$$P(\omega_3) - P(\omega)^3 * N^2 * \chi_3(\omega) * |\phi|^2 \qquad (12)$$

where P is the polarizability of the mixing medium at a given frequency, N is the number density of the medium, $\chi_3(\omega)$ is the non-linear susceptibility, Φ is a function of the wave vector mismatch, and $\omega_3=3\omega$. The figure of merit for how efficient a medium will be for mixing is the non-linear susceptibility, $\chi_3(\omega)$. This factor depends on the various energy levels present and can be calculated according to:

$$\chi_3(\omega) \propto \sum_{i,j,f} \frac{\langle E_f|V_{fj}|E_j\rangle * \langle E_i|V_{i0}|E_0\rangle * \langle E_j|V_{ij}|E_i\rangle * \langle E_0|V_{f0}|E_f\rangle}{(E_f-3\omega) * (E_j-2\omega-\Gamma_j) * (E_{0i}-\omega)} \quad (13)$$

Equations (12) and (13) can be extended to describe mixing processes.

One change we have made compared to our previous vuv generation experiments is the use of a large travel PZT driven pulsed valve.[49] This new home-made valve (operated with a 1mm diameter nozzle) allows for a larger throughput than the commercial valve that was used previously (LaserTechniques). This gives nearly a factor of ten increase in number density in the tripling medium which in turn results in a greatly improved tripling efficiency. Together with a higher uv power, up to two orders of magnitude improvement in xuv signal has been seen with the new valve.

G. PHOTON SEPARATION TECHNIQUE

The last component to be discussed here is the 1m normal incidence monochromator (McPherson model 225) used to separate the photons of different wavelengths present in the laser beam. While the monochromator reduces the vuv-xuv beam intensity by a large factor it introduces a tremendous amount of experimental versatility making it an invaluable component in the laser system. The monochromator offers two major conveniences. The first, as mentioned above, is that it separates out the fundamental light beams, permitting the

use of vuv and xuv photons without interference from the powerful uv and/or visible beams when desired. The second is that the curved grating recollimates the vuv-xuv beam allowing an optimal spatial overlap of the photon beam with our molecular beam in the ionization chamber. Optical damage to the grating is minimized by expanding the uv beam to fill the size of the grating.

The position of the grating inside the monochromator can be varied in order to change the spot size of the laser beam in the interaction region. This can be accomplished in two different manners. The grating mount can be adjusted to position the grating closer to the entrance and exit slits. The focal spot of the laser beam is then moved closer to the interaction region by twice the distance that the grating is moved. With the grating in its normal setting the focal spot of the laser beam is ≈12cm in front of the axis of the ion optics. The mount is designed with enough travel so that the laser can be focused underneath the ion optics. A second degree of freedom is provided by moving the four-wave mixing nozzle, along with the focusing lens, along the axis of the laser beam. This is a more sensitive adjustment and allows only 1-2cm of travel.

In addition to the 1m grating, a 1.18m grating has also been used in the monochromator. This is mounted in a separate holder connected to the rear flange of the monochromator. The position is set to focus the beam

underneath the ion optics although a small amount of travel is provided with the mount for adjusting the location of the focal spot. In this set-up it is not possible to scan the grating so, in essence, the grating acts as a focusing mirror. An advantage with the longer focal length grating is that the uv spot size at the grating is larger reducing the amount of damage to the coating.

H. NORMALIZATION TECHNIQUES

The inherent fluctuations in the vuv power can often be the limiting factor in the signal to noise ratio obtainable for any given experiment. As a result of this it is important to be able to monitor the intensity of the vuv, shot by shot, so that one can normalize the ion signal to this intensity. This is not a trivial problem for many experiments. The presence of the residual uv light from the four-wave mixing process often interferes with attempts to measure the vuv power directly due to its much greater intensity (uv $>10^5$ x vuv). Furthermore, the large fluctuations in the vuv signal require that the sensor maintain a linear response over a wide dynamic range.

The most trivial method for vuv normalization is to use the EMT to monitor the vuv power. The EMT does not have a window so it is useful for any wavelength within the response range of the CuBe cathode ($\approx$5 to 15 eV). It also has a wide dynamic range. While this provides a good

normalization signal it is only useful for experiments where the monochromator is set to first order. For experiments which require the monochromator to be set to zeroth order the uv light swamps the EMT making it useless as a source for a normalization signal.

A second method that has been used successfully is the introduction of secondary gas into the molecular beam which is directly ionized by the vuv radiation. This provides an ion signal which is proportional not only to the vuv power but also to the gas density in the molecular beam. There are certain requirements for the molecule to be used for normalization. It must have a low enough ionization threshold so that the wavelengths where it will be used will lie in the ionization continuum of the molecule. There must be no structure due to autoionizing resonances in the frequency range of interest. Finally, it should not interfere with the ion signal being measured and its signal strength must be on the same order of magnitude as that of the ion signal. Perhaps the gas most useful for this purpose is acetylene. It is still limited to wavelengths shorter than ≈100nm. NO is another gas that should work successfully (although the author has never used it for normalization purposes) but it has the drawback of being very noxious. One gas that appeared to be promising was allene ($H_2C=C=CH_2$) however it turns out to have a fair amount of structure in its ionization spectrum making it not

very useful for experiments which involved scanning the laser.

There are no readily available gases which work well for normalization at wavelengths longer than ≈110nm. In order to normalize at these wavelengths a solar blind photomultiplier tube (SBPMT) was set up inside the monochromator to look at the 1st order vuv light diffracted off of the grating. This is shown in Figure 13. The SBPMT used had $>10^4$ discrimination against uv light. Even so, there was a fair amount of background from scattered uv light in the chamber. This signal could be reduced to tolerable levels by the use of baffling around the SBPMT. The SBPMT has a LiF window covering the cathode so it is only useful for wavelengths longer than 106nm. In addition the uv response starts to increase rapidly for wavelengths shorter than 285nm. This method proved useful for normalizing to vuv generated by 2+2+1 mixing in Xe using the 5p-7s and 5p-5d resonances in the wavelength regions 113nm to 117nm and 117nm to 119nm respectively.

Perhaps the most versatile method for vuv normalization involves using a Platinum photodiode (Pt P.D.). The use of this type of system has been noted by White et al.[50] A significantly different design was developed in this laboratory primarily by A. Stolow. A schematic of the Pt P.D. used is shown in Figure 14. The vuv light impinges upon a piece of Pt ejecting electrons by the photoelectric

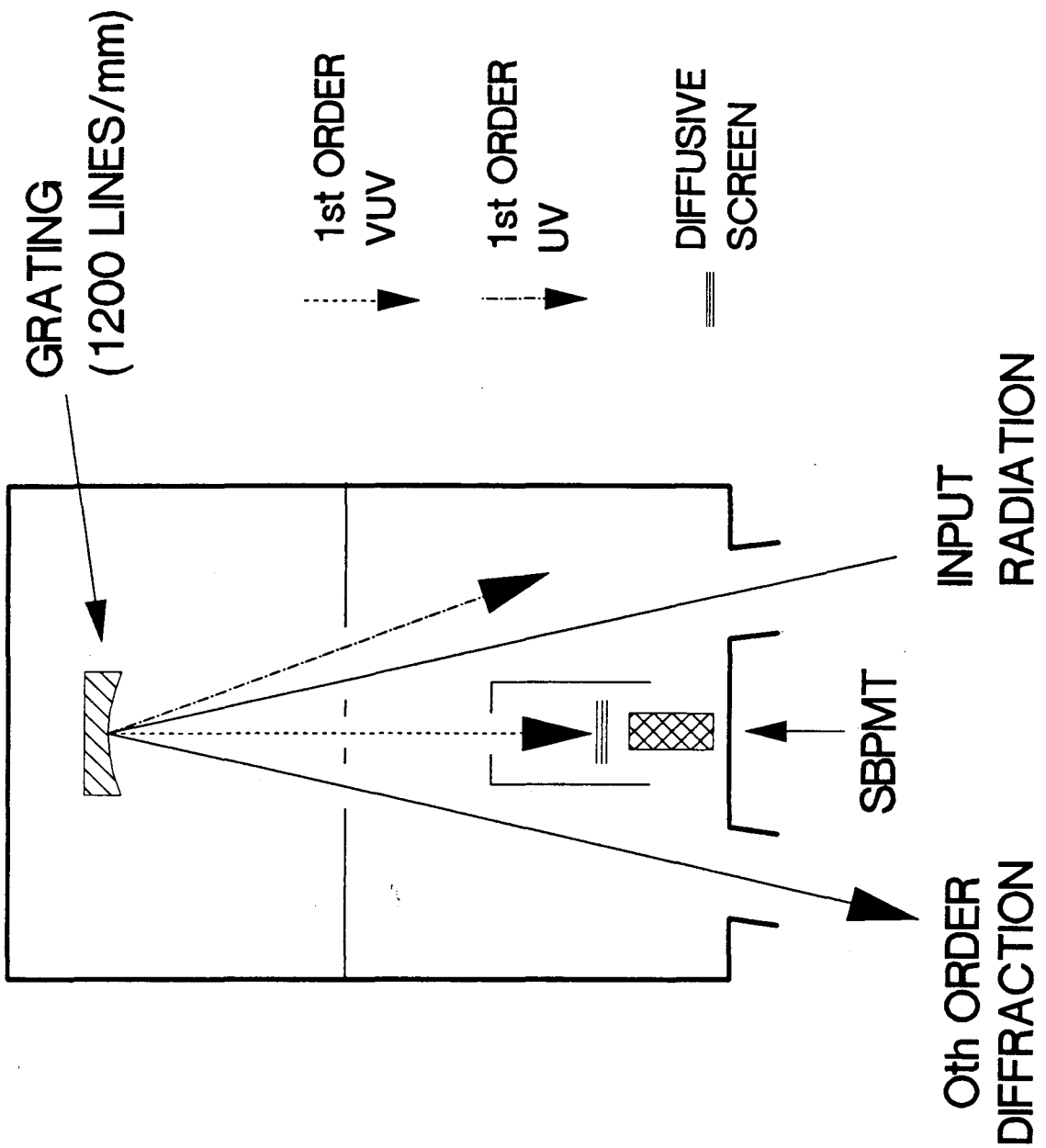

Figure 13. Set-up of the solar-blind photomultiplier tube (SBPMT) in the vacuum monochromator for vuv normalization. The large arrows indicate the directions of the different diffraction orders for a 1200grooves/mm grating. Layers of a fine mesh screening were used to attenuate the vuv intensity at the SBPMT.

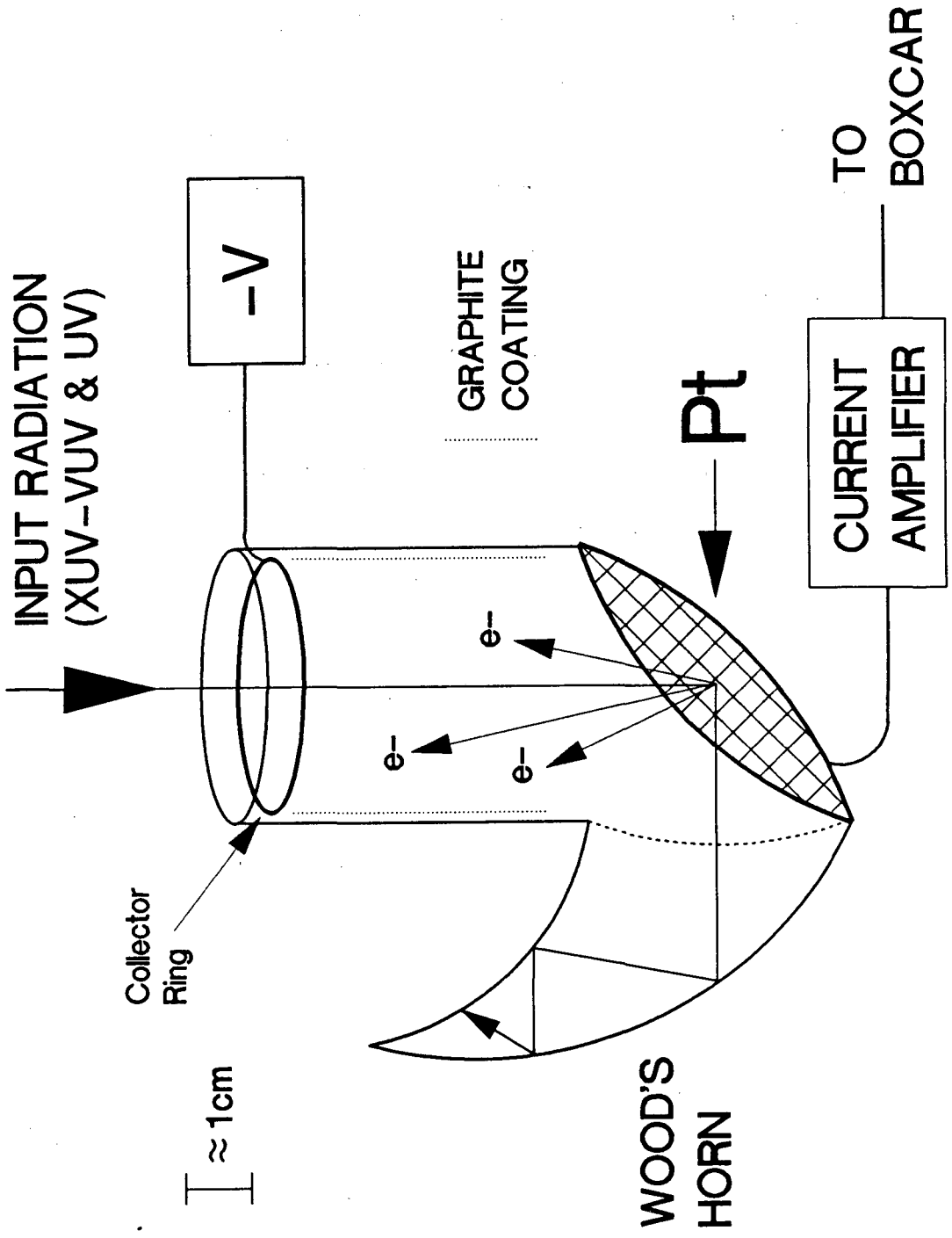

Figure 14. Schematic of the Pt. Photo Diode used to measure vuv and xuv radiation intensity. The main body (shown roughly to scale) is constructed of glass and the Pt is held in place with wire. -V=low voltage power supply, CR=electron collector ring.

effect which are then collected by a metal ring. The current generated is then amplified via a low background/high gain amplifier. In this design the uv light is discriminated against by two methods. The high work function of the Pt metal (6eV) prohibits electrons from being ejected by the uv photons. In practice there is a fair amount of background electrons from the uv generated either by tunneling, impurities in or on the Pt surface or multi-photon effects. To further reduce this signal a negative bias is applied to the collector ring. Since electrons generated by uv light will be much lower in energy than those generated by vuv photons they will not be able to overcome as high an electric field gradient. Application of a -0.5 to -2.0 volt bias is enough to reduce the uv background signal to tolerable levels. This bias is generally adjusted to maximize the ratio between vuv and uv signal.

III. LASER PERFORMANCE

A. VISIBLE

Through three stages of the amplifier chain a gain of approximately 10^8 is obtained with a Nd:YAG pump laser energy of 450mJ per pulse at 532nm. The pump energy is distributed in the ratio of 1:8:91 resulting in a gain of 10^3, $3x10^3$ and 33 for the three stages respectively. For

less efficient dyes the middle cell can be pumped harder, if needed, by increasing the reflectance of the beam splitter which directs the Nd:YAG beam into that cell. The laser system has been operated in the visible from 548nm to 725nm using R560, R590 and DCM and LDS698 dyes in the c.w. dye laser and various other dyes in the amplifiers. The power output curves for these dyes under normal operating conditions are shown in Figure 15. For FL548 and LDS750 the laser output was measured only at a single wavelength. The dashed curves in Figure 15 for these dyes are estimated response curves (from Exciton) scaled to the measured energy point. The concentrations of the different dyes used in the three cells are listed in Table I.

TABLE I: DYE CONCENTRATIONS FOR AMPLIFIER SYSTEM

DYE	1mm CELL (MOLES/LITER)	3mm CELL (MOLES/LITER)	6mm CELL (MOLES/LITER
FL548	1.0×10^{-3}	4.7×10^{-4}	2.7×10^{-4}
R590	2.2×10^{-4}	8.3×10^{-5}	4.4×10^{-5}
R610*	1.7×10^{-4}	6.2×10^{-5}	4.0×10^{-5}
KITON RED	2.5×10^{-4}	9.0×10^{-5}	4.0×10^{-5}
R640*	1.9×10^{-4}	7.6×10^{-5}	5.1×10^{-5}
SR640	2.6×10^{-4}	1.1×10^{-4}	6.7×10^{-5}
DCM	5.8×10^{-4}	2.2×10^{-4}	1.2×10^{-4}
LDS688	2.4×10^{-4}	7.6×10^{-5}	5.4×10^{-5}
LDS750	4.1×10^{-4}	6.8×10^{-5}	2.3×10^{-5}

*Denotes Basic Solution

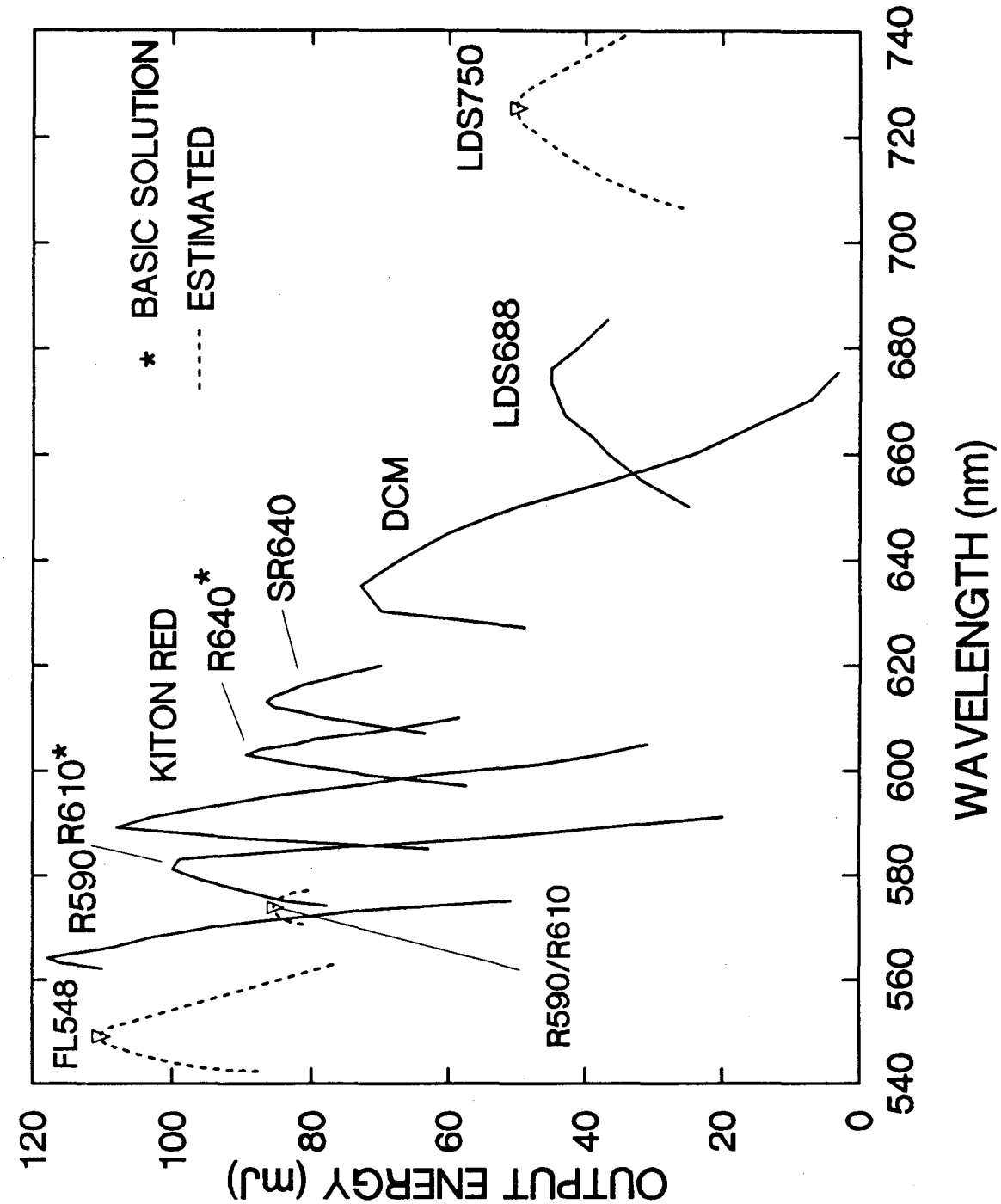

Figure 15. Output response curves of the dye laser for various dyes. The dashed lines are estimated response curves (from Exciton) scaled to the measured output energy (▽). R590/R610 denotes R610 in the final amplifier only (discussed in text) and * denotes basic solution.

The maximum output obtained so far has been 135mJ at 568 nm, the peak of R590 dye. However, at this power the beam contains some hot spots in its spatial profile. Under operating conditions that result in a uniform beam, the pulse energy is approximately 10% less than the maximum energy obtainable. ASE is depleted by the amplified c.w. beam to less than 10% of the measured energy over most (≈90%) of the tuning range. Near the edge of the range the ASE can be effectively subdued by using a different dye in the final amplifier (as shown in Figure 15 for the R590/R610 combination where R610 is used in the final amplifier). The depletion of the ASE in the dye amplifier chain as a function of wavelength for the dyes R6G and R610 is shown in Figure 16.

The final near-field beam profile is a circle 6mm in diameter with hard edges and a few diffraction rings. The diffraction rings come from the aperturing of the near-Gaussian beam by the bore of the amplifier cells. These rings can be minimized by reducing the c.w. laser beam diameter. However, this causes a loss in output power of 20% or greater. A compromise between spatial beam quality (both uniformity and extent of diffraction rings) and pulse energy is required.

As discussed above (§II.D), the actual modeling of the energy extraction process in a dye cell is a very complicated procedure and is beyond the scope of this

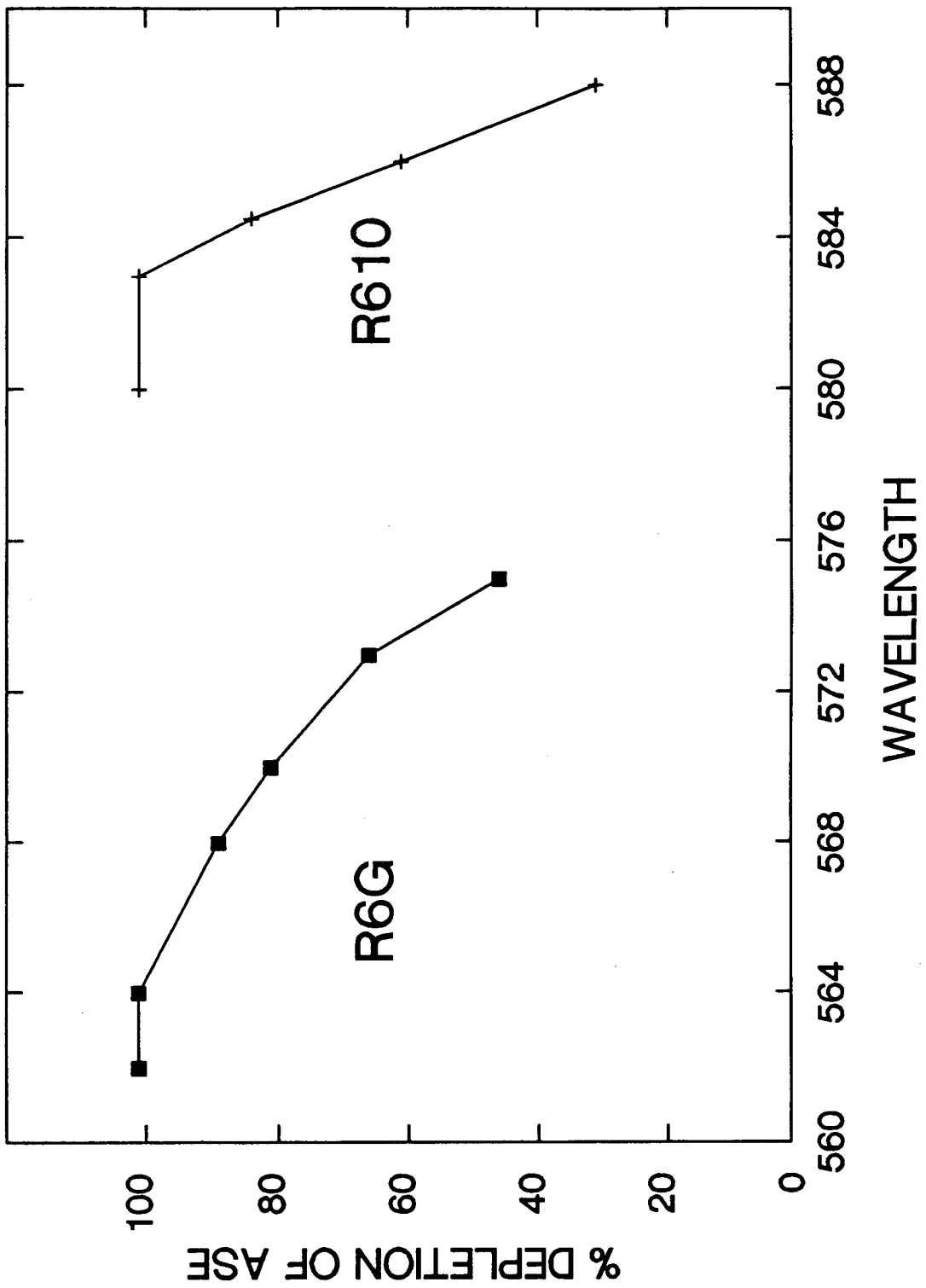

Figure 16. Percent depletion of amplified spontaneous emission (ASE) in the dye amplifier chain for R6G and R610 (100% = ASE completely depleted).

thesis. A measure of the performance of each of the dye cells can be obtained by calculating the ratio of extracted energy to the energy available. The analysis presented below is for a steady state extraction. While this assumption is not quite valid for the amplifier cells it simplifies the calculation and provides a feeling for the relative performance of the different cells.

If one assumes that the pump pulse has a square temporal profile and pumps the dye cell uniformly then the population difference (per cm^3), ΔN_{12}, can be estimated by:[51]

$$\Delta N_{12} = R_p * \tau_2 * [1 - e^{-T_p/\tau_2}] \qquad (14)$$

where R_p=pump photons absorbed per second per cm^3, τ_2=lifetime of the upper state and T_p=pump pulse length. This further assumes that the lower state is rapidly depopulated so that its population is essentially zero. The available energy is then given by:

$$I_{avail} = \frac{\Delta N_{12} * \hbar\omega}{\tau_2} * L \qquad (15)$$

where L=length of the dye cell. The extraction efficiency, η, for each cell is calculated from the known input intensity (I_{in}) and output intensity (I_{out}) as follows:

$$\eta = \frac{I_{out} - I_{in}}{I_{avail}} \qquad (16)$$

The results of the calculations performed for the three dye cells (using R590 dye) along with the parameters used are presented in Table II.

Table II: Dye Cell Extraction Efficiency Calculations			
τ_2 T_p Pump Energy Extraction λ	5.5×10^{-9} sec 1.0×10^{-8} sec 450mJ @ 532nm 575nm		
	1mm Cell	3mm Cell	6mm Cell
Pump Energy	2mJ	36mJ	412mJ
Length(L)	1.5cm	3cm	6cm
$\Delta N_{12}(cm^{-3})$	2.06×10^{17}	2.10×10^{17}	2.99×10^{17}
$I_{avail}(W/cm^2)$	1.9×10^{7}	4.0×10^{7}	1.1×10^{8}
$I_{in}(W/cm^2)$	38	4.2×10^{3}	1.1×10^{6}
$I_{out}(W/cm^2)$	3.8×10^{4}	4.2×10^{6}	3.6×10^{7}
η	1.8×10^{-3}	0.10	0.32

The temporal profiles of the Nd:YAG and pulsed dye laser beams are shown in Figure 17. The dye pulse shows significant deviation from the near Gaussian profile of the pump beam. The fast rise in the front end of the pulse is caused by the exponential gain of the amplifiers. Double passing the second amplifier contributes to the slight broadening at the top. The steep fall and shortening of the pulse to 6.5ns is due to gain saturation in the second and final amplifiers. These factors will contribute to the spectral broadening of the pulse discussed below.

Bandwidth measurements were done with two different confocal etalons: a 300MHz FSR étalon with a finesse of 100

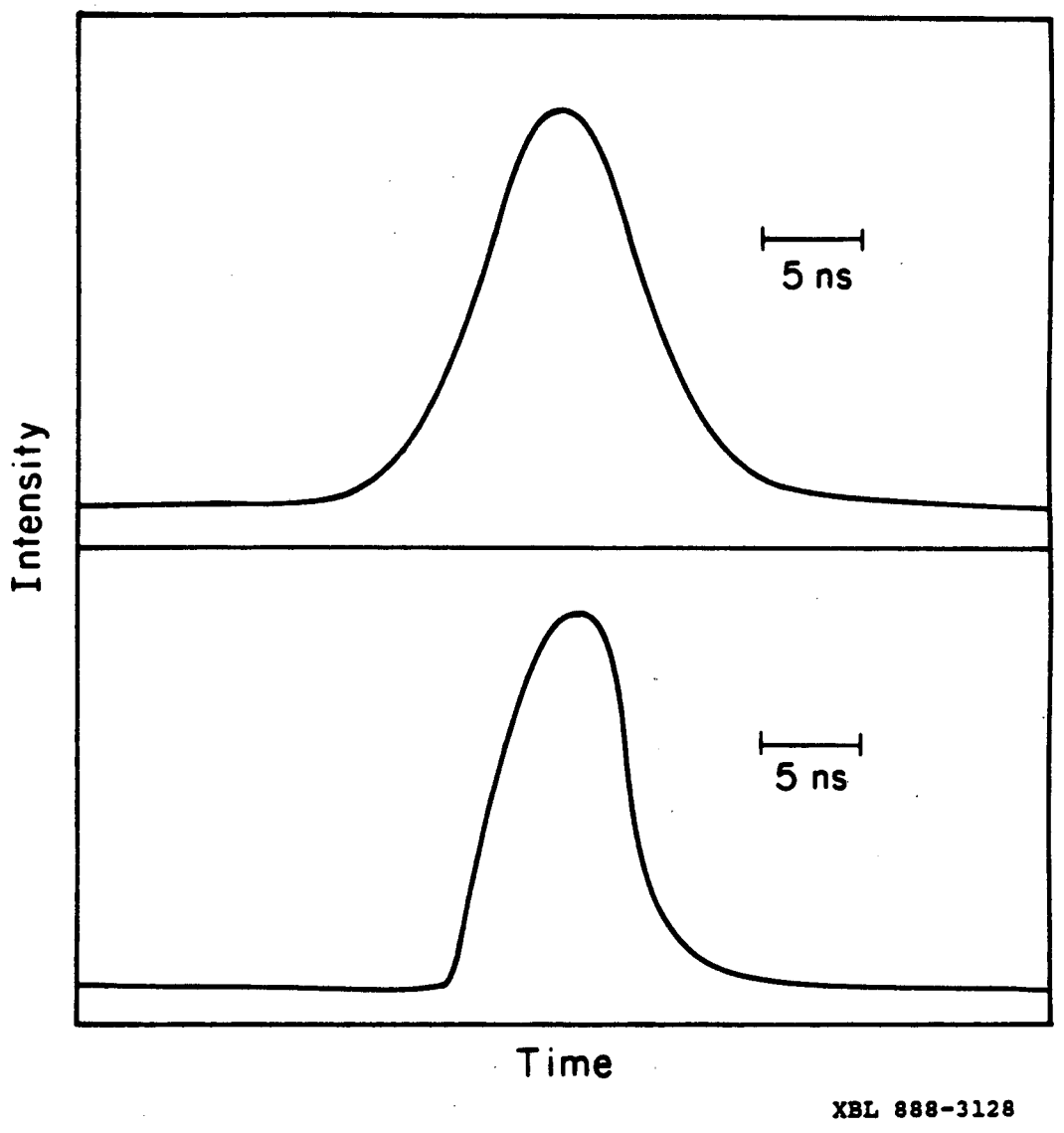

Figure 17. Upper trace: temporal profile of the injection-seeded Nd:YAG laser pulse (FWHM=10ns). Lower trace: temporal profile of the dye laser pulse (FWHM=7ns).

and a 1.5GHz FSR étalon with a finesse of 130. In both cases the c.w. and pulsed signals through the etalons were measured simultaneously as the c.w. dye laser was scanned. The pulse bandwidth, measured with R590 dye in the amplifiers, was found to be 91MHz (see Figure 18). In comparison, the Fourier transform-limited bandwidth for a Gaussian pulse 7ns wide is 32MHz. The discrepancy between these two numbers is consistent with that observed in other pulse-amplified single-mode systems.[3] An important contributing factor to the larger than transform-limited bandwidth is the exponential dye gain that produces the non-Gaussian temporal profile of the pulse described above. This profile, in turn, is dependent on the amplifier dye. Thus slightly different bandwidths are observed in the other dyes used. No power broadening of the bandwidth is seen. In fact, a gain narrowing effect of roughly 5-10% occurs when the pump power is increased. Hence the entire origin of the broadening is still not well understood. Frequency pulling of the amplified beam was also seen. The amplified beam was shifted by a few MHz to the blue of the c.w. beam. This effect has been observed previously[52] and attributed to a Stark shift by the high electric field produced in the dye by the pump laser. However, in our laser the pump beams are not focused in the dye cells so the electric field strength is much lower then in conventional dye cells. We have observed that this shift is configuration and dye

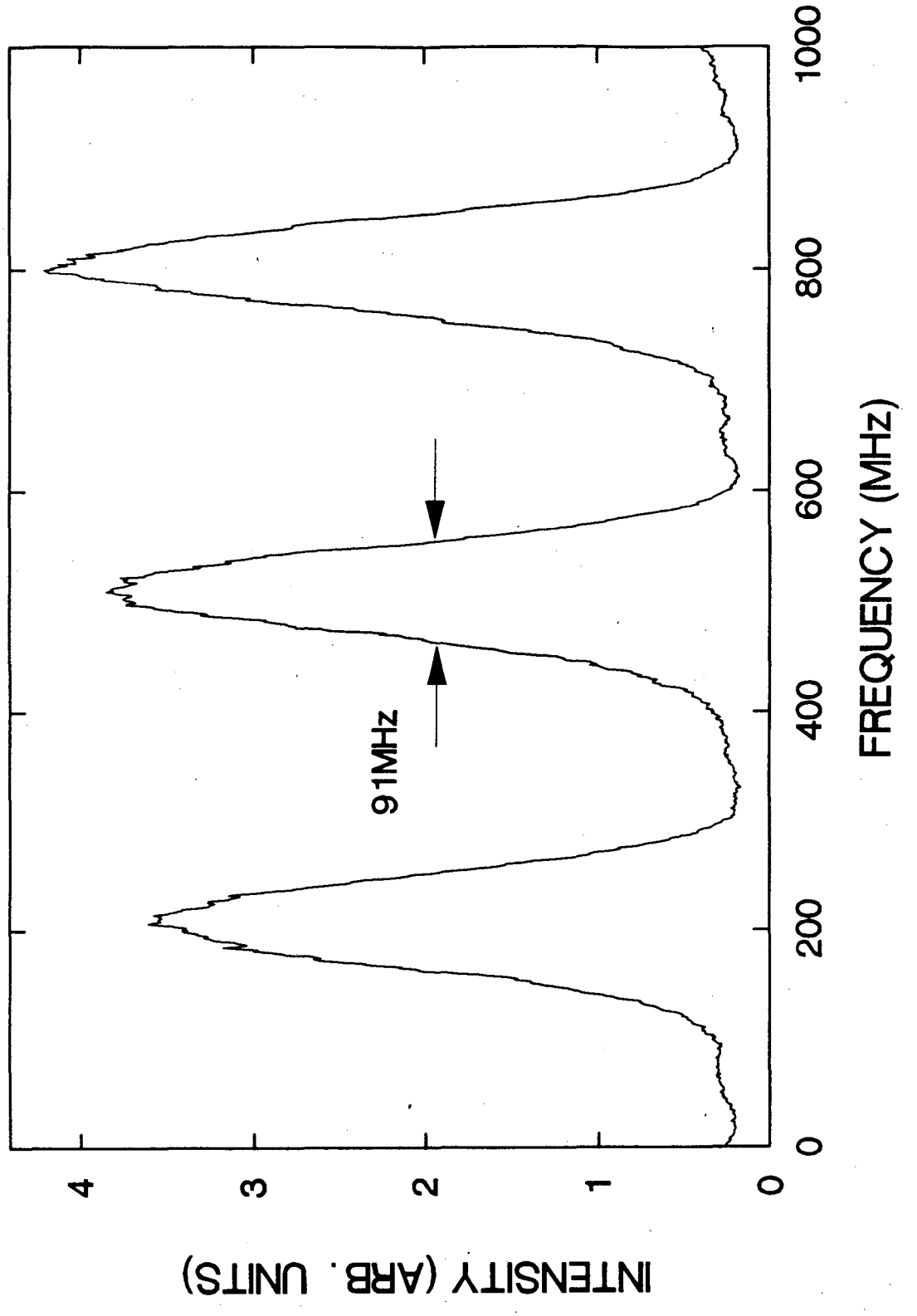

Figure 18. Scan of the pulsed dye laser through a 300-Mhz étalon with R590 dye in the amplifiers. (FWHM=91MHz).

dependent. For high absolute accuracy the shift must be measured for the experimental conditions used.

The present scanning capabilities are set by the 699-29 laser. These include a minimum step interval of 1MHz and a slowest scanning speed of 10MHz per second. As of this writing a new computer control unit for the 699-29 laser system has been developed by Coherent affording much more versatility in the scanning capabilities of the laser.

B. ULTRAVIOLET

As mentioned previously second harmonic generation is accomplished in KDP crystals. The maximum conversion efficiency measured (after reflection losses at optical surfaces were accounted for) was 40% with a well collimated beam. During operation, when the beam must be slightly diverging for the doubling units to track, the conversion efficiency is around 30-35%. The uv beam profile is very similar to that of the visible beam with the diffraction rings being more pronounced.

Extension to shorter uv wavelengths from 230nm to 200nm is accomplished by two techniques. The first involves mixing the frequency doubled dye output with the residual 1064nm beam from the Nd:YAG laser in an angle tuned β-Barium Borate (BBO) crystal. Pulse energies of about 5mJ have been obtained using this set-up. This conversion is limited by the divergence and large spot size of the IR beam

($dia_{ir} > 2dia_{uv}$). The second method involves doubling the visible beam and then mixing the generated uv radiation with the residual visible light in a BBO crystal. To accomplish this the visible light is separated from the uv beam via dichroic mirrors, its polarization is rotated by 90° with a $1/2\lambda$ Fresnel Rhomb, and then the two beams are recombined and sent through the mixing crystal. A schematic of this arrangement is shown in Figure 19.

There are certain advantages associated with the tripling technique as opposed to the infra-red mixing method for generating far uv radiation. The wavelength of the tripled light is known to the accuracy of the 699 wavemeter. While the 1064nm radiation has the same bandwidth as the visible light, giving single-mode far uv, its absolute frequency is not known to any precision so the frequency of the uv light is also unknown. The wavelength can be calibrated but since the frequency of the Nd:YAG laser changes every hour or so due to mode hops performing an experiment which requires knowledge of the absolute frequency, or even relative frequency, of the laser is extremely difficult. The conversion efficiency achieved by straight tripling is also better. The main reason for this is a much better spatial and temporal overlap of the mixed beams (visible and uv) since they come from the same source. Pulse energies of up to 10mj have been achieved at wavelengths around 212nm and 204nm utilizing the frequency

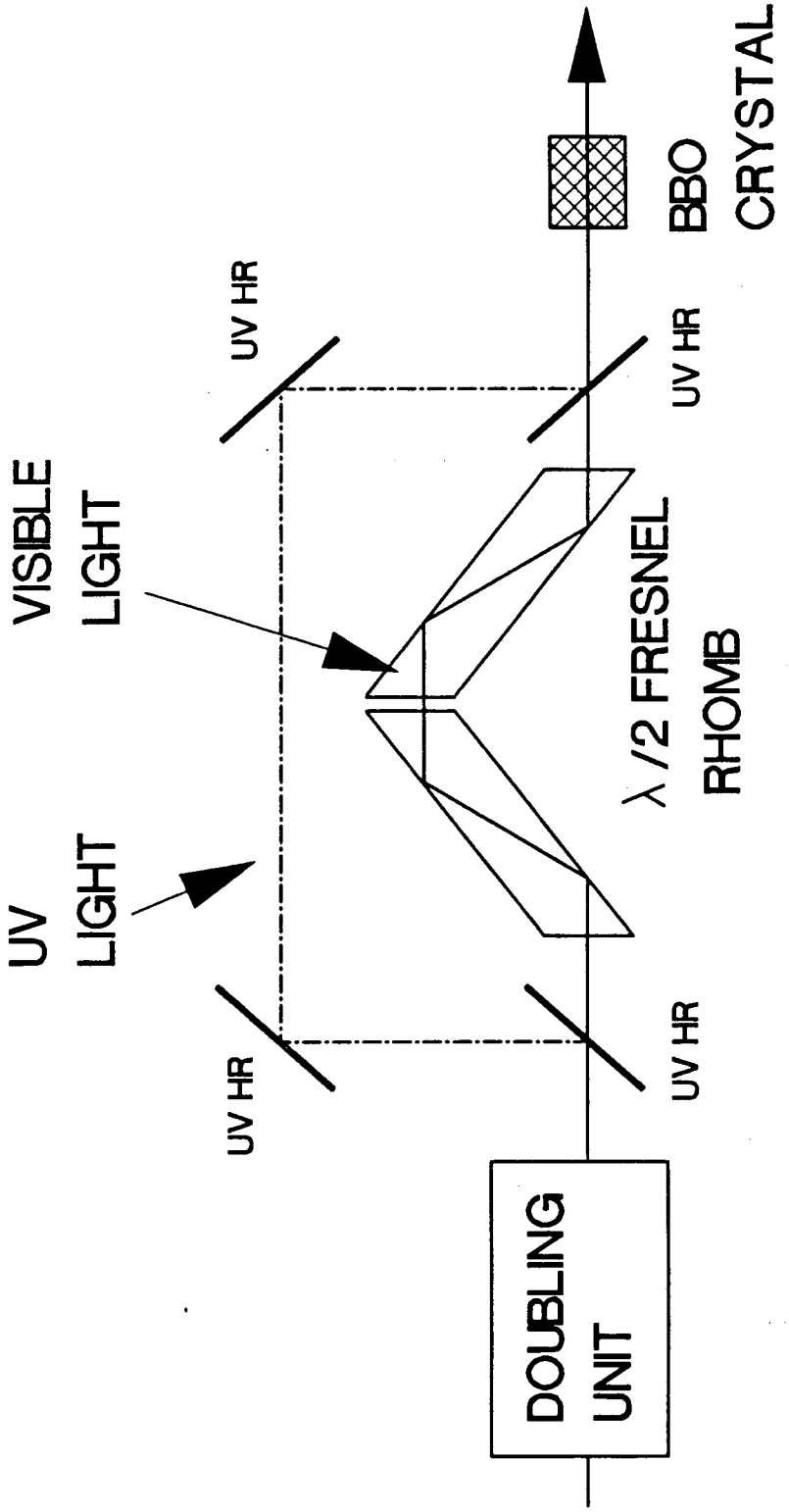

Figure 19. Schematic of the set-up for uv+vis mixing in a β-barium borate (BBO) crystal. UV HR=uv high reflectance/visible high transmittance beam splitter.

tripling technique. A complete summary of the uv powers obtained are given below in Table III.

TABLE III: UV PERFORMANCE OF LASER SYSTEM

Wavelength Region	Crystal Type	Pulse Energy	Mixing Scheme	Conversion Efficiency
310nm-350nm	KDP-C	10-20mJ	1+1	12%-30%
310nm-290nm	KDP-R6G	20-35mJ	1+1	20%-35%
290nm-270nm	KDP-B	20-40mJ	1+1	25%-40%
220nm-225nm	BBO	2-5mJ	$2+1_{IR}$	≈10%*
		3-8mJ	$2+1_{VIS}$	≈20%*
210nm-215nm	BBO	4-10mJ	$2+1_{VIS}$	≈20%*
200nm-205nm	BBO	3-8mJ	$2+1_{VIS}$	≈12%*

*With respect to uv power.

C. VUV & XUV

The efforts to produce high power single-mode visible and uv light with good spatial control are to ensure a good conversion efficiency in generating single-mode vuv and xuv radiation.

A lens, of variable focal length, is used to focus the input beams at the pulsed molecular jet several mm downstream from our home-made pulsed nozzle source. Typically a 25cm fl singlet lens is used for straight tripling while a 30cm fl achromat is used for sum frequency mixing. The generated radiation and the fundamental beam(s) are dispersed by the differentially-pumped monochromator. This source has been tuned from wavelengths around 124nm to wavelengths around

74nm. When mixing of two lasers is called for the use of both legs of the laser system allows generation of tunable radiation while maintaining a narrow bandwidth. For certain applications a Quanta-Ray DCR-2 Nd:YAG/PDL dye laser system can also be used as the second laser. Table IV summarizes the wavelengths we have studied to date, showing the generation scheme used, the generating medium and the incident pulse energies.

TABLE IV: EXAMPLES OF WAVELENGTHS GENERATED

λ (nm)	υ (cm^{-1})	υ_{vis} (cm^{-1})	AMP. DYE	MIXING SCHEME	MIXING MEDIUM
123.6	80917	17578	R590	$3\upsilon_{uv}$	CO
117.8	84910	16982	K. R.	$2\upsilon_{uv}+\upsilon_{vis}$	Xe
116.5	85847	17169	R610	$2\upsilon_{uv}+\upsilon_{vis}$	Xe
100.1	99894	16649	R640	$3\upsilon_{uv}$	Ar
98.5	101530	16922	K. R.	$3\upsilon_{uv}^{*}$	CO
98.2	101868	16978	K. R.	$3\upsilon_{uv}$	Ar
95.1	105146	17524	R590	$3\upsilon_{uv}$	Xe
80.4	124344	υ_1=17768 υ_2=17242	R590 R590	$2\upsilon_{uv1}+\upsilon_{uv2}$	Xe
74.2	134792	17768	R590	$3\upsilon_{uv1}$	Xe

*2-Photon Resonant Mixing K.R. = Kiton Red

$\upsilon_{uv}=2\upsilon_{vis}$

$\upsilon_{uv1}=2\upsilon_1+\upsilon_{ir}$ (υ_{ir}=Nd:YAG fundamental)

$\upsilon_{uv2}=2\upsilon_2$ (Second Laser)

Continuous tuning is accomplished either by scanning the cw dye laser (MHz resolution) or, when mixing, the second laser whether it be the other cw dye laser or the PDL ($1cm^{-1}$ resolution). Other wavelengths can be obtained

easily by choosing the appropriate input wavelengths and generating medium. The narrowest laser bandwidth achieved has been by non-resonant third harmonic generation of the near-transform limited beam pumped by the single-mode Nd:YAG laser. To test the spectral resolution we scanned the 4p-7s $^2P_{3/2}(J=1)$ transition of ^{86}Kr in a collimated atomic beam with a 30MHz Doppler width at 94.5nm using this source. The vuv monochromator was set at 1st order. Detection was by ionization of the excited Kr atom with a second uv laser beam maintained at well below 1mJ to minimize power broadening. After correcting for contributions from Doppler broadening we calculate that the xuv bandwidth is 210MHz.[1]

The high brightness of our uv beam and the improved valve helped to increase the vuv-xuv output compared to previously obtained signals by as much as two orders of magnitude. The output reported in Table V is what is available at the input to the monochromator and is representative of most of the wavelengths we have studied. The number of photons/pulse was derived from measurements of direct ionization of NO made with a single ion chamber.[53] This beam intensity was accomplished through non-resonant tripling in Ar. The relative non-resonant straight tripling intensities follow closely the tuning curves of Reference 28. Variation in the vuv intensity is determined primarily by the positions of the atomic resonances. Relative single laser sum frequency mixing output agrees with the curves

measured by Hilbig and Wallenstein[39] with peak intensities at $>10^{11}$ photons/pulse. In the shorter wavelength region, where resonant two-photon mixing in Xe is utilized, the output is proportional to the power and tuning range of the non-resonant laser. The actual usable output for all wavelengths is determined by the reflectivity and efficiency of the monochromator grating. This is estimated to vary from ≈20% at >120nm to ≈1.5% at 74nm.

In some cases, we have observed gas breakdown at the focal point of the uv beam as a result of its high brightness. This causes spectral broadening of the vuv beam. The problem is remedied by increasing the distance between the pulsed nozzle and the laser focal point. This necessarily reduces the output power of the vuv and must be taken into account when using the source.

D. OTHER RESULTS

In addition to the efforts to make short wavelength radiation discussed above other non-linear mixing techniques, such as difference frequency mixing and stimulated Raman scattering, have been used to generate infra-red radiation and also some uv light. The set-up for these processes are described in detail elsewhere[54] so only a brief summary will be given here.

Radiation around 1.6μm was generated by difference frequency mixing in a $LiNbO_3$ crystal. Approximately 70mJ of

650nm light (produced with DCM in both the 699 and the dye amplifiers) was mixed with 80mJ of 1064nm light (S-M Nd:YAG fundamental) making 7mJ of single-mode 1.6μm radiation. The mixing was done in an IR-WEX unit (Spectra-Physics). The major limitation on conversion efficiency in this process was the divergence of the 1064nm beam.

Radiation around 1.13μm was generated in two fashions, both utilizing difference frequency mixing. In the first attempt 6mJ of 363nm light was mixed with the second harmonic of the S-M Nd:YAG (532nm) in a Type II process to produce only $\approx$250μJ of 1.14μm light. The 363nm radiation was generated by doubling 50mJ of 726nm light from the dye laser system (using LDS698 in the 699 and LDS750 in the dye amplifiers) in a KDP crystal. The difference mixing was done in the 3rd Harmonic generation crystal (KDP) of the Quantel Nd:YAG laser.

The second, more successful, attempt to generate 1.13μm light used difference frequency mixing with the Nd:YAG fundamental. In this scheme $\approx$100mJ of 549nm light from the laser system (using R560 in the 699 and FL548 in the amplifiers) was mixed with $\approx$200mJ of 1064nm radiation from the S-M Nd:YAG laser in a Type I mixing process in a KDP crystal. A maximum of 15mJ of 1.13μm light was generated in this manner. The major drawback in this set-up was the lifetime of the R560 dye in the 699 laser ($\tau_{1/2}\approx$1day). The dye could be revitalized with the addition of a few drops of

HCl. This would approximately double the dye's lifetime.

Stimulated Raman scattering in room temperature H_2 was used to generate a number of different wavelengths. A 25cm focal length lens was used in all the set-ups discussed below. The 1st Stokes of 645nm light (at 880nm) was generated as follows: 80mJ of 645nm light was focused into 1.5Atm of H_2 making 10mJ of 880nm radiation. The 1st and 2nd Stokes of 585nm light (at 772nm and 1.14μm respectively) was generated as follows: 100mJ of 585nm light was focused into 2Atm of H_2 resulting in 15mJ of 772nm and 9mJ of 1.14μm radiation. The 1st anti-Stokes of 290nm light (at 259nm) was generated as follows: 25mJ of 290nm light (generated by doubling 100mJ of 580nm light in KDP) was focused into 1.5Atm of H_2 to make 0.4mJ of 259nm radiation. A summary of the laser's performance is given in Table V.

TABLE V: LASER SYSTEM PERFORMANCE

	I-R	Visible	U.V.	VUV-XUV
ENERGY	5-15mJ	>100mJ	>30mJ(2x) <10mJ(3x)	$>10^{11}$ ph/pulse^{+}
BANDWIDTH (FWHM)	>91MHz	91MHz	<140MHz*	210MHz
PULSE LENGTH	<7ns	7ns	<7ns*	<7ns*
TUNING RANGE (TO DATE)	880nm-1.6μm	546-700nm	273-350nm 200-240nm	74-124nm
TEMPORAL PROFILE	NEAR GAUSSIAN	NEAR GAUSSIAN	NEAR GAUSSIAN	NEAR GAUSSIAN

$^{+}$Measured @ 982nm
*Estimated

IV. SUMMARY

This chapter has described a laser system capable of continuously scanning over much of the visible, uv, vuv and xuv spectral regions with high pulse energy and a near transform-limited bandwidth. A second pulse-amplified single-mode dye laser adds to the tunability and versatility of the laser system by allowing the use of mixing schemes to make xuv light. This system provides nearly full, single frequency, coverage of the entire spectrum discussed above. Future plans include the use of high power excimer lasers to facilitate efficient pumping of dyes in the blue-green region, use of tunable solid-state amplifiers and the use of high repetition rate pump lasers for higher average power.

REFERENCES

1. See also, E. Cromwell, T. Trickl, Y.T. Lee, and A.H. Kung, Rev. Sci. Inst. **60**, 2888 (1989).

2. M.M. Salour, Opt. Commun. **22**, 202 (1977).

3. P. Drell and S. Chu, Opt. Commun. **28**, 343 (1979).

4. Tim Johnston, Jr., R.H. Brady, and W. Proffitt, App. Opt. **13**, 2307 (1982).

5. CR 699-29 Autoscan: Operator Manual, Coherent Inc., 3210 Porter Dr., Palo Alto, CA 94304.

6. W.B. Bridges, Appl. Phys. Lett. **4**, 128 (1964); erratum: Appl. Phys. Lett. **5**, 39 (1964).

7. R.J. Pressley, Ed., Handbook of Lasers with Selected Data on Optical Technology (CRC Press, Cleveland, 1971), ppg. 242-297.

8. Innova 100 Series Ion Laser: Operator Manual, Coherent Inc., 3210 Porter Dr., Palo Alto, CA 94304.

9. A.G. Fox and T. Li, Bell Syst. Tech. J. **40**, 453 (1961).

10. F.R. Faxvog, Opt. Lett. **5**, 285 (1980).

11. A.E. Siegman, Lasers (University Science Books, Mill Valley, CA, 1986), ppg. 532-538.

12. C.T. Pike, Opt. Commun. **10**, 14 (1974).

13. W. Koechner, Solid-State Laser Engineering, **Springer Series in Optical Sciences, Vol. 1** (Springer-Verlag, New York, 1978).

14. F.A. Jenkins and H.E. White, Fundamentals of Optics (McGraw-Hill Book Company, New York, 1957).

15. L. Rahn, private communication.

16. L.J. Aplet and J.W. Carson, Appl. Opt. **3**, 544 (1964).

17. P.C. Fletcher and D.C. Weisman, Appl. Opt. **4**, 867 (1965).

18. M. Born and E. Wolf, Principles of Optics (Pergamon Press, New York, 1980), ppg. 435-442.

19. T.J. Kane and R.L. Byer, Opt. Lett. **10**, 65 (1985).

20. S-100 Injection Seeding System: User's Manual, Lightwave Electronics Corp., 1161 San Antonio Rd., Mountain View, CA 94043.

21. D.S. Bethune, App. Opt. **20**, 1897 (1981).

22. C. Rolland and P.B. Corkum, Opt. Commun. **59**, 64 (1986).

23. R. Falcone, private communication.

24. U. Ganiel, A. Hardy, and D. Treves, IEEE J. Quantum Elec. **QE-11**, 881 (1975).

25. W. Demtröder, Laser Spectroscopy: Basic Concepts and Instrumentation, **Springer Series in Chemical Physics, Vol. 5** (Springer-Verlag, New York, 1982), ppg. 358-370.

26. H. Rabin and C.L. Tang, Eds., Treatise in Quantum Electronics 1, Nonlinear Optics, Parts A and B (Academic Press, New York, 1975).

27. A.H. Kung, Opt. Lett. **8**, 24 (1983).

28. J. Bokor, P.H. Bucksbaum and R.R. Freeman, Opt. Lett. **8**, 217 (1983).

29. R.H. Page, R.J. Larkin, A.H. Kung, Y.R. Shen and Y.T. Lee, Rev. Sci. Instrum. **58**, 1616 (1987).

30. C.T. Rettner, E.E. Marinero, R.N. Zare, and A.H. Kung, J. Phys. Chem. **88**, 4459 (1984).

31. D.S. Bethune and C.T. Rettner, IEEE J. Quantum Elec. **23**, 1348 (1987).

32. G.C. Bjorklund, IEEE J. Quantum Elec. **QE-11**, 287 (1975).

33. C.R. Vidal, App. Opt. **19**, 3897 (1980).

34. J. Reintjes, App. Opt. **19**, 3889 (1980).

35. R.B. Miles and S.E. Harris, IEEE J. Quantum Elec. **QE-9**, 470 (1973).

36. P.R. Herman, P.E. LaRocque, R.H. Lipson, W. Jamroz, and B.P. Stoicheff, Can. J. Phys. **63**, 1581 (1985).

37. J.F. Ward and G.H.C. New, Phys. Rev. **185**, 57 (1969).

38. L. Cabaret, C. Delsart and C. Blondel, Opt. Commun. **61**, 116 (1987).

39. C.H. Muller III, D.D. Lowenthal, M.A. DeFaccio, and A.V. Smith, Opt. Lett. **13**, 651 (1988).

40. R. Hilbig and R. Wallenstein, App. Opt. **21**, 913 (1982).

41. K.D. Bonin and T.J. McIlrath, J. Opt. Soc. Am. B **2**, 527 (1985).

42. R. Hilbig and R. Wallenstein, IEEE J. Quantum Elec. **QE-19**, 194 (1983).

43. F. Aguillon, A. Levéhot, J. Rousseau, and R. Camparque, J. Chem. Phys. **86**, 5246 (1987).

44. F. Vallée, S. Wallace, and J. Lukasik, Opt. Commun. **42**, 148 (1982).

45. F. Merkt and T.P. Softley, Chem. Phys. Lett. **165**, 477 (1990).

46. K. Tsukiyama, M. Tsukakoshi, and T. Kasuya, Appl. Phys. B **50**, 23 (1990).

47. K. Tsukiyama, T. Munakatam, M. Tsukakoshi, and T. Kasuya, Chem. Phys. **121**, 55 (1988).

48. K. Tsukiyama, M. Tsukakoshi, and T. Kasuya, J. Chem. Phys. **92**, 6426 (1990).

49. D. Proch and T. Trickl, Rev. Sci. Inst. **60**, 713 (1989).

50. L. Tonkyn and M.G. White, Rev. Sci. Inst. **60**, 1245 (1989).

51. "Lasers," Siegman, ppg. 292-304.

52. C. Wieman and T.W. Hansch, Phys. Rev. A **22**, 192 (1980).

53. J.A.R. Samson, Techniques of Vacuum Ultraviolet Spectroscopy (Wiley, New York, 1967), pg. 266.

54. D.-J. Liu, A. Stolow, M.J.J. Vrakking, E. Cromwell, A.H. Kung, and Y.T. Lee, (to be published).

CHAPTER III

DYNAMICS OF H_2 ELIMINATION FROM CYCLOHEXADIENE

I. INTRODUCTION

Knowledge of the potential energy surface in the transition state region is paramount in understanding reaction dynamics. In a concerted decomposition eliminating a molecular product the configuration of the molecule at the transition state plays an important role in determining how the released energy is distributed among the different degrees of freedom of the products. For example, in the H_2 elimination from 1,4-cyclohexadiene (CHDN), the structure near the transition state will have cyclohexadiene in a boat form with the two hydrogen atoms attached to the 3 and 6 positions pushed toward each other. There are two coordinates which are important in determining the final internal state and the translational energy of the H_2 products. The distance between two H atoms in the transition state region determines the final vibrational excitation of the H_2 product and the separation between the "H_2" and the departing carbon atoms determines the repulsive energy released in the product formation. By measuring the translational, vibrational and rotational energy of the H_2 products one can deduce the structure of the transition state region especially related to the two orthogonal coordinates mentioned above. Complete characterization of product state distributions and translational energy distributions is a powerful tool for indirect investigation of transition state regions.

Initial experiments of H_2 elimination from cyclic hydrocarbons in the Y.T. Lee laboratories were carried out in the photodissociation of cyclohexene, 1,4-cyclohexadiene and benzene.[1,2] In those studies angularly resolved, mass selected, time of flight product distribution measurements revealed the translational energy distributions of H_2 products which had an average translational energy around 25 kcal/mole and clearly indicated a strong repulsion between H_2 and the other products. However, it was not possible to estimate the extent of the vibrational and rotational excitation of H_2, nor can one understand whether the kinetic energy in H_2 is strongly coupled to the internal excitation.

Using an ultra-high resolution vacuum ultraviolet-extreme ultraviolet (vuv-xuv) laser system, described in the previous chapter, the relative populations of the different ro-vibrational states of H_2 molecules were investigated by applying state selective detection of H_2 via (1+1) resonance enhanced multi-photon ionization (REMPI).[3] In addition to the internal energy, the translational energy distributions of the H_2 products as a function of their quantum states have been obtained from the Doppler profile of the transitions and a correlation between translational and internal energy has been derived.

CHDN was chosen for this study because it has a "clean" H_2 elimination channel as shown in many previous investigations.[4,5,6,7,8,9,10,11] In considering the

photodissociation of CHDN three things stand out: H_2 is only eliminated in the electronic ground state through a concerted reaction, the ring opening channel does not subsequently yield any measurable amount of H_2, unless it reverses back to CHDN, and secondary H_2 elimination from benzene is not appreciable.[1,2] The H_2 $B^1\Sigma_g$ and $C^1\Pi_u$ electronic states are well characterized with the transition frequencies from the ground ($X^1\Sigma_g$) state known to $<0.1cm^{-1}$.[12] Furthermore, the oscillator strengths for transitions between nearly all the different ro-vibrational states are calculated to a high degree of precision[13] which allows us to estimate the quantum state distribution from the data obtained via the (1+1) REMPI.

Through-out the course of this experiment it was hoped that some insight would be gained into the nature of the transition state for the elimination of H_2 from 1,4-CHDN. From preliminary results, reported in an earlier communication,[14] and a more intensive study described in detail below it became clear that this reaction proceeds through a very tight and near symmetric transition state with both the H-H and H_2-C_6H_6 distances appearing to be short. Furthermore, a correlation between the recoil velocity vector (**v**) and the rotational angular momentum vector (**J**) of the H_2 product was also observed with $\mathbf{v} \parallel \mathbf{J}$ predominately. Two calculations on the transition state configuration and its normal modes have recently been

communicated to us.[15,16] These results agree very well with the observations reported here.

II. EXPERIMENTAL

The laser system used in this experiment has been described in Chapter II and elsewhere.[17] The molecular beam source used in this experiment has also been described previously.[18] Other details of the experimental set-up will be given below. A schematic of the experimental set-up is shown in Figure 1.

The CHDN is expanded through a 0.5mm diameter nozzle of a pulsed valve, designed by Proch and Trickl[19], into the source chamber the pressure of which is kept below 10^{-4} torr. The main chamber, which contains the interaction region, is differentially pumped and separated from the source chamber by a skimmer with a 2mm diameter aperture. The main chamber pressure was $\approx 5 \times 10^{-7}$ torr while running the beam source. The nozzle-skimmer distance was 2cm and the distance from the skimmer to the interaction region was 3cm. The CHDN beam was crossed with the laser beams at an angle of 98°. The Doppler shift due to the >90° angle and the Doppler broadening due to the molecular beam divergence was negligible compared to that caused by the velocity spread of the H_2 products.

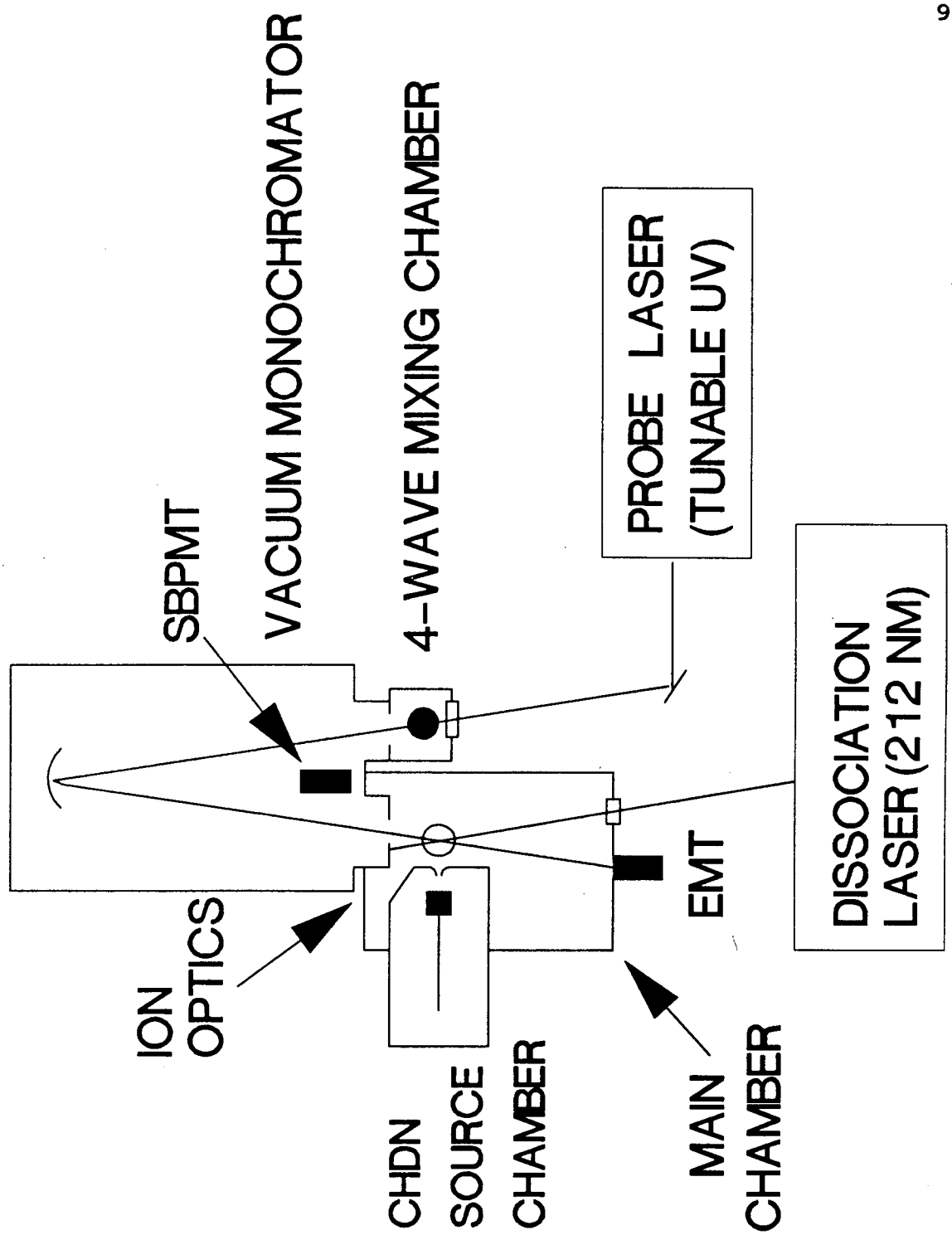

Figure 1. Schematic of the experimental set-up for the detection of H_2 product from the dissociation of 1,4-CHDN. SBPMT=Solarblind photomultiplier tube, EMT=Electron multiplier tube.

The ion optics used for the detection of the products were the same as described previously.[20] A schematic of the full ion detection apparatus is shown in Figure 2. There was a 1500V drop across the interaction region and ions were eventually accelerated to 2500 eV into the drift region. The ions of different mass were separated by time of flight along the 1m path to the detector (the quadrupole shown in Figure 2 was not used in these experiments). The H+ and H_2+ peaks were separated by ≈1μs while their widths (FWHM) were only 50ns. The ions were detected with a Daly type scintillation ion detector[21] using an acceleration voltage of 30kV and an RCA C31000M photomultiplier tube.

With a high H_2 product velocity (≈1x10^{6}cm/s) in the dissociation of CHDN there was a concern that some H_2 might escape detection. It was imperative that all the H_2^* be collected in order to have accurate quantum state distributions and Doppler profiles. The collection efficiency of the apparatus was tested by measuring H_2 product from the dissociation of formaldehyde. The velocity of H_2 formed in the v"=1 state from H_2CO resonantly dissociated on the $2^14^1\,{}^pP_1(1)0$ at 29484.6cm^{-1} has a narrow velocity distribution with an average velocity of ≈1.5x10^{6}cm/s. Doppler profiles corresponding to that velocity with an isotropic angular distribution were obtained in accord with those measured by Butenhoff et. al.[22] using LIF detection. This assured that when

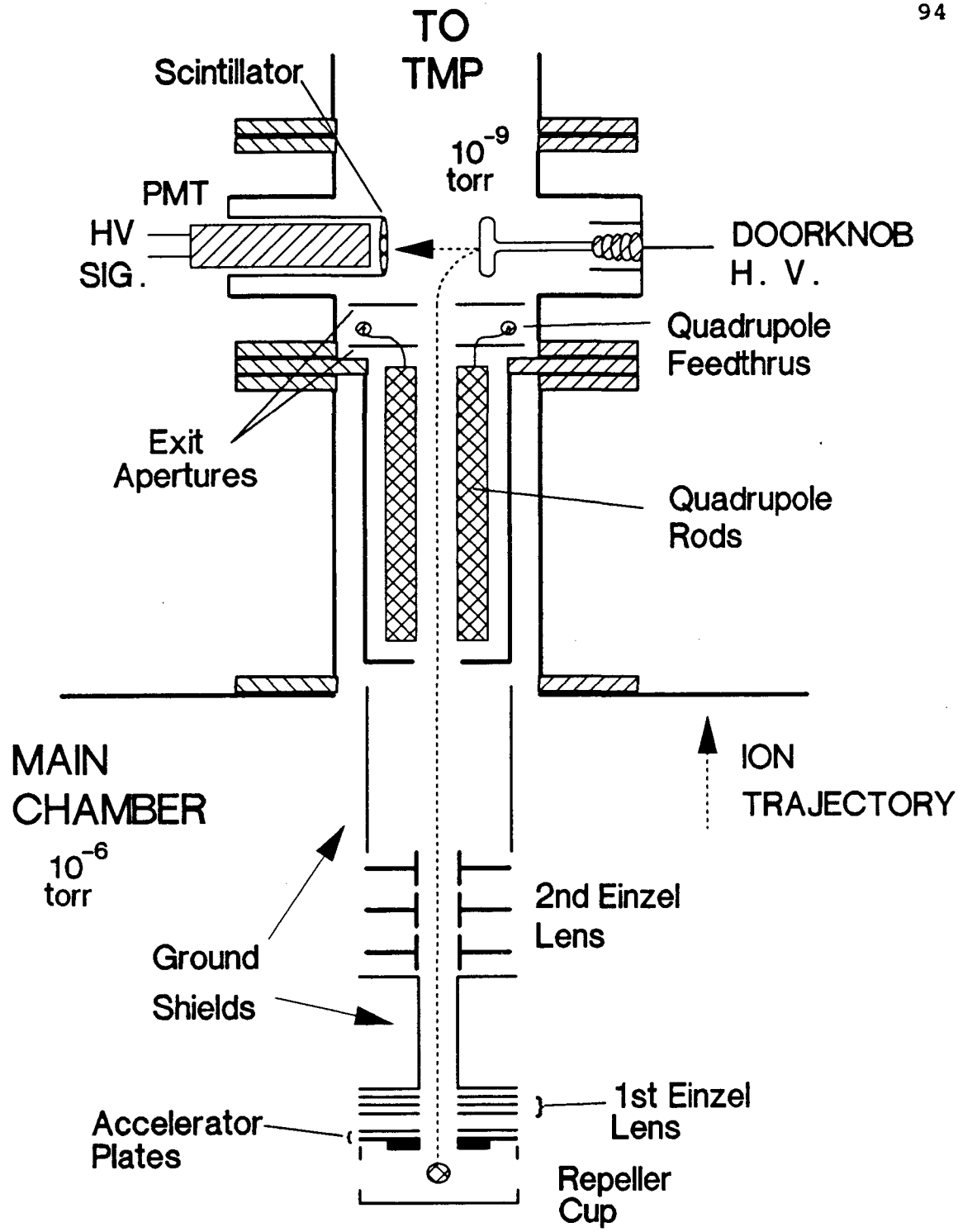

Figure 2. Cross section of the ion detection apparatus used in the experiments reported in this thesis. All ion optics are cylindrically symmetric. The drawing is roughly to scale.

dissociating CHDN the H_2 product, which has a velocity $<1.3x10^6$cm/s, could be collected uniformly without bias towards the slower molecules.

Beams of both the 1,3 CHDN and the 1,4 CHDN were produced neat from a reservoir kept at 0°C giving vapor pressures of approximately 30 torr and 20 torr respectively. 1,3 CHDN was obtained from Aldrich and 1,4 CHDN was obtained from Fluka and were degassed before use. No further purification was performed. CHDN dimers were not observed in the beam, as was expected due to the soft expansion conditions, and no attempt was made to investigate their impact on the experiment.

The probe laser system began with pulse amplification of the output from a Coherent 699-29 ring dye laser. The amplification was done with 450mJ of 532nm light from a Quantel 581C Nd:YAG laser. The amplifier chain, built in our laboratory, utilized 3 prism dye cells. The output power of the visible light was >100mJ with a bandwidth of ≈95MHz at the peak of the amplifier dyes used (R6G and Kiton Red). The visible light was frequency doubled using a INRAD Autotracker II doubling crystal unit with a 3cm long KD^*P crystal which typically gave around 30% conversion. The uv light was then converted to xuv-vuv radiation via straight tripling[20] or sum frequency mixing (2uv+1vis)[23] in a pulsed molecular beam. The use of the pulsed molecular beam allowed for the elimination of windows between the mixing

chamber and the interaction region while maintaining a good vuv-xuv conversion efficiency. The vuv-xuv radiation was reflected off a grating in a 1m VUV monochromator into the main chamber. The grating served to recollimate the beam and to allow separation of the uv radiation from the vuv when desired. The size of the probe laser beam at the interaction region was adjustable from a tight focus (<100μm) to 3mm by translating the grating inside the monochromator. During scans the grating was set at zeroth order so that the intense residual uv light could be used as the ionization beam in the 1+1 REMPI scheme.

The 699-29 was operated with Rhodamine 6G (R6G) while the amplifier chain was operated with primarily either R6G or Kiton Red covering the regions 565nm to 573nm and 589nm to 595nm respectively. With these dyes we were able to utilize the Xenon 2+2+1 (5ω) mixing resonances from 85,000cm^{-1} to 87,000cm^{-1} and 88,000cm^{-1} to 90,000cm^{-1}.[23] In this configuration a 3mm LiF window was inserted into the beam path in order to filter out any 6ω light generated by tripling of the uv radiation. The intensity of the 6ω radiation was measured to be <1% of that of the 5ω light after the LiF window. Straight tripling (6ω) was done in Argon giving coverage of the regions from 101,000cm^{-1} to 103,000cm^{-1} and 104,000cm^{-1} to 106,000cm^{-1} for Kiton Red and R6G respectively.[17]

For the majority of the experiment the CHDN molecules were photodissociated with photons generated around 212nm. The dissociation light source was comprised of a second single-mode pulsed dye laser system operated at ≈636nm (using DCM in both the 699-29 and amplifier chain) from which the 3rd harmonic was generated by frequency doubling in a KDP crystal and then mixing the generated uv radiation with the residual visible light in a BBO crystal. The pulse energy from this system was ≈6mJ. For 1,4-CHDN this excited a symmetry forbidden $\pi \rightarrow \pi^*$ transition[24,25] while for 1,3-CHDN a symmetry allowed $\pi \rightarrow \pi^*$ transition was excited.[26,27] The dissociation laser had a beam diameter of 6mm and was sent, unfocused, through a secondary port into the main chamber where it crossed with the molecular beam and the probe beam. Although having a focused photolysis laser beam yielded more signal, the configuration used in the experiment, with a unfocused laser, kept the dissociation area large compared to the probe area which was important in eliminating any artifacts due to beam overlap. A side view of the interaction region is shown in Figure 3.

Additional experiments to measure the kinetic rate constants and to repeat the (v,J) correlation measurements utilized a Lambda-Physik EMG-103-MSC excimer laser operated with an ArF gas mixture with an output of ≈100mJ at 193nm. An unstable resonator was used in the laser cavity to produce a well collimated beam with a uniform intensity

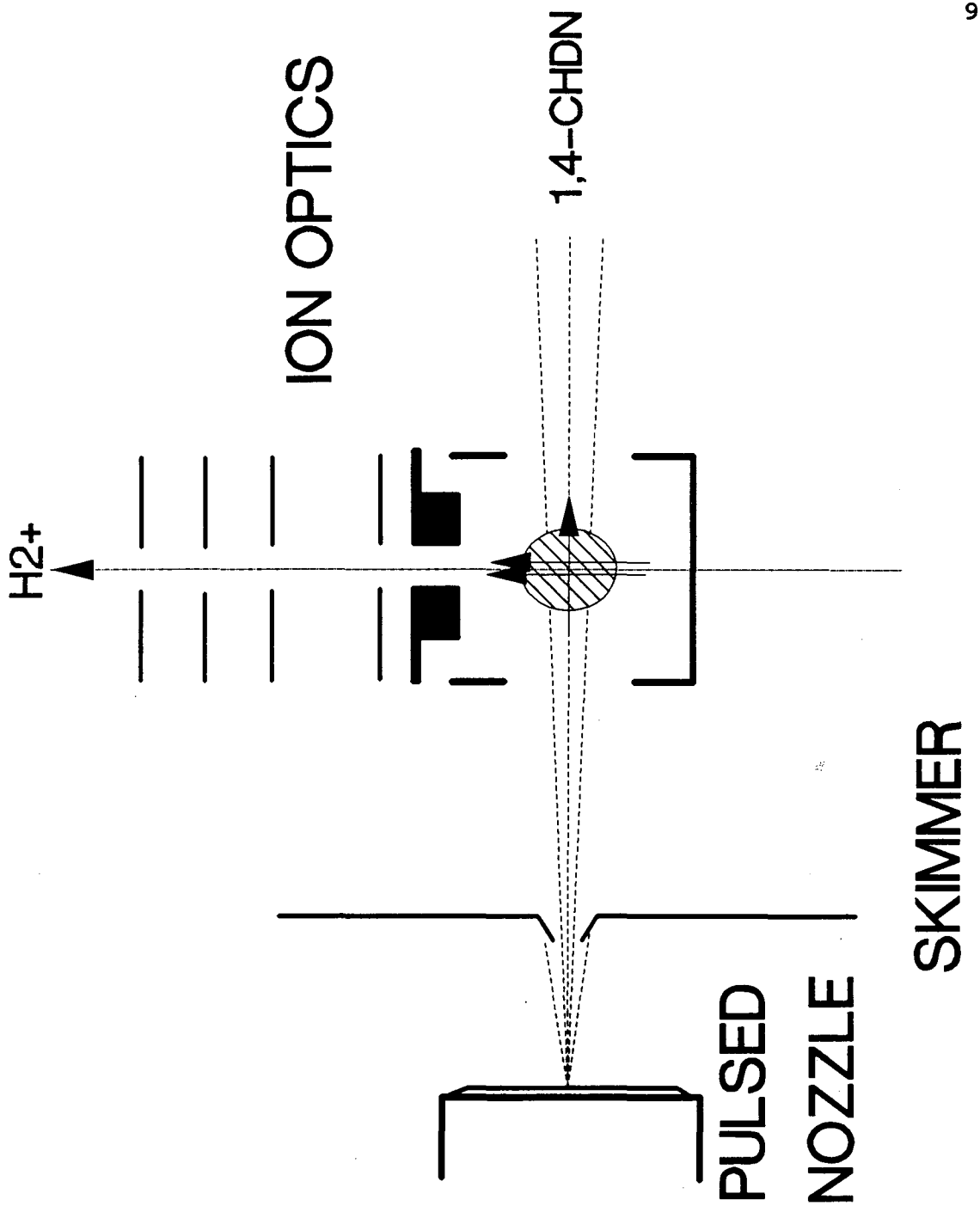

Figure 3. Side view of the interaction region. The arrows indicate the polarizations of the various laser beams which propagate perpendicular to the page. The photolysis (212nm) and ionizing (uv) beams are polarized vertically while the vuv polarization can be vertical or horizontal depending on the four-wave mixing scheme used.

cross section. An 8mm diameter section of the beam, containing ≈10mJ of energy, was injected into the interaction region. For the kinetic rate constants study this beam was unfocused while for the (v,J) correlation measurements the beam was softly focused to ≈2mm diameter. The pulse-to-pulse timing jitter was <±1.5ns for the 20ns FWHM beam. A full description of the set-up utilizing this photolysis laser will be given in Chapter IV and elsewhere.[28]

The use of a narrow bandwidth tunable photolysis laser allowed a study of the effect on the H_2 elimination process of the frequency of the photon absorbed by the CHDN molecule. Resonances in the 1,4-CHDN excited electronic state (π^*) were looked for briefly by tuning the dissociation laser over a narrow region of $10cm^{-1}$ and monitoring the H_2 signal intensity from a given ro-vibrational level. The pump laser bandwidth was sufficiently narrow ($<0.01cm^{-1}$) to resolve any rotational structure that might be present. No excited state resonances were observed. This is not surprising in view of the expected short lifetime of the 1,4-CHDN excited electronic state.[1,9]

Time delay scans between the pump and probe lasers were performed for beam diagnostics and kinetic rate constant measurements. The timing of the whole system was controlled with two SRS 535 Delay/Pulse generators. When utilizing the

two single-mode systems the jitter between the two laser pulses was <±1ns. For experiments using the excimer laser as the photolysis source the jitter was somewhat greater (<±2ns). Delay scans were generated and data was taken by a PC interfaced to the pulse/delay generators. The photolysis/probe delay for the population scans was set at the maximum H_2^+ signal as determined by the delay scans. Time delay scans were done for both the 1,4-CHDN and 1,3-CHDN with significant differences between the two isomers observed. The data presented here was taken using the excimer laser as the photolysis source. With laser pulses of 8ns and 20ns for the probe and photolysis lasers respectively the maximum resolution was ≈2ns for these scans.

To determine the rotational and vibrational state distributions of the H_2 product the H_2 was ionized by (1+1) REMPI using either the B $^1\Sigma_u$ or C $^1\Pi_u$ states of H_2. The vibrational coverage was from v"=0 to v"=6 although for the v"=6 scans the signal was barely detectable. The rotational coverage varied for each vibrational level depending on the relative populations and transition strengths but typically was from J"=0 to J"=9. For higher J" levels only the odd states were observable due to the hydrogen nuclear spin statistics.

Normalization of the vuv laser intensity dependent H_2^+ signal was accomplished in two different manners. For

wavelengths above the LiF cutoff a solarblind PMT (EMR 542G) was placed in the monochromator to monitor the intensity of the first order vuv diffraction. The tube has a 10^4 discrimination against uv light and a reasonably flat vuv response in the region where it was being used. Operating voltages were typically between 1.6 and 1.8kV. For wavelengths below the LiF cutoff acetylene was seeded into the CHDN beam to produce an additional ion signal that was dependent on the xuv signal. The $C_2H_2^+$ signal was then used to normalize the H_2^+ signal. C_2H_2 has a flat photoionization response in this region and has been successfully used before for xuv normalization.[29] The accompanying uv laser has sufficient intensity to ionize all H_2 molecules excited by the vuv laser. The dissociation laser power was stable enough that shot-to-shot normalization to that signal was not necessary although the pulse energy was monitored prior to each scan.

While dissociating 1,3-CHDN and scanning the H_2 v"=0 product (when straight tripling was required) there was a large background ion signal at m/e=26 ($C_2H_2^+$). This made shot-to-shot normalization with acetylene impossible. In this case the relative xuv intensity was measured by adjusting the monochromator to pass 1st order light through the interaction region and onto an electron multiplier tube (EMT) which measured the beam intensity. The grating was then turned to 0th order for scanning the H_2 transition.

The xuv signal was measured before and after each scan and that signal was used to normalize between different scans.

III. RESULTS AND ANALYSIS

A. POPULATION DISTRIBUTION

The different transitions used to generate the quantum state distribution of the H_2 molecule eliminated from CHDN are listed in Table I. The vibrational distribution obtained from this data is shown in Figure 4 while the rotational distributions are shown in Figure 5. Included with each of the distributions are non-linear least-square fits of the data with an appropriate statistical distribution function. These will be discussed in more detail below.

The relative population, P(v,J), for a given ro-vibrational state was calculated according to:

$$P(v,J) \propto \frac{I(v,J)*C*g}{\mu_{if}*E_p}$$

where I(v,J)=normalized integrated line intensity, C=instrument function (boxcar sensitivity, analog processor gain, etc.), g=H_2 nuclear spin statistic degeneracy factor, μ_{if}=line transition strength (including the Franck-Condon and the Höln-London factors), and E_p=photolysis laser (212nm) intensity. The 1,4-CHDN and 1,3-CHDN data were not normalized to each other due to the differences in the beam

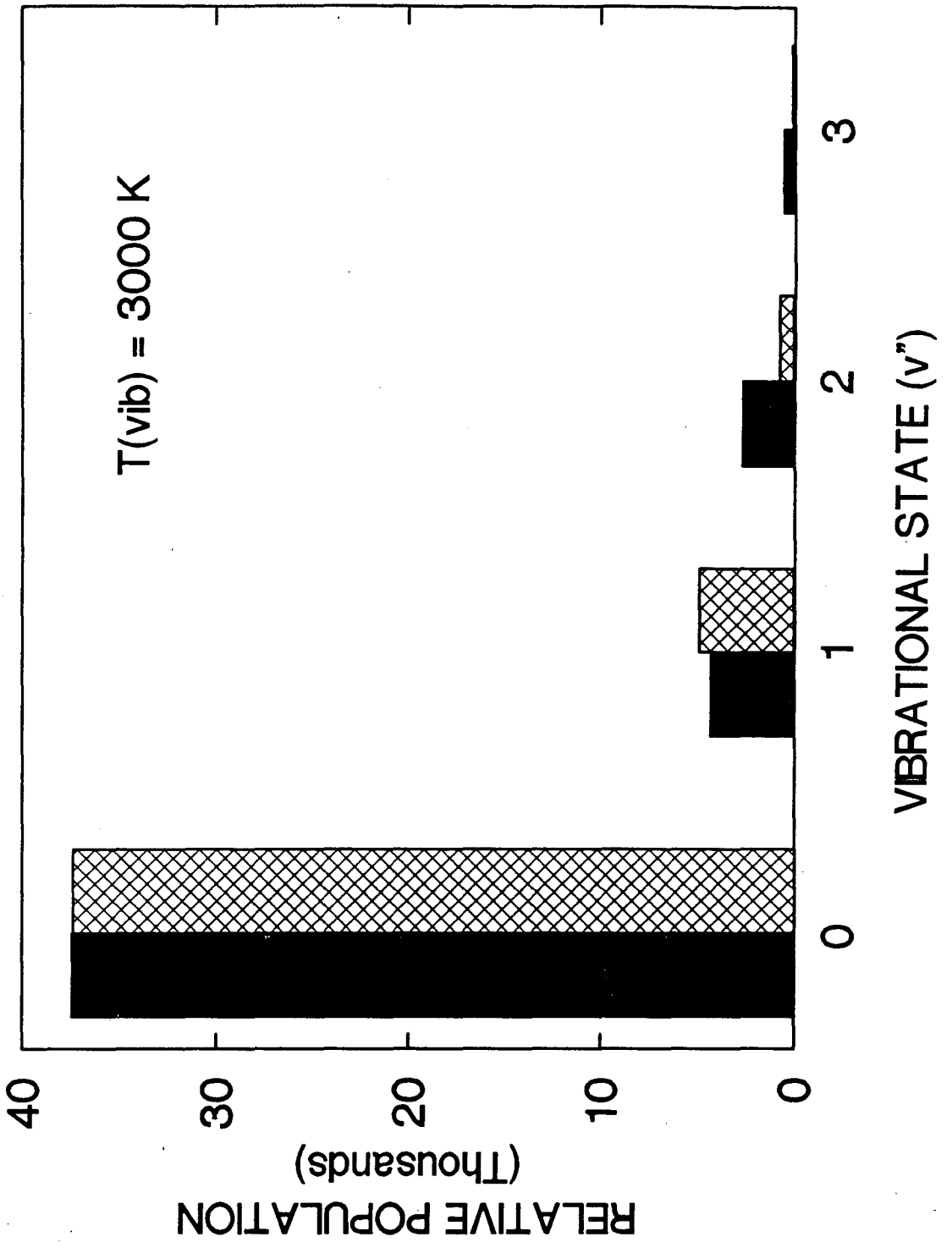

Figure 4. Vibrational state distribution of H_2 product from the photodissociation of 1,4-CHDN at 212nm. The solid bars are the experimental data points while the hatched bars are the statistical fit.

Figure 5. Rotational state distributions of H_2 product from the photodissociation of 1,4-CHDN at 212nm for the vibrational levels v"=0 through v"=3. The solid bars are the experimental data points while the hatched bars are the statistical fits.

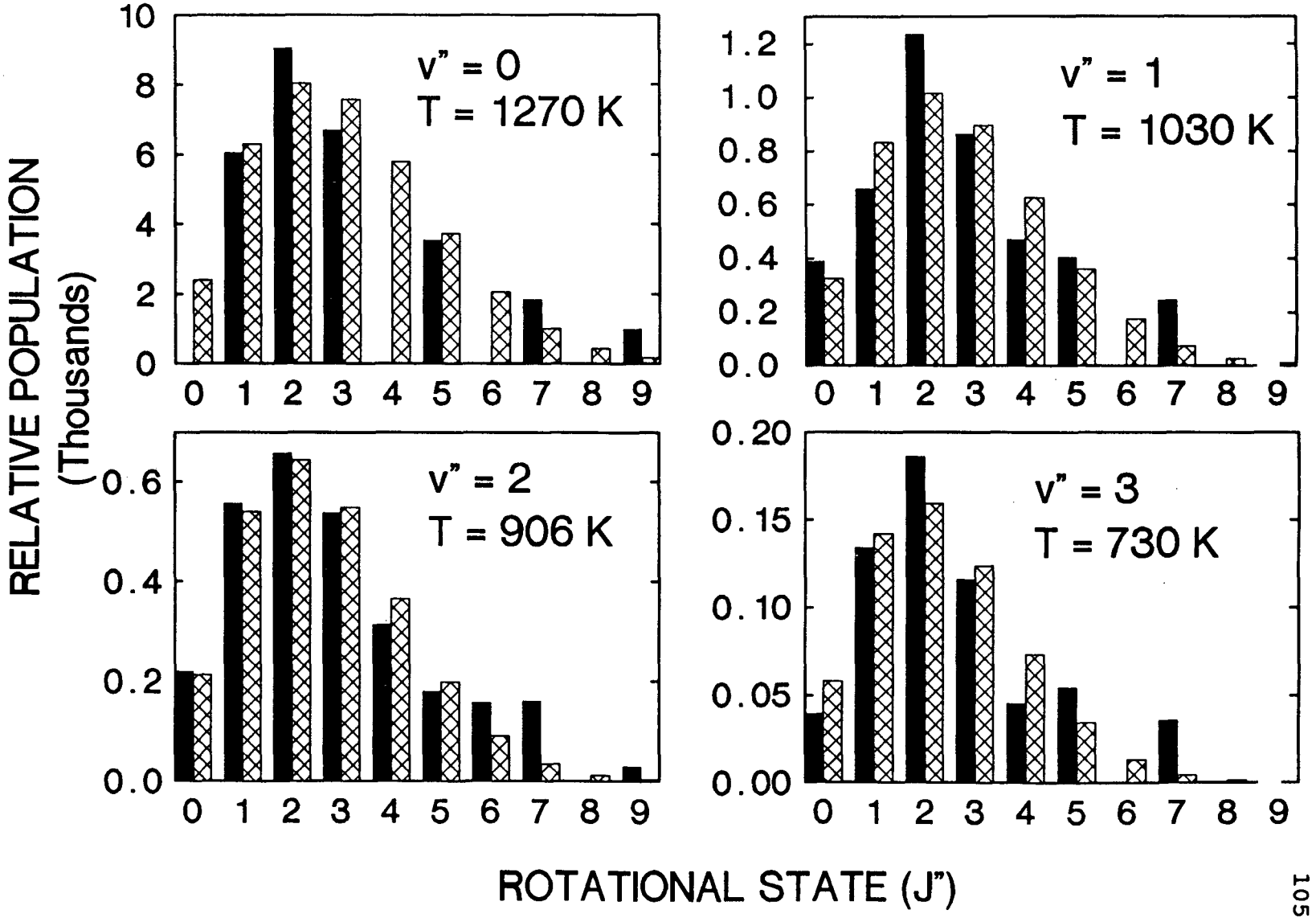
RELATIVE POPULATION
(Thousands)
v" = 0
T = 1270 K
v" = 1
T = 1030 K
v" = 2
T = 906 K
v" = 3
T = 730 K
ROTATIONAL STATE (J")

Figure 5

densities and the absorption cross sections at 212nm of the isomers. The intensity of each scan I(v,J) was measured by numerically integrating the area under each curve after appropriate axis scaling and baseline subtraction. The scans were normalized to the vuv intensity as described in the previous section.

Table I: H_2 TRANSITIONS USED FOR POPULATION DISTRIBUTION

Initial Vib. State	Electronic Transition	Initial Rot. States	Trans. Freq. Range
v"=0	C-X (1,0)	J"=0 TO 5	100,500 to 102,600 cm^{-1}
	C-X (2,0)	J"=5 TO 9	
	C-X (3,0)	J"=9	
v"=1	B-X (1,1)	J"=0 TO 2	87,200 to 88,500 cm^{-1}
	B-X (2,1)	J"=3 TO 5	
	B-X (3,1)	J"=5 TO 7	
	B-X (4,1)	J"=9	
v"=2	B-X (2,2)	J"=0 TO 4	83,750 to 85,500 cm^{-1}
	B-X (3,2)	J"=5 TO 7	
	B-X (4,2)	J"=9	
v"=3	B-X (5,3)	J"=0 TO 5	83,750 to 85,500 cm^{-1}
	B-X (6,3)	J"=4 TO 7	
	C-X (0,3)	J"=1 TO 3	87,200 to 88,500 cm^{-1}
	C-X (1,3)	J"=7 TO 9	
v"=4	B-X (8,4)	J"=0 TO 3	83,750 to 85,500 cm^{-1}

In some cases there was overlap between transition profiles due to the large Doppler widths of those transitions. When this happened it was often possible to deconvolute the profiles by fitting one or the other to a lineshape from a transition of similar quantum numbers and rotational branch. While this technique was useful in estimating line intensities it was not used to infer lineshapes. Another difficulty arose when trying to probe high lying vibrational states in the $B^1\Sigma_g$ manifold. The $B^1\Sigma_g$ state correlates to the ion pair H^+ and H^- and as a result of this (1+1) REMPI often causes dissociative ionization, producing both H^+ and H_2^+. For REMPI through the $B^1\Sigma_g$, v'=5 or 6, state typically from 10% to 30% of the signal is in the H^+ channel. REMPI through higher vibrational states can produce >80% H^+. While under the conditions of this experiment there is essentially zero background at m/e=2, there is a considerable m/e=1 signal due to the tight focusing of the uv required to saturate the ionizing step in the REMPI process. The m/e=1 signal can be reduced to tolerable levels by relaxing the probe focus but then one has to account for the non-saturated second REMPI step. A consequence of this was that in order to take the v"=0 data it was necessary to ionize through the $C^1\Pi_u$ state (which is non-dissociative). For v"=3 the H^+ component was estimated from measured H^+/H_2^+ ratios. For v"=4 the rotational populations were taken under non-saturating conditions

although the H_2^+ signal for the J"=1 transition was measured under saturating conditions. The v"=5 and 6 signals (which were ionized through v'>8 of the B state and were nearly all H^+) were observed with a loosely focused probe beam.

The normalization worked very well for reducing the uncertainty caused by fluctuations in the vuv-xuv power. These fluctuations, which could be greater than 50% of the average vuv intensity, were by far the largest source of uncertainty in the experiment. With proper shot-to-shot normalization very good signal to noise ratios (>10:1) were obtained on scans which were not limited by ion counting statistics. However, the ability to reproduce relative integrated intensities of different transitions was somewhat disappointing. Some individual transitions were scanned a number of times in order to get meaningful statistics. From these measurements the accuracy of the quantum state populations is estimated to be ±20%. While the uncertainty in the measurements is relatively large the trends in the populations can be clearly seen.

The vibrational distribution, while peaked at v"=0, shows a fair amount of vibrational excitation the distribution of which can be statistically fitted with a vibrational temperature of ≈3000K. The functional form used to fit the distribution is:

$$P(v) = P_0 * e^{-(v+1/2)\frac{\omega_e}{kT} + (v+1/2)^2\frac{\omega_e x_e}{kT} - (v+1/2)^3\frac{\omega_e y_e}{kT}}$$

The anharmonicity constants were taken from Herzberg.[30] The rotational populations peak around J=2 or J=3 with the rotational temperatures varying from ≈1270K to ≈730K. For the rotational distributions the following statistical function was used in the fitting:

$$P(v,J) = P_0 * (2J+1) * e^{-J(J+1)\frac{B(v)}{kT} + J^2(J+1)^2\frac{D(v)}{kT} - J^3(J+1)^3\frac{H(v)}{kT}}$$

Here the vibrationally dependent anharmonicity constants were taken from Dabrowski.[12] The vibrational level populations were calculated from the fits to the rotational levels. The measured temperatures along with their standard deviations are given below in Table II. The rotational excitation of the H_2 fragment is less favorable then vibrational excitation and the amount of rotational energy imparted into the H_2 fragment is relatively decoupled from its final vibrational state.

TABLE II: H_2 INTERNAL ENERGY DISTRIBUTION TEMPERATURES

Vibrational Temperature		
T(vib)	3000 +/- 430 K	
Rotational Temperatures		
v"	T(rot)	Std. Dev.
0	1270K	170
1	1030K	160
2	910K	80
3	730K	120

There are a number of important observations that can be made from the rotational and vibrational quantum state distributions of the H_2 product from the unimolecular dissociation of 1,4-CHDN. In the ground state of 1,4 CHDN the 3 and 6 hydrogen atoms are calculated to be 3.0Å apart.[11] In molecular hydrogen the H-H distance is well known to be 0.75Å in its ground state. The H-H distance is expected to be longer than this value in the critical structure near the transition state. The H atoms must be very close to each other before there is sufficient electronic orbital overlap for a H-H bond to form and two C-H bonds to break simultaneously as is required by the concerted nature of the process. There are two ways to account for this. Either the CHDN ring must be in a severely distorted boat formation at the transition state or the 3 and 6 C-H bond lengths must increase, due to a weakening of the bond by partial relocation of electron density from between the C and H atoms to the π-orbital system of the carbon ring, in order to get the H's close enough for the reaction to take place. Calculations of the ring strain energy needed for the first process show that it is significantly higher than the measured activation energy of 43kcal/mole for the reaction. Thus it seems obvious that, in addition to the strained boat form, elongation of the C-H bonds is necessary to reach the critical structure. That is not surprising, especially when one considers the

stabilizing effect from formation of the benzene ring. This is supported by recent calculations of the transition state configuration of 1,4-CHDN which show elongated C-H bond lengths and a H-H distance of ≈1Å.[15,16]

In a sense, the experimental probing of the vibrational and translational energies of H_2 products should reveal the average H-H and C-H distances in the critical structure near the transition state. Vibrational relaxation of H_2 during the repulsive separation of products is expected to be inefficient and the H_2 vibrational energy will depend on the average H-H distance at the transition state. In a concerted decomposition, when bonding electrons between C-H bonds rearrange into the benzene ring and H_2 molecules, C-H interaction between H_2 and nascent benzene will be repulsive and the repulsive energy will depend on the C-H distances in the transition state region.

Since the beam of cyclohexadiene in this experiment is produced by supersonic expansion, the rotational temperature is expected to be very cold. The rotational energy of H_2 which is associated to the original rotational motion of CHDN should be negligible and if the transition state structure for H_2 elimination is symmetric, the synchronous concerted decomposition will not exert any torque on the departing H_2 molecules. It is not surprising that the various rotational distributions observed are peaked at relatively low J given the high total amount of energy

available in the system.

The angular momentum of H_2 is undoubtedly created during the repulsive release of the potential energy. To understand this one must first consider how rotational energy would be imparted into the H_2 fragment. Vibrational energy would come from different H-H separations at the transition state but rotational energy would have to come from either a twisting of the two C-H bonds away from the symmetry plane which contains the 3 and 6 carbon atoms in the ring or a non-symmetric boat formation (i.e. one side flipped up more than the other). The first would send the H_2 off like a helicopter with its imparted velocity and rotational angular momentum vectors parallel while the later would induce a Frisbee like motion where the two vectors are perpendicular. Given the low amount of rotational energy in the fragment the distortion from the symmetric transition state, especially the twisting of the H_2 with respect to the two C atoms along the C-H-H-C coordinate, should not be extensive. The second observed trend, that the amount of rotation is decoupled from the amount of vibration, also supports this view since even in the vibrational ground state where there is much more available energy for rotation little such excitation occurs. Thus, while the bending of the ring occurs quite readily it appears that even though the energy of excitation is far above that required to reach the transition state, the molecules dissociate from a very

symmetric transition state structure with little distortion involved.

Part of the impetus for looking at both isomers of CHDN was to see if there was a rapid isomerization of the two isomers in the excited state before molecular dissociation. If elimination of H_2 took place from both isomers then one might expect to see a bimodal H_2 vibrational distribution. On the other hand, if 1,3-CHDN isomerized to 1,4-CHDN before eliminating H_2 then one would expect a single vibrational distribution with the 1,3-CHDN mimicking that of the 1,4-CHDN. Within the experimental error the quantum state distributions from the two isomers are identical. This, combined with the fact that the translational energies are identical and the rate of dissociation of 1,3-CHDN, as measured from the time dependence of the accumulation of H_2 products, is slower supports the later process where 1,3-CHDN isomerizes to 1,4-CHDN before eliminating H_2.

B. TRANSLATIONAL ENERGY

As discussed previously, the translational energy of the product H_2 molecule was determined through the Doppler profiles of the transitions measured. The individual lineshapes were fit using a non-linear least squares method with the function:

$$I \propto \frac{1}{v_D} * [1+\beta * P_2(\cos\theta) * P_2(\chi)] \quad (4)$$

where v_D=maximum doppler shift, β=effective anisotropy parameter, P2=second order Legendre polynomial, θ=angle between the electric field vector of the linearly polarized photolysis laser and the direction of the probe laser and χ=Doppler shift/v_D. This function was convoluted with a normalized Gaussian H_2 velocity distribution of a variable width. The H_2 translational energy was then calculated from the Doppler shift observed and the transition frequency. A listing of the H_2 translational energies and velocities measured is given in Table III. The velocities for a number of quantum states were not able to be measured due to interference in the Doppler profiles from other close lying transitions.

TABLE III: H_2 TRANSLATIONAL ENERGY FROM 1,4-CHDN			
VIB. STATE	ROT. STATE	VELOCITY(CM/S)	E_{Tr}(kcal/mole)
v"=0	J"=3	$1.25x10^6$	37
	J"=7	$1.2x10^6$	34
v"=1	J"=1	$1.0x10^6$	24
	J"=3	$9.95x10^5$	24
	J"=5	$1.0x10^6$	24
v"=2	J"=0	$9.3x10^5$	21
	J"=1	$9.7x10^5$	22.5
	J"=5	$9.9x10^5$	23.4
	J"=7	$1.0x10^6$	24
v"=3	J"=1	$9.5x10^5$	22
	J"=3	$9.4x10^5$	21
	J"=9	$1.0x10^6$	24

A measurement of the translational energy distribution of H_2 product was done previously via photofragmentation translational spectroscopy[1] and it was found that the H_2 translational energy peaked at 25 Kcal/mol. In this study the CHDN molecule was dissociated in two manners: with 193nm photons and through an infra-red multi-photon process. The H_2 translational energy distribution from these two methods peaked at the same energy. The only difference was in the widths of the distributions. This indicated that the kinetic energy imparted into the H_2 fragment was dependent mainly on potential energy barrier in the exit channel and not on the total amount of energy available.

If the repulsive energy release dominates the separation of products unless there is an extremely strong dependence of the repulsive potential energy on the H-H vibrational coordinate one would expect that the H_2 translational energy should not depend strongly on the final rotational or vibrational state of the molecule provided that the transition state has a symmetric structure and the decomposition is synchronous and concerted. Our results show that the H_2 kinetic energy only decreases slightly as its internal energy increases. The lineshapes for the J"=1 states from v"=1 to v"=3 are shown in Figure 6 with their respective fits and measured widths. As one can see, the translational energy decreases from ≈34kcal/mole for v"=0 to ≈22kcal/mole for v"=3 while at the same time the H_2 internal energy has increased by >30kcal/mole. Similar behavior was observed for the v"=4, v" 5, and v"=6 transitions although the uncertainty is much greater in these measurements. The widths of the H_2 velocity distributions also increase as one goes to higher internal energy. This would explain the difference between the P(E) curves seen by Zhao et. al in their experiments using IRMPD and 193nm excitation. The 193nm dissociation, with a much higher average excitation energy per molecule, is expected to produce more vibrationally excited H_2 with wider velocity distributions then the IRMPD experiment. Thus the former process produced a wider P(E) curve but the maximum translational energy

Figure 6. Variation of the translational energy with vibrational level of H_2 product from the photodissociation of 1,4-CHDN at 212nm. Bottom Trace (■): H_2 B←X (1,1) R(1) transition (v_D=2.70cm^{-1}, $\upsilon(0)$=87,358.60cm^{-1}, E_{tr}=20.6kcal/mole). Middle Trace (+): H_2 B←X (2,2) R(1) transition (v_D=2.63cm^{-1}, $\upsilon(0)$=84,714.92cm^{-1}, E_{tr}=20.7kcal/mole). Top Trace (◇): H_2 B←X (5,3) R(1) transition (v_D=2.51cm^{-1}, $\upsilon(0)$=84,652.91cm^{-1}, E_{tr}=18.9kcal/mole). The theoretical fits were calculated using a non-linear least squares fit to the function $1/v_D(1+\beta P_2(\cos\theta)P_2(\chi))$ (where v_D=Doppler shift) given in Ref. 33.

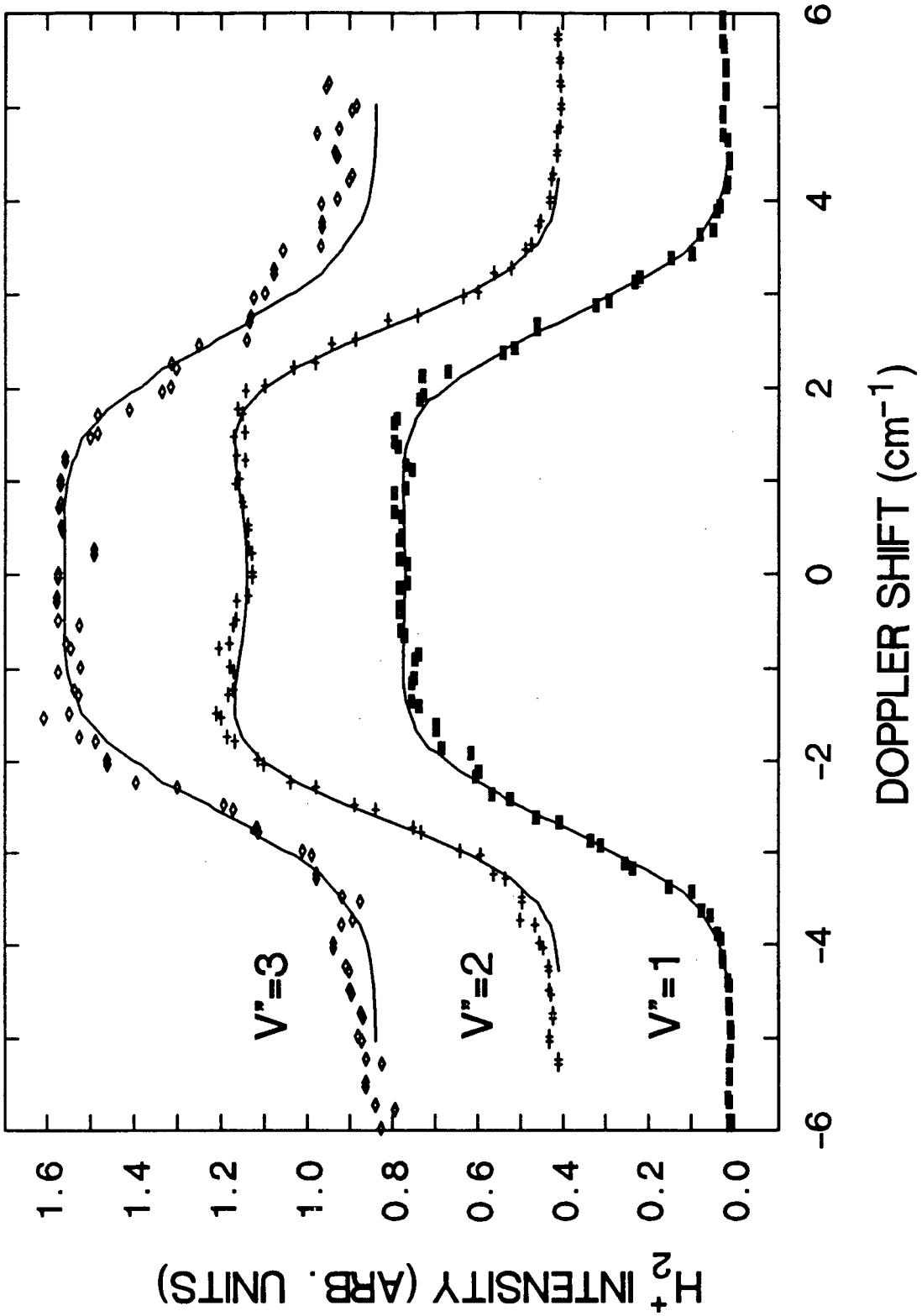
V"=3
V"=2
V"=1
1.6
1.4
1.2
1.0
0.8
0.6
0.4
0.2
0.0
H_2^+ INTENSITY (ARB. UNITS)
-6
-4
-2
0
2
4
6
DOPPLER SHIFT (cm^{-1})

Figure 6

remained fairly constant for both experiments.

There are two important things to consider in explaining the translational energy distribution in the H_2 fragment. The first is the concerted nature of the reaction. As explained previously,[1] in a concerted process there is a large repulsion between the product molecules immediately after the reaction has occurred when they are closely placed in the region of the transition state. This potential energy is mainly channeled into translational energy of the H_2 product. A second reason is the presence of a large number of degrees of freedom in the parent molecule. Depending on how many active modes there are in the CHDN and in despite of the deposition of 134kcal/mole of energy there will only be 3-5 kcal/mole of energy in any given ro-vibrational degree of freedom. Thus translational energy imparted to the H_2 from energy coupled to the reaction coordinate by an excited parent molecule will be a relatively small fraction of the total translational energy of the fragment. Of course, the repulsion between H_2 and benzene formed near the transition state is expected to depend slightly on the H-H distance, or the vibrational excitation of H_2.

C. REACTION KINETICS

Photolysis/probe laser delay scans for both the 1,3-CHDN and 1,4-CHDN are shown in Figure 8. The H_2^+ signal from the 1,4-CHDN photofragmentation peaks at 20ns while the corresponding signal for the 1,3-CHDN case peaks at 80ns. This difference is independent of the vibrational or rotational state being probed within the experimental resolution. Diffusion effects were minimized by having the photolysis beam diameter much greater than that of the probe beam. To get the best possible representation of the H_2 evolution the delay scans were taken under identical alignment conditions.

The relative heats of formations of 1,3-CHDN, 1,4-CHDN, and Benzene+H_2 are shown in Figure 7. The two CHDN isomers are nearly equal in energy with the heat of formation of 1,3-CHDN being ≈3 Kcal/mol lower. According to the Woodward-Hoffman selection rules the direct H_2 elimination from 1,3-CHDN is forbidden in its ground electronic state while from 1,4-CHDN it is allowed.[31,32] With this in mind the following kinetic model was used to explain the differences between the decomposition of the two isomers.

$$\begin{array}{ccccccc} & & \overset{k_1}{\rightleftharpoons} & & \overset{k_2}{\rightarrow} & & \\ 1,3\text{-}CHDN & & & 1,4\text{-}CHDN & & BENZENE+H_2 \rightarrow DIFFUSION & \\ \downarrow k_4 & & \underset{k_{-1}}{} & \downarrow k_3 & & & \\ RING & & & H\ ATOM & & & \\ OPENING & & & ELIMINATION & & & \end{array} \qquad (5)$$

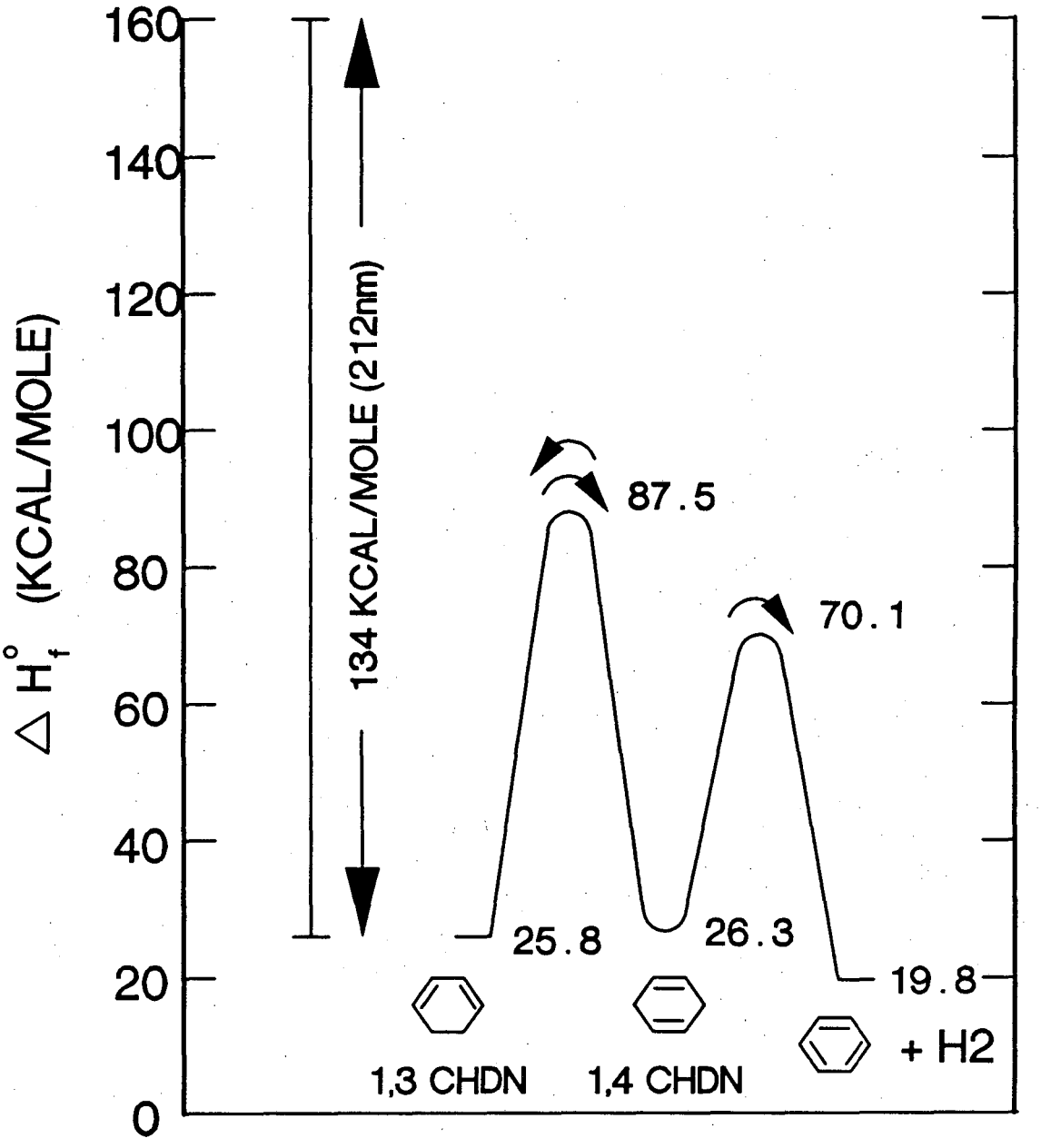

Figure 7. Potential energy diagram for the isomerization and H_2 elimination reactions of 1,4-CHDN.

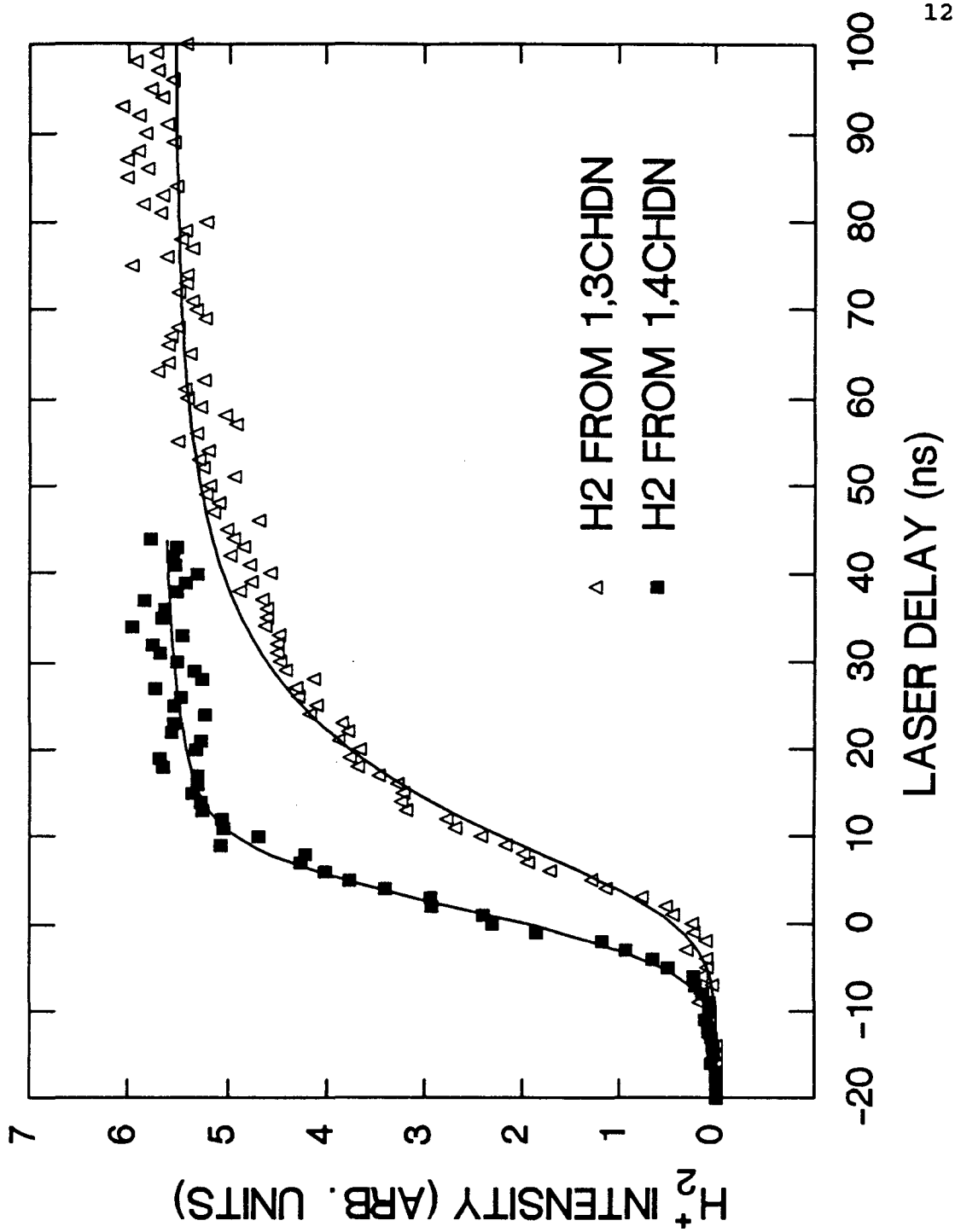

Figure 8. Appearance of H_2 product from the photodissociation of 1,4-CHDN an 1,3-CHDN as a function of the delay between the photolysis and probe lasers. The rate constants obtained are: $k_1=0.06ns^{-1}$, $k_2=0.5ns^{-1}$, $k_3=0.001ns^{-1}$, $k_4=0.06ns^{-1}$.

If one neglects the diffusion process initially the appearance of H_2 as a function of time obeys the following set of rate equations:

$$\frac{dX}{dt} = k_1*Y - k_{-1}*X - k_2*X - k_3*X \tag{6}$$

$$\frac{dY}{dt} = k_{-1}*X - k_1*Y - k_4*y \tag{7}$$

$$\frac{dZ}{dt} = k_2*X \tag{8}$$

where X=[1,4-CHDN], Y=[1,3-CHDN] and Z=[H_2]. From (6) and (7) the following differential equation for X can be derived:

$$\frac{d^2X}{dt^2} + (k_1+k_{-1}+k_2+k_3+k_4)*\frac{dX}{dt} + [k_1*k_{-1}-(k_1+k_4)*(k_{-1}+k_2+k_3)]*X = 0 \tag{9}$$

This can be simplified further by letting $k_1 \approx k_{-1}$ since the energy difference between 1,4-CHDN and 1,3-CHDN is only 3kcal/mole in their ground electronic states and the barrier height to isomerization is >60kcal/mole, much smaller than the excitation energy which is as high as 148kcal/mole.

If one lets $X = e^{\lambda t}$ and then substitutes into (9) and solves for λ one finds that:

$$\lambda_{1,2} = 1/2*\{-(2*k_1+k_2+k_3+k_4) \pm [4*k_1^2+k_2^2+2*k_2(k_3-k_4)+(k_3-k_4)^2]^{1/2}\} \tag{10}$$

Thus:

$$X = C_1 * e^{\lambda_1 * t} + C_2 * e^{\lambda_2 * t} \qquad (11)$$

where C_1 and C_2 are determined by initial conditions. Solving (8) one obtains the following equation for the appearance of H_2 as a function of time:

$$K_{H_2}(t) = \alpha * e^{\lambda_1 * t} + \beta * e^{\lambda_2 * t} - (\alpha + \beta) \qquad (12)$$

with,

$$\alpha = k_2 * \frac{C_1}{\lambda_1}$$
$$\beta = k_2 * \frac{C_2}{\lambda_2} \qquad (13)$$

For the dissociation of 1,4-CHDN the initial conditions are that $X(t=0) = D_0 = C_1 + C_2$ where D_0 is a constant and $Y(t=0) = 0$. Substitution into (6) yields:

$$\frac{dX}{dt}\Big|_{t=0} = -(k_1 + k_2 + k_3) * D_0 = C_1 * \lambda_1 + C_2 * \lambda_2 \qquad (14)$$

The solution of (14) gives the following values of α and β for the dissociation of 1,4-CHDN:

$$\alpha = D_0 * k_2 * \frac{[-\lambda_2 - (k_1 + k_2 + k_3)]}{\lambda_1 * (\lambda_1 - \lambda_2)} \qquad (15)$$

$$\beta = D_0 * k_2 * \frac{[\lambda_1 + (k_1+k_2+k_3)]}{\lambda_2 * (\lambda_1 - \lambda_2)}$$

For the dissociation of 1,3-CHDN the initial conditions are switched so that X(t=0) = 0 and Y(t=0) = D_0. Therefore:

$C_1 + C_2 = 0$ and $C_1 * \lambda_1 + C_2 * \lambda_2 = k_1 * D_0$.

This yields the following values of α and β for the dissociation of 1,3-CHDN:

$$\alpha = D_0 * k_2 * \frac{k_1}{\lambda_1 * (\lambda_1 - \lambda_2)} \qquad (16)$$

$$\beta = -D_0 * k_2 * \frac{k_1}{\lambda_2 (\lambda_1 - \lambda_2)}$$

The delay curves shown in Figure 8 were taken using the ArF excimer laser (193nm) described previously as the dissociation source. The theoretical fits were calculated according to equation 11 with the appropriate α and β's as given by equations 15 and 16. Full delay curves (which included the rising edge due to H_2 evolution and the decaying part due to H_2 moving away from the probe region) were measured for various pump beam diameters. The falling edge was successfully modeled using the geometrical factors of the experiment. This analysis is presented below. A pump beam diameter of 8mm was used for the curves shown in Figure 8 under which conditions the H_2 signal did not start falling off significantly until after 200ns, well after both the 1,3-CHDN and 1,4-CHDN signals had leveled off.

In order to account for the decay of the H_2^+ signal it was necessary to model the geometry of the experiment. If the photolysis beam and the molecular beam are both of diameter R then the initial excited CHDN distribution is located in a volume given by the intersection of two cylinders of diameter R. For ease of computation this was modeled as a sphere with a Gaussian $CHDN^*$ density distribution of FWHM = R. R in these experiments ranged from 2mm to 8mm. The probe beam intersected the sphere, passing through the center, with a radius of $\approx 100\mu$ at the center. The detection area was taken as a sphere of radius r_0 located at the center of the interaction area. While physically this is not a very satisfying approximation, it greatly reduces the amount of computation necessary and, as will be shown later, does a very satisfactory job of reproducing the decay of the H_2^+ signal.

Using the above geometry it is easily shown that the probability that H_2 molecules formed a distance R from the detection region would cross that region is proportional to r_0^2 and is inversely proportional to R^2. Furthermore, at time t one would sample the surface of a sphere of radius R where R is given by $R(t)=v_{H2}*(t-t0)$ and v_{H2} is the velocity of the H_2 molecules. Thus the number density of H_2 molecules in the interaction region at time t is given by:

$$N_{H_2}(t) = 4\pi R^2 dR \left\langle \frac{r_0^2}{R^2} \right\rangle N(R) \qquad (18)$$

where N(R) is the radial distribution function of H_2 molecules. This reduces to:

$$N_{H_2}(t) = 4\pi v_{H_2} dt * r_0^2 * N[R(t)] \qquad (19)$$

To fit the H_2+ intensity curves the function $N_{H2}(t)$ from equation (19) was convoluted with a Gaussian H_2 velocity distribution with a peak velocity and FWHM given by the experimental measurements. This was then convoluted with the H_2 appearance function given by equation (11) with the appropriate α and β parameters.

Laser delay curves showing the H_2^+ signal decay for photolysis laser beam diameters of 3mm, 5mm, and 8mm are presented in Figure 9 along with the best fit given by the above analysis. The H_2 was ionized via the B←X (1,1) R(1) transition. The H_2 velocity was taken as $1x10^6$cm/s and the FWHM of the velocity distribution as $6x10^5$cm/s. The three scans (3mm, 5mm, and 8mm) were fit with dissociation volume FWHM's of 3mm, 4.5mm and 6.5mm respectively. Discrepancies between the measured H_2^+ signal and the fits are accorded to the non-spherical nature of the dissociation volume. The larger deviation between the FWHM of the fit and the size of the photolysis beam for the 8mm scan is attributed to the width of the molecular beam (≈6mm).

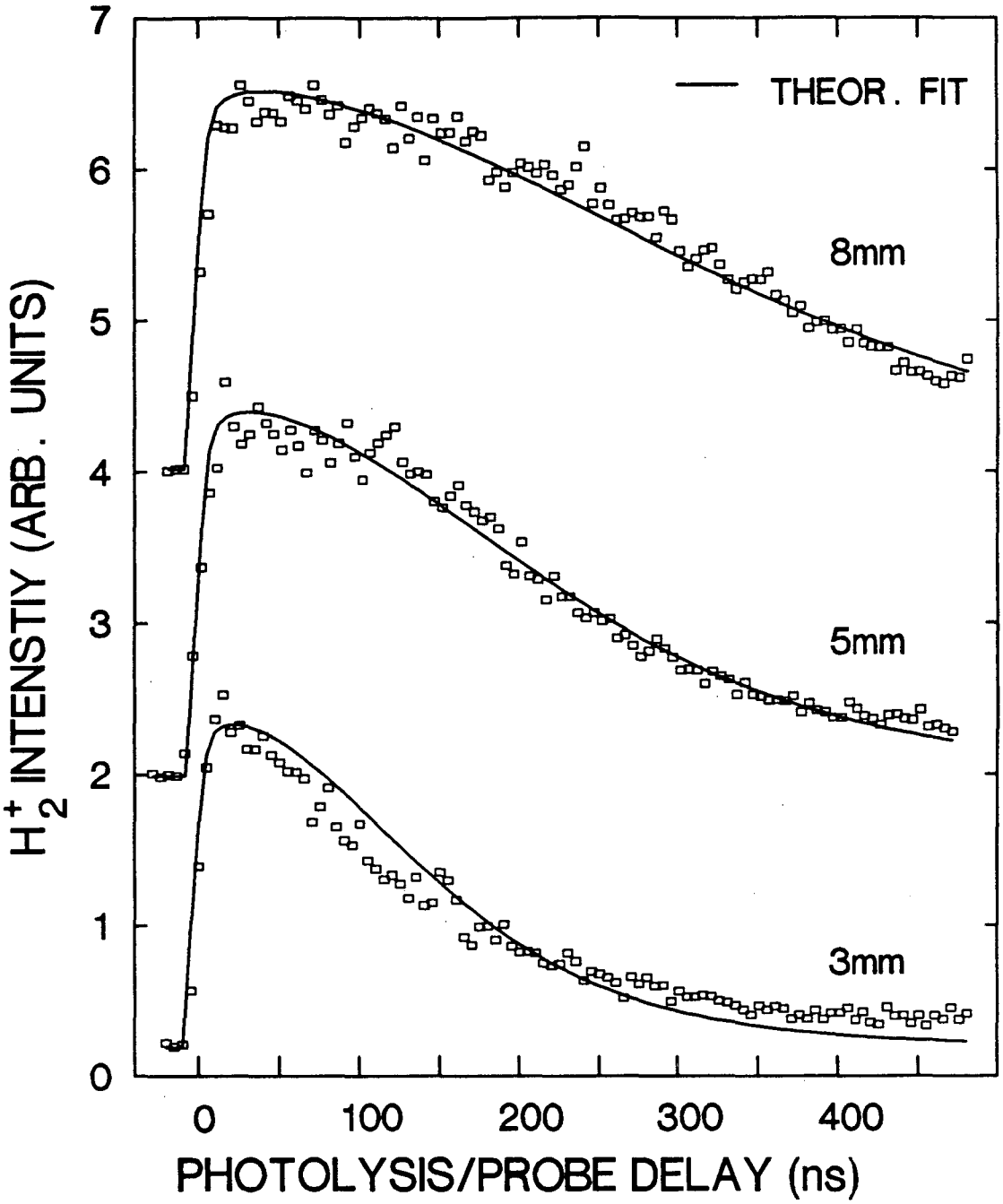

Figure 9. Long time behavior of the photolysis/probe laser delay scans for H_2 product from the dissociation of 1,4-CHDN. The scans shown are: (Top trace) 8mm diameter photolysis beam, (middle trace) 5mm diameter photolysis beam, and (bottom trace) 3mm diameter photolysis beam. The solid lines are the theoretical fits described in the text. The scans were scaled to equal peak height.

In order to successfully fit the time dependent yield curves it was necessary to include a correlation function between the two lasers. This was accomplished as follows. The probe laser was set resonant with the H_2 C-X (1,0) Q(1) transition, the monochromator was set to 1st order and a small amount of H_2 ($1x10^{-5}$torr) was introduced into the main chamber through a needle valve. The excimer laser was then used as the ionizing laser for the (1+1) REMPI of the H_2. The laser correlation function was then measured by varying the pump/probe laser delay and monitoring the H_2^+ signal. This curve was fit fairly well with a Gaussian distribution with a FWHM=12ns. This Gaussian was then convoluted with the H_2 evolution functions given above to fit the delay curves in Figure 8 and 9.

An RRKM calculation was performed with 26 modes counted to obtain theoretical values for k_1, k_2, k_3, and k_4. The results of this calculation are given in Table IV along with the experimentally obtained results from the best fits of the delay curves. As one can see there is fairly good agreement among all the rates except for k_4, which is the ring opening process. The initial ring opening process from the electronically excited state should be even faster than the rate calculated using RRKM theory. One explanation for the much smaller rate for k_4 might lie in the fact that after the initial ring opening this process is reversible. If the ring opening and closing processes are fast on the

time scale of the experiment, which is indicated by the RRKM calculation and other reported results,[9] an equilibrium would be quickly reached between the linear and ring compounds and the effect on the long term reduction of H_2^+ signal would be small. Thus, the experimentally measured k_4 would represent the decay of 1,3-CHDN by some other process, such as H atom elimination, rather than by isomerization.

TABLE IV: KINETIC RATES FOR PHOTODISSOCIATION OF CHDN

RATE	EXP. VALUE	RRKM VALUE
k_1	$0.07ns^{-1}$	$0.23ns^{-1}$
k_2	$0.3ns^{-1}$	$0.94ns^{-1}$
k_3	$0.18ns^{-1}$	$0.93ns^{-1}$
k_4	$0.005ns^{-1}$	$11.0ns^{-1}$

D. V-J CORRELATION

In the previous angularly resolved, but non-state-selective, experiments involving photofragmentation translational energy spectroscopy the H_2 was observed to have an isotropic distribution.[1] This confirmed the expectation of a long dissociation lifetime (greater than one rotational period). As a result of this one would not expect to see any correlation between the electric field vector of the dissociation laser and the velocity (**v**) or rotational angular momentum (**J**) vectors of the H_2 product. However, this does not rule out the possibility of a

correlation between **v** and **J**. Evidence of a (**v**,**J**) correlation for H_2 would show up in differences in lineshapes between parallel (Q-branch) and perpendicular (P or R branch) transitions. The theory behind this has been well documented elsewhere and so will not be discussed in any detail here.[33,34,35,36,37,38]

Classically, one can calculate the expected lineshapes for pure $\mathbf{v} \parallel \mathbf{J}$ and $\mathbf{v} \perp \mathbf{J}$ using rotation matrices to project the transition dipole of the absorbing molecule onto the electric field vector of the probe light. The classical Doppler profiles for both a Q branch and a P or R branch transition where $\mathbf{v} \parallel \mathbf{J}$ and $\beta=0$ are shown in Figure 10. These were calculated for a single product velocity according to Hall et. al.[33] However, this analysis is only good in the high J limit ($J > 7$) where the H_2 can be thought of as a rigid rotor. For H_2 formed in a low J state quantum effects become quite important and one must take into account the projection of the rotational angular momentum vector along the electric field vector axis, m_J. A series of lineshapes for J=1 to 9 for both a Q-branch and a R-branch transition resulting from pure $\mathbf{v} \parallel \mathbf{J}$ correlation are also shown in Figure 10. These were calculated using a quantum mechanical formulation given by Hall et. al.[33]

A series of Doppler profiles for H_2 product formed in the v"=0 state from the photodissociation of 1,4-CHDN is shown in Figure 11. Figure 11A shows a R(3), a P(7) and a

Figure 10. Calculated lineshapes for **v** ∥ **J** according to Ref. 33 for H_2 C←X transition when J"=1, J"=3, J"=5, J"=9, and the classical limit (J"=∞). The ∥ transition (Q-branch) lineshapes are shown in 10A and the ⊥ transition (R-branch) lineshapes are shown in 10B.

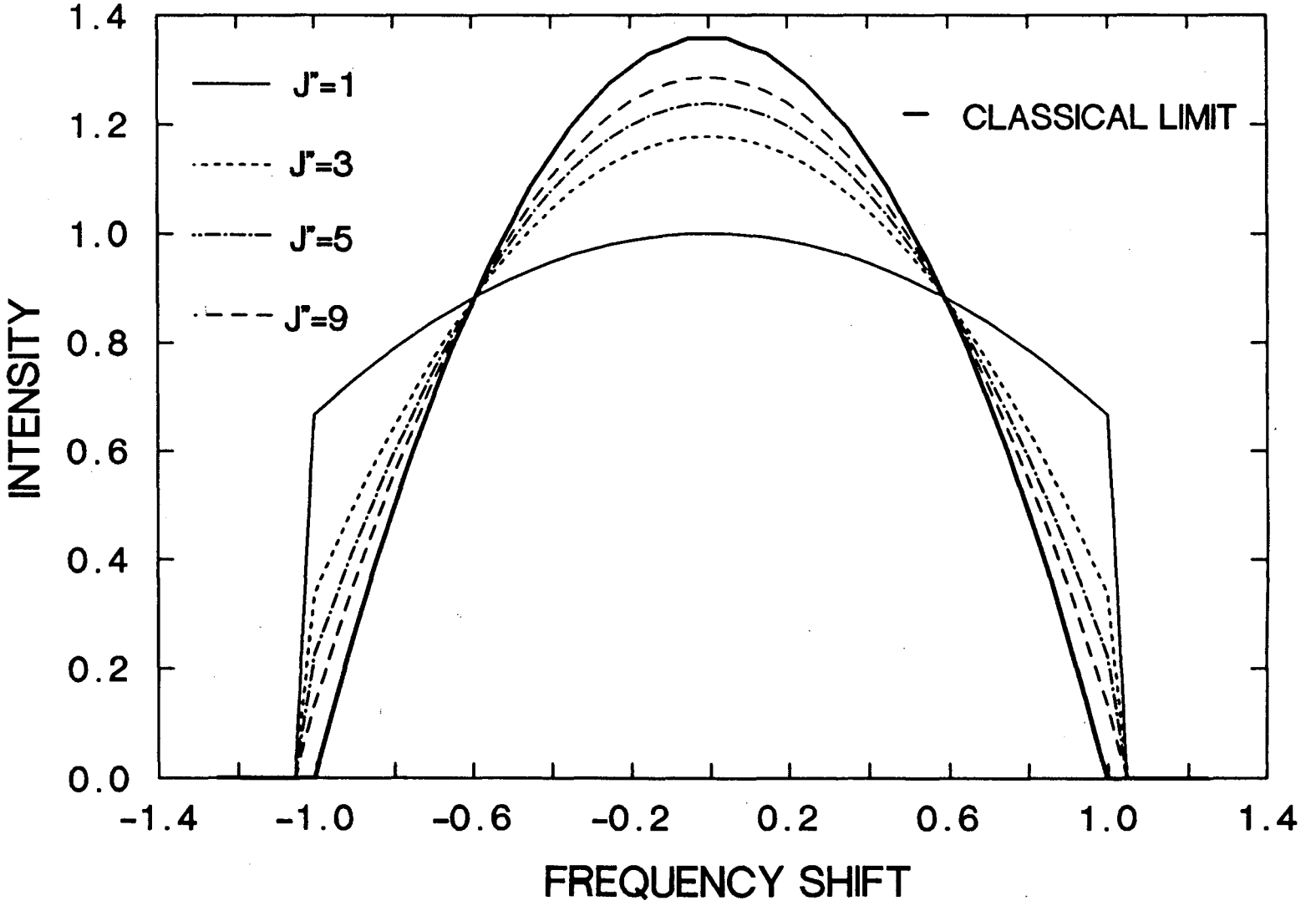
1.4
1.2
1.0
0.8
0.6
0.4
0.2
0.0
INTENSITY
J"=1
J"=3
J"=5
J"=9
CLASSICAL LIMIT
-1.4
-1.0
-0.6
-0.2
0.2
0.6
1.0
1.4
FREQUENCY SHIFT

Figure 10A

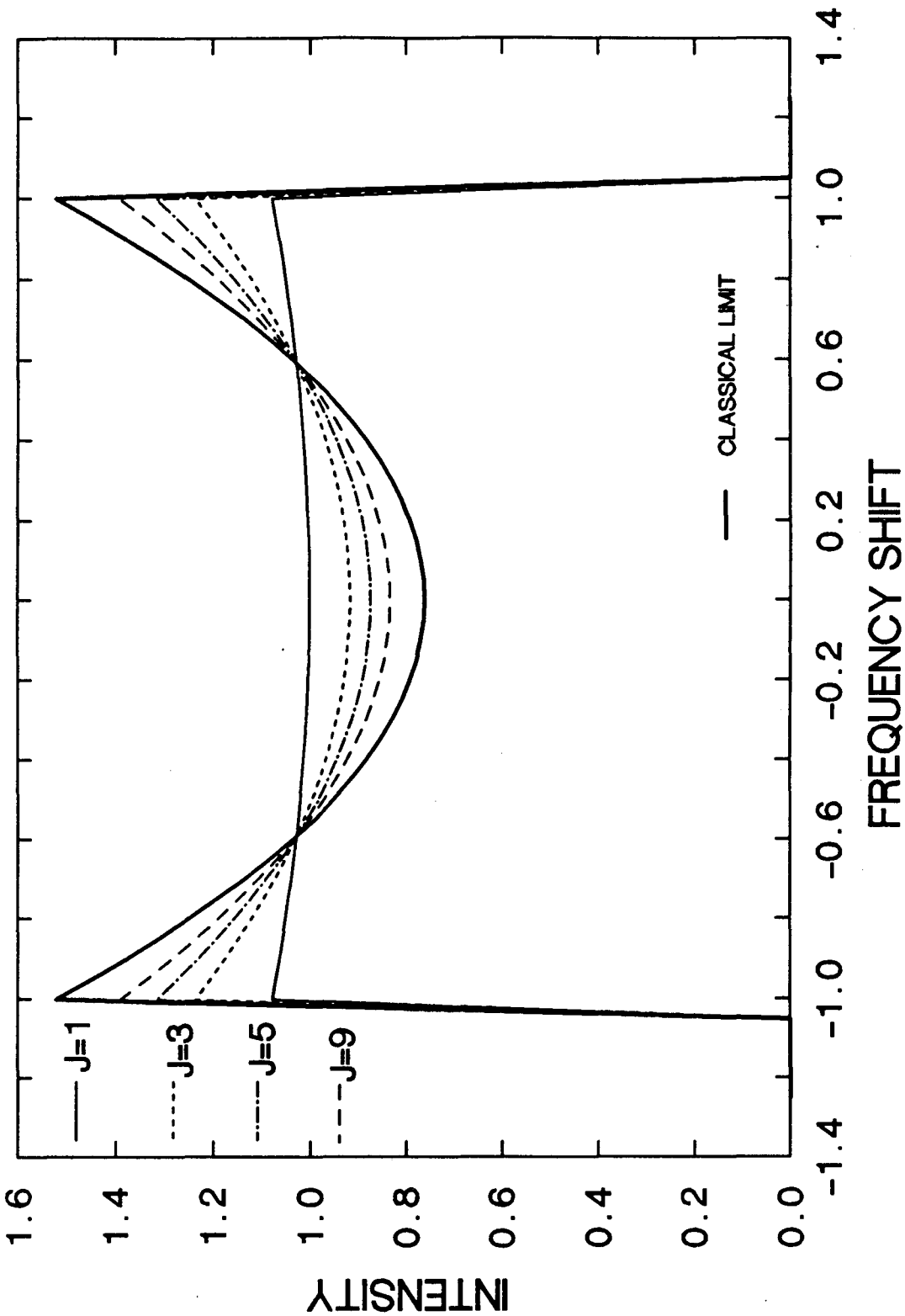
INTENSITY
1.6
1.4
1.2
1.0
0.8
0.6
0.4
0.2
0.0
J=1
J=3
J=5
J=9
-1.4
-1.0
-0.6
-0.2
0.2
0.6
1.0
1.4
FREQUENCY SHIFT
CLASSICAL LIMIT

Figure 10B

P(9) transition while in 11B is shown a Q(3), a Q(5) and a Q(9) transition. The fitting was done in the same manner as described in section III(B). The data presented in Figure 11 was taken under slightly different conditions then the previous data. The dissociation laser was the excimer laser (discussed above) and it was aligned counter propagating to the probe beam with a spot size of 3mm diameter. The dissociation laser was unpolarized and the pump/probe timing was 20ns. A direct comparison of the P and Q-branch transitions for J"=9 is shown in Figure 12.

This data fits well with the interpretation of having $\mathbf{v} \parallel \mathbf{J}$ for H_2 in the v"=0 state. The Q-branch transition lineshapes are rounded, with the roundness becoming much more pronounced as J increases, while the P and R-branch lineshapes are much more square. However, the anisotropy is not as pronounced as is predicted by the quantum mechanical calculations. Two reasons for this are that the spread in the H_2 velocities tends to "wash out" any features in the Doppler profile and, perhaps most importantly, the (v,J) correlation is not perfect.

In the previous communication regarding this experiment[14] the R(3) transition had a more pronounce dip. The author feels that this might have been caused by too long of a delay between the photolysis and probe laser (>100ns). This effect, reported previously as velocity aligned Doppler spectroscopy (VADS),[39] is a result of

Figure 11. Measured Doppler profiles showing variation of lineshapes with increasing J" quantum number. 11A Bottom Trace (♦): H_2 C←X (1,0) Q(3) (β=0.19, v_D=3.33cm^{-1}, $\upsilon(0)$=101,037.63cm^{-1}); Middle Trace (▲): H_2 C←X (2,0) Q(5) (β=0.35, v_D=3.30cm^{-1}, $\upsilon(0)$=100,509.99cm^{-1}); Top Trace (+): H_2 C←X (2,0) Q(9) (β=0.65, v_D=3.50cm^{-1}, $\upsilon(0)$=100,898.40cm^{-1}) transitions. 11B Bottom Trace (■): H_2 C←X (1,0) R(3) (β=-0.06, v_D=3.30cm^{-1}, $\upsilon(0)$=101,270.95cm^{-1}); Middle Trace (+): H_2 C←X (2,0) P(7) (β=-0.15, v_D=3.24cm^{-1}, $\upsilon(0)$ = 101,531.22cm^{-1}); Top Trace (□): H_2 C←X (3,0) P(9) (β=-0.13, v_D=3.65cm^{-1}, $\upsilon(0)$=102,447.60cm^{-1}) transitions.

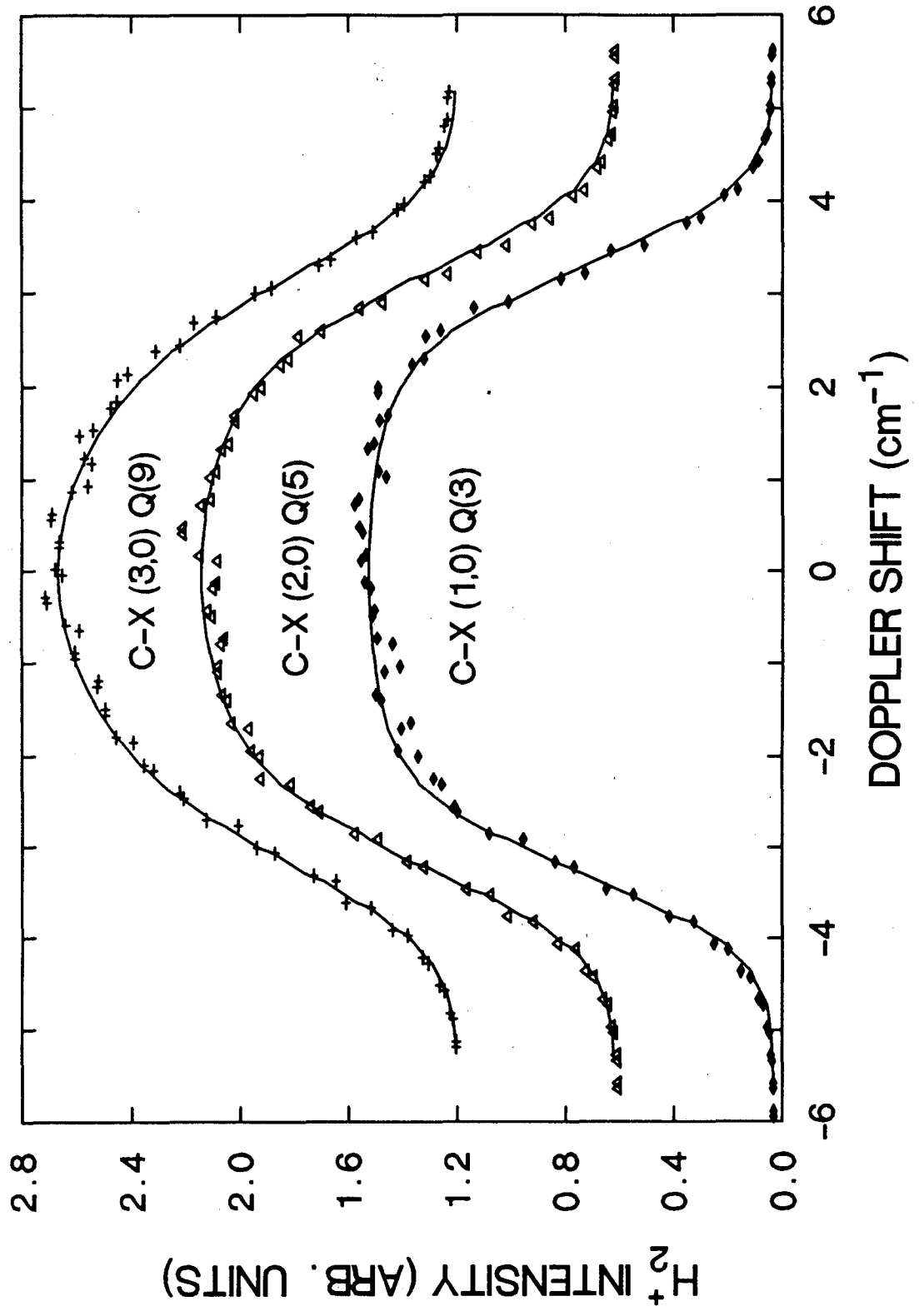
C-X (3,0) Q(9)
C-X (2,0) Q(5)
C-X (1,0) Q(3)
DOPPLER SHIFT (cm^{-1})
H_2^+ INTENSITY (ARB. UNITS)
-6
-4
-2
0
2
4
6
0.0
0.4
0.8
1.2
1.6
2.0
2.4
2.8

Figure 11A

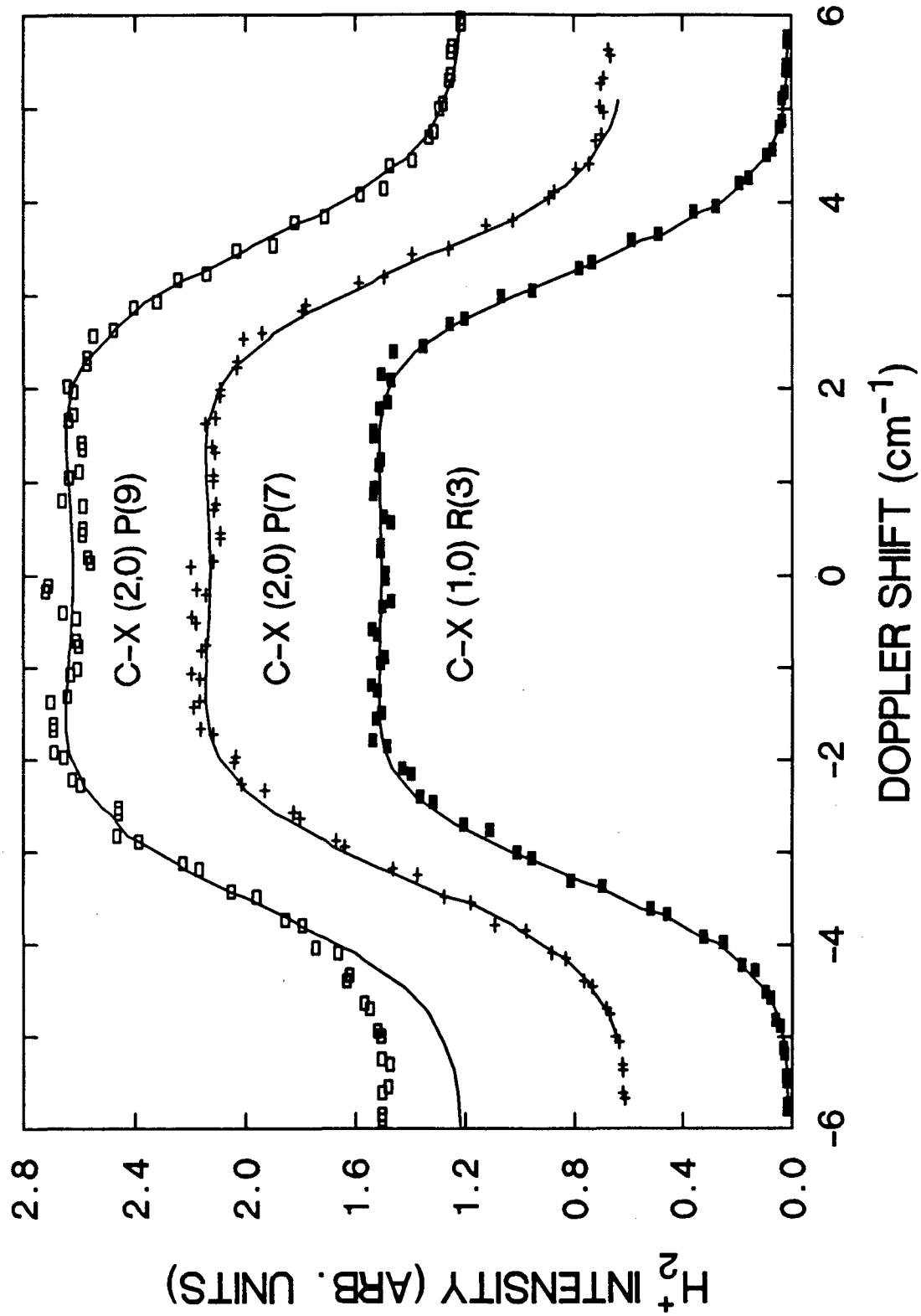
C-X (2,0) P(9)
C-X (2,0) P(7)
C-X (1,0) R(3)
DOPPLER SHIFT (cm^{-1})
H_2^+ INTENSITY (ARB. UNITS)
6
4
2
0
-2
-4
-6
2.8
2.4
2.0
1.6
1.2
0.8
0.4
0.0

Figure 11B

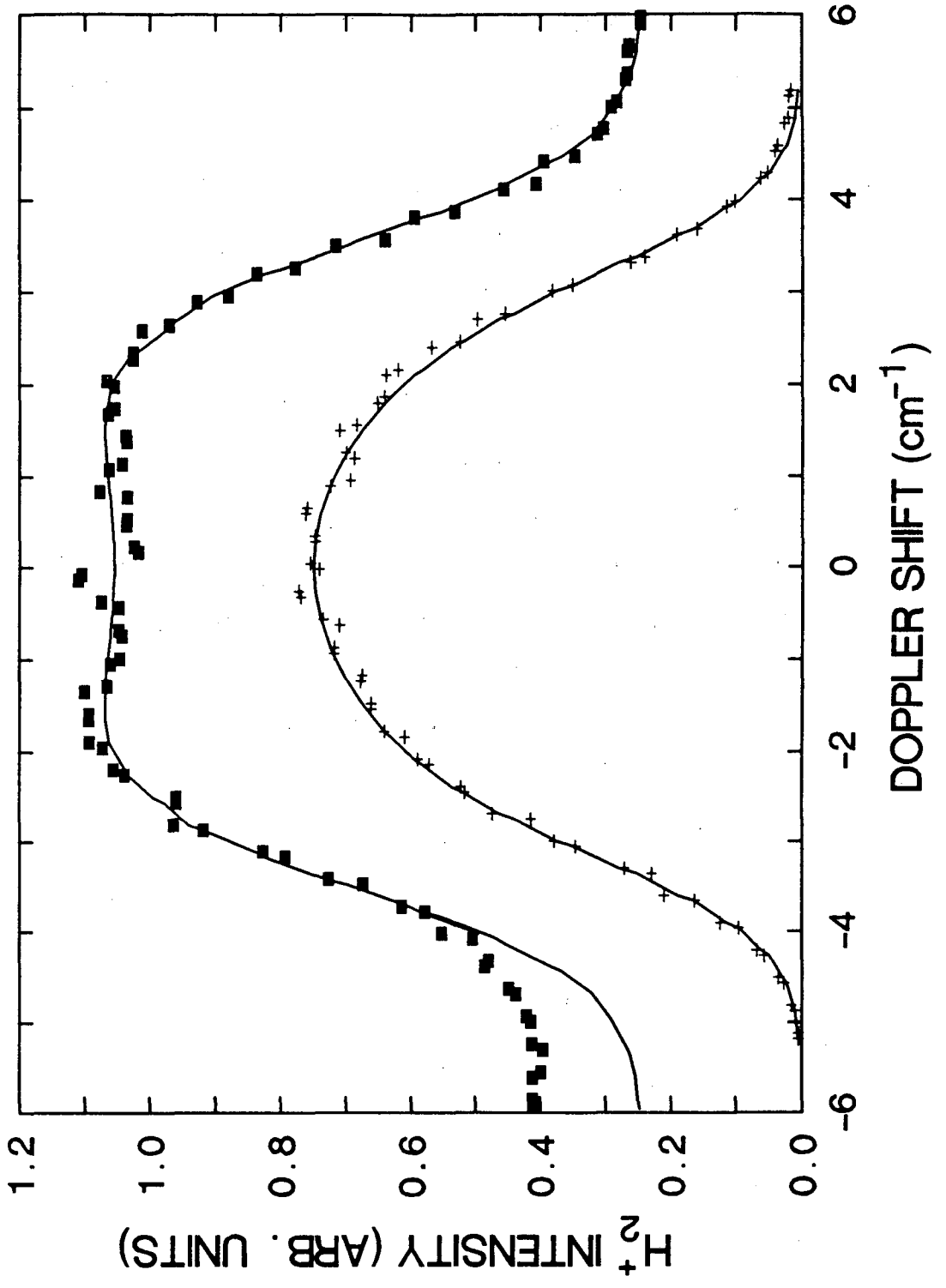

Figure 12. Comparison of the H_2 C←X (3,0) P(9) (top trace: ■) and (2,0) Q(9) (bottom trace: +) transitions shown in Figure 11.

product with zero Doppler shift (where the velocity vector is aligned perpendicular to the probe beam) flying out of the probe region and thus being discriminated against. Since the Q(3) transition did not exhibit the same effect this means that the interpretation of having a (v,J) correlation with $\mathbf{v} \parallel \mathbf{J}$ is still valid but that the correlation is just not as strong.

From this data it is concluded that the H_2 comes away from the transition state with a "helicopter" type motion, albeit a wobbly helicopter. A cartoon of a critical configuration that would lead to this type of motion is shown in Figure 13. This is the first known observation of this type of correlation for H_2.

There was no conclusive evidence of any (v,J) correlation for H_2 generated in higher vibrational states. Unfortunately it was not possible to measure any Q-branch transitions for states with v">0 although many attempts were made. One possible explanation is that the transition states leading to vibrationally excited H_2 are significantly enough distorted to destroy any correlation or, at least, to wash it out to the point where it was not able to be detected.

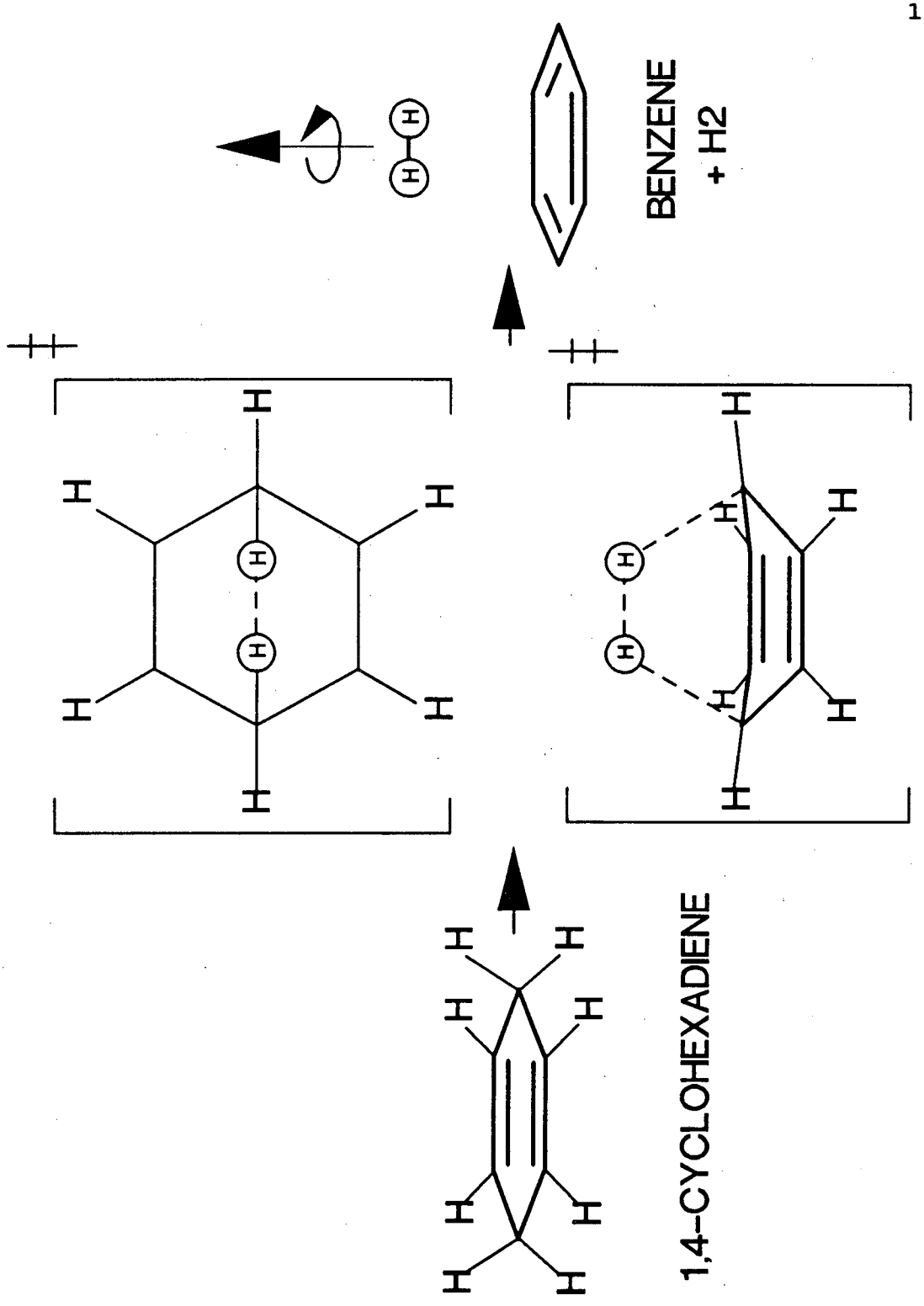

Figure 13. Cartoon of H_2 elimination from 1,4-CHDN showing a side and a top view of the transition state region and the helicopter motion of H_2 product.

IV. SUMMARY

The analysis of product quantum state and translational energy distributions can be a powerful tool for investigation of the transition state region of any reactive process. In the case of the photodissociation of 1,4-cyclohexadiene to form H_2 and benzene the characterization of the H_2 product in this way is particularly illuminating. The H_2 vibrational and rotational energy distributions indicate a tight and symmetric transition state which is supported by theoretical calculations. The distribution of H_2 translational energy both over a given ro-vibrational state and over all the populated quantum states confirms the concerted and synchronous nature of the dissociation process and the dominance of the potential energy barrier to the release of the translational energy of the H_2 product. Further information has also been derived from a correlation between the velocity and rotational angular momentum vectors of the H_2 product indicating that the H_2 moves away from the transition state complex with a helicopter type motion.

In conjunction with the angularly resolved photofragment translational energy measurements of the photodissociation of 1,4-CHDN, which provide a "global" picture of the reaction process, the results described above give a nearly complete picture of the H_2 elimination in this unimolecular decomposition. It is beyond the scope of these experiments to fill in the missing part, the internal energy

distribution of the benzene fragment. It should be possible for future experiments to distinguish for a given reaction H_2 product from different reactive pathways as long as there is enough difference in either translational, rotational or vibration energy.

REFERENCES

1. X. Zhao, R.E. Continetti, A. Yokoyama, E.J. Hintsa and Y.T. Lee, J. Chem. Phys. **91** 4118 (1989).

2. A. Yokoyama, X. Zhao, E.J. Hintsa, R.E. Continetti, and Y.T. Lee, J. Chem. Phys. **92**, 4222 (1990).

3. A.H. Kung, T. Trickl, N.A. Gershenfeld, and Y.T. Lee, Chem. Phys. Lett. **144**, 427 (1988).

4. R. Srinivasan, J. Chem. Phys. **38**, 1039 (1963).

5. R.J. Ellis and H.M. Frey, J. Chem. Soc. A **5**, 553 (1966).

6. S.W. Benson and R. Shaw, J. Am. Chem. Soc. **80**, 5351 (1967).

7. S.W. Orchard and B.A. Thrush, Proc. R. Soc. Lond. A. **337**, 257 (1974).

8. R. Srinivasan, L.S. White, A.R. Rossi, and G.A. Epling, J. Am. Chem. Soc. **103**, 7299 (1981).

9. P.J. Reid, S.J. Doig, and R.A. Mathies, Chem. Phys. Let. **156**, 163 (1989).

10. G. Dallinga and L.H. Toneman, J. Mol. Struc. **1**, 117 (1967).

11. D.C. Tardy, A.S. Gordon, and W.P. Norris, J. Phys. Chem. **80**, 1398 (1976).

12. I. Dabrowski, Can. J. Phys. **62**, 1639 (1984).

13. E. Roueff, private communication.

14. E.F. Cromwell, D.-J. Liu, M.J.J. Vrakking, A.H. Kung, and Y.T. Lee, J. Chem. Phys. **91**, 3230 (1990).

15. M. Page, private communication.

16. K.N. Houk, private communication.

17. E. Cromwell, T. Trickl, Y.T. Lee, and A.H. Kung, Rev. Sci. Inst. **60**, 2888 (1989).

18. T. Trickl, M.J.J. Vrakking, E. Cromwell, Y.T. Lee, and A.H. Kung, Phys. Rev., A **39**, 2948 (1989).

19. D. Proch and T. Trickl, Rev. Sci. Inst. **60**, 713 (1989).

20. R.H. Page, R.J. Larkin, A.H. Kung, Y.R. Shen, and Y.T. Lee, Rev. Sci. Intsr. **58**, 1616 (1987).

21. N.R. Daly, Rev. Sci. Instr. **31**, 264 (1960).

22. T.J. Butenhoff, K.L. Carleton, and C.B. Moore, J. Chem. Phys. **92**, 377 (1990).

23. R. Hilbig and R. Wallenstein, App. Opt. **21**, 913 (1982).

24. R.P. Frueholz, W.M. Flicker, O.A. Mosher, and A. Kuppermann, J. Chem. Phys. **70**, 1986 (1979).

25. R. McDiarmid and J.P. Doering, J. Chem. Phys. **75**, 2687 (1981).

26. R. McDiarmid, A. Sabljic, and J.P. Doering, J. Chem. Phys. **83**, 2147 (1985).

27. B.L. Sowers, E.T. Arakawa, and R.D. Birkhoff, J. Chem. Phys. **54**, 2319 (1971).

28. E.F. Cromwell, A. Stolow, M.J.J. Vrakking, and Y.T. Lee, (to be published).

29. R.H. Page, R.J. Larkin, Y.R. Shen, and Y.T. Lee, J. Chem. Phys. **88**, 2249 (1988).

30. G. Herzberg, **Spectra of Diatomic Molecules**, (Van Nostrand Reinhold, New York, 1950).

31. R. Hoffman, Trans. N.Y. Acad. Sci., 475 (1966).

32. R.B. Woodward and R. Hoffman, **The Conservation of Orbital Symmetry**, (VCH, New York, 1970).

33. G.E. Hall, N. Sivakumar, D. Chawla, P.L. Houston and I. Burak, J. Chem Phys. **88**, 3682 (1988).

34. R.N. Dixon, J. Chem. Phys. **85**, 1866 (1986).

35. P.L. Houston, J. Phys. Chem. **91**, 5388 (1987).

36. M.P. Docker, Chem. Phys. **135**, 405 (1989).

37. M. Mons and I. Dimicoli, J. Chem. Phys. **90**, 4037 (1989).

38. K.L. Carleton, T.J. Butenhoff, and C.B. Moore, J. Chem. Phys. **93**, 3907 (1990).

39. Z. Xu, B. Koplitz, and C. Wittig, J. Chem. Phys. **87**, 1062 (1987).

CHAPTER IV

DYNAMICS OF H_2 ELIMINATION FROM ETHYLENE

I. INTRODUCTION

In the previous chapter elimination of molecular hydrogen from an unsaturated hydrocarbon (1,4-cyclohexadiene) via a 6-centered transition state was investigated. In this chapter H_2 elimination from ethylene, one of the smallest unsaturated hydrocarbons, will be analyzed in a similar fashion. The detailed study of the unimolecular decomposition of ethylene (C_2H_4) has been of great interest to the scientific community for more than 30 years. The importance of this molecule comes from not only its value to industry as an precursor to many widely used materials but also from its value as a test of theoretical modeling for a 6-atom molecule.

Early experiments determined the major unimolecular reaction pathways for C_2H_4: elimination of H (reaction 1) and elimination of H_2 (reaction 2) to form acetylene.

$$C_2H_4 \rightarrow C_2H_2 + 2H \qquad (1)$$

$$C_2H_4 \rightarrow C_2H_2 + H_2 \qquad (2)$$

These experiments were typically performed in a "bulb" using a variety of excitation sources including radiolysis,[1,2] mercury sensitization,[3] flash photolysis[4] and discharge lamps.[5,6,7,8,9] However, a number of important questions remained regarding the structures of the intermediates and the electronic potential energy surfaces involved in the different reactive processes.

The next important breakthroughs came with the detection of two radical intermediates in the ethylene reaction scheme: the vinyl radical ($CH_2CH\cdot$) and vinylidene ($CH_2C:$). These species had both been predicted theoretically but it was not known whether their lifetimes would be long enough to permit detection. The presence of $CH_2CH\cdot$ was confirmed initially by detection of products which could only result from the presence of $CH_2CH\cdot$ in the reactive process.[4,10] The existence of the biradical, $CH_2C:$, was not confirmed till much later when appropriate laser light sources had been developed to detect it by spectroscopic means.[11,12,13] Even then the vinylidene formed was found to be in an electronically excited triplet state ($^3B_2$), instead of its ground singlet state, $A(^1B_{1u})$. The temporal evolution of the triplet species indicated that it was not the result of one of the primary processes but rather had decayed into the triplet state from some other electronic state.

The mechanism of H-atom elimination from C_2H_4 has been well characterized.[14,16,29] Following electronic excitation with a photon, $C_2H_4^*$ internally converts to its ground electronic state after which H-atom elimination occurs leading to the formation of $CH_2CH\cdot$. The vinyl radical can then either subsequently decay into acetylene plus another H-atom (provided the initial excitation energy is high enough) or react with other species that might be present.

The mechanism for the elimination of molecular hydrogen from C_2H_4, though, is not as well determined. The initial proposed reaction mechanism provided two pathways: a 3-centered elimination from one of the carbons leaving behind CH_2C: (reaction 3) or a 4-centered elimination across the carbon-carbon double bond forming acetylene directly (reaction 4).

$$H_2C\text{-}CH_2 \rightarrow H_2C\text{-}C\text{:} + H_2 \qquad (3)$$

$$H_2C\text{-}CH_2 \rightarrow HC\text{-}CH + H_2 \qquad (4)$$

From studies of deuterated species the ratio for H_2 production between these two pathways, (3) to (4), was determined to be approximately 3:2.[1,6,14]

A recent review on the photochemistry of ethylene by Collin[15] discusses, among other things, which electronic potential energy surfaces are involved in the elimination of molecular hydrogen from C_2H_4. Theoretical work that has been done indicates that H_2 elimination occurs from an electronically excited state of C_2H_4.[16,17] These arguments are based on Woodward-Hoffman symmetry selection rules for elimination from ground and excited states. Calculated potential energy barriers are lower for reaction occurring on the excited state potential surface than on the ground state potential surface. Further postulation involves ethylidene (CH_3CH) as a reactive intermediate. While energetically it is possible to form CH_3CH with the

excitation techniques used in the above experiments (and the experiment described here) it is not clear whether it is more likely for H_2 to eliminate from a "methyl" type structure, as would be the case for CH_3CH, or from the 4-centered transition state of ethylene.

The experiments reported in this chapter examine the H_2 elimination channels from C_2H_4. Using the H_2 detection technique previously reported[18,19,20] the rotational, vibrational, and translational energy distribution in the H_2 product from the photodissociation of C_2H_4 at 193nm was measured. The 193nm photon excites a $\pi^* \leftarrow \pi$ transition from the ground electronic state, $N(^1\Sigma_g^+)$, to the first excited singlet state, $V(^1\Sigma_u^+)$, of C_2H_4.[21] The energy deposited (148kcal/mole) is well above the activation barriers for H_2 elimination.[16] The D-atom elimination channel from C_2D_4 was also examined for information on the translational energy of the D product.

In order to be able to distinguish between the two H_2 elimination channels further experiments with deuterated ethylene were carried out. H_2 product from the dissociation of 1,1-d_2 ethylene was analyzed in the same manner as above. This allowed direct comparison between the products from the 3-centered and 4-centered H_2 elimination channels of ethylene. The data presented below indicates that there are two distinct channels for formation of H_2 which impart significantly different amounts of energy into the different

degrees of freedom of the H_2 product.

II. EXPERIMENTAL

The molecular beam apparatus and the vuv-xuv laser system used are the same as described in Chapter II and Chapter III. The main difference between the experimental set-up described below and those in Chapter III is in the photolysis source. For the C_2H_4 experiments an ArF excimer laser (Lambda-Physik EMG-103-MSC) was used as the dissociation source. This, along with other differences, will be described in more detail below. A view of the set-up of the laser and molecular beams in the main chamber is shown in Figure 1.

The ArF laser used as the photolysis source had an output of >100mJ in 20mm x 5mm rectangular beam. The temporal pulse width was 20ns and the pulse to pulse jitter was $< \pm$ 1ns. An unstable resonator was utilized in order to provide a uniform photolysis beam intensity in the interaction region and to minimize energy loss due to beam divergence along the ≈3m path from the laser to the molecular beam chamber. An 8mm diameter section of the beam (the aperture was in front of the main chamber where the laser beam was slightly larger) containing ≈10mJ of energy was selected and sent into the main chamber where it was then focused to an ≈2mm spot size with a 50cm CaF_2 lens.

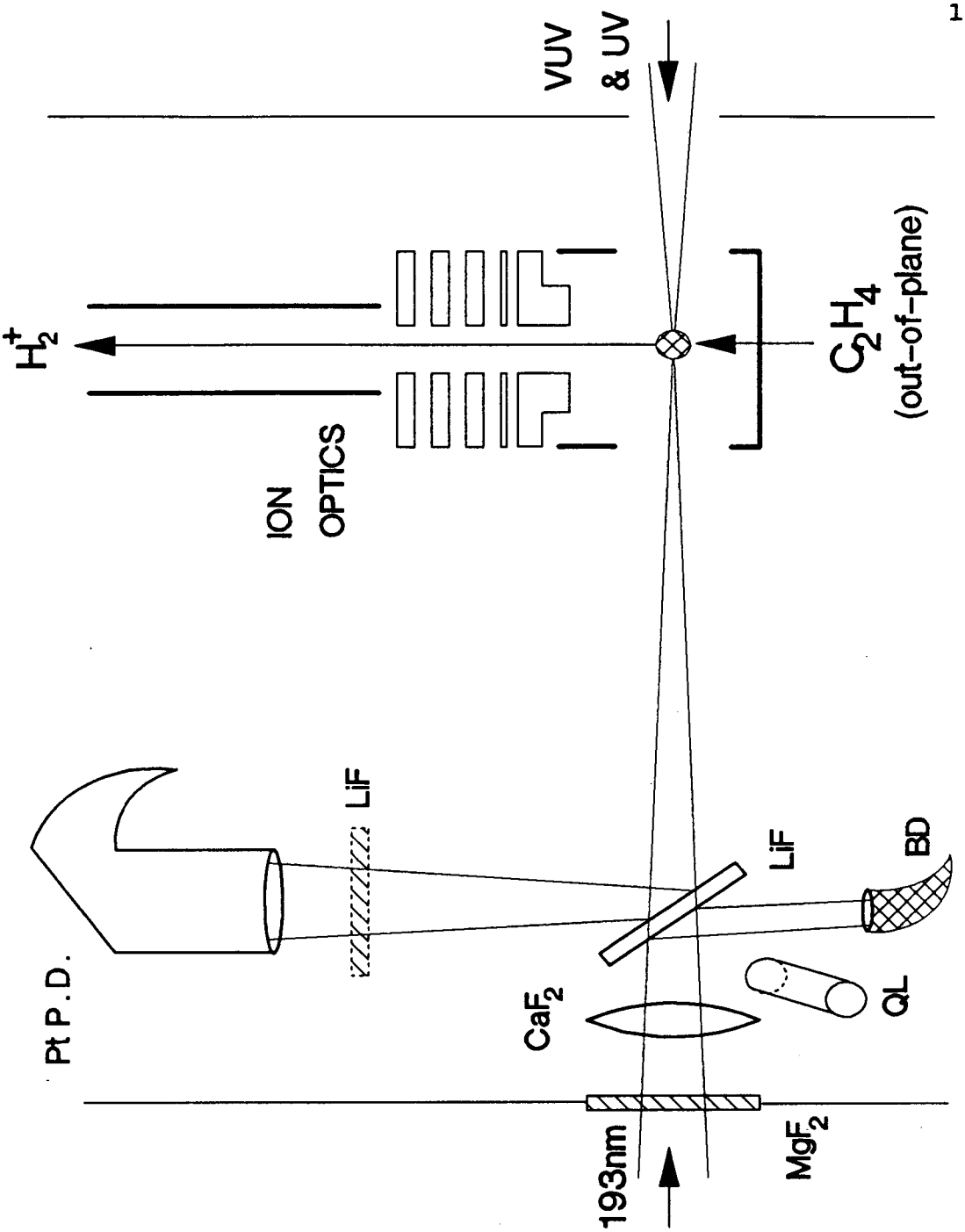

Figure 1. Blow-up of the interaction area in the main chamber for the dissociation of C_2H_4 experiment. The substrates of the various optical components are indicated. Pt P.D.=platinum photo diode, QL = quartz heat lamp, and BD = Wood's Horn beam dump for 193nm beam reflection.

Increasing the 193nm intensity in the interaction region by focusing to 2mm improved the amount of H_2^+ signal while minimizing any experimental artifacts, due to poor beam overlap with the tightly focused probe beam or multiphoton processes, that might occur with a tightly focused photolysis beam.

The beam steering optics were dichroic high reflecting, 45° mirrors coated for 193nm (Acton Research Inc.). The input window to the main chamber was a 25mm diameter, 3mm thick MgF_2 laser grade window which was rotated occasionally to prevent the formation of color centers. Condensation of pump oil onto the optics was a major problem due to its tendency to burn onto the surface of the optics when exposed to 193nm radiation. All optics inside the main chamber were kept warm in order to minimize this effect. It was found that a solution of H_2O_2 (≈10% in water) worked extremely well for removing burn marks on the optics due to pump oil.

The 699-29 laser used in these experiments is extremely sensitive to external sources of vibration which can cause unstable operation. Since the ArF laser was on an optics table that contacted the 699-29 laser it was necessary to vibrationally isolate the laser head (which contained a mechanically "noisy" gas processing unit) from the table. This was accomplished with a multi-layered pad which consisted of the following: 3/4" plywood, 1/8" neoprene rubber, 1/8" lead, and 1/4" cork, on top of the 1/4"

stainless steel table top. The laser head was held in place by gravity. Changes in laser pointing due to movement of the laser head was small compared to that caused by the pressurizing and depressurizing of the laser chamber when changing the laser gas and by cleaning the laser cavity optics (which requires removal of the optics). Electrical noise from the discharge in the laser chamber did not adversely affect the 699-29 laser (as it was greatly feared it would).

The photolysis laser beam was sent in counter-propagating to the probe laser. This was necessary in order to reduce the amount of background ions generated by photoelectrons from scattered 193nm radiation impinging on the metal surfaces of the main chamber. In this set-up the vuv grating in the monochromator was in the beam path of the laser which presented a problem. The energy density of the collimated ArF beam is greater than the damage threshold of the coating on the grating and thus would burn the coating if exposed directly onto the grating. For this reason the photolysis laser must be focused before the grating. Focusing the beam around the interaction region with a 50cm lens allows it to expand to a size large enough at the grating so as to cause no damage to the coating.

A pyroelectric detector (Molectron J3-09) measured the 193nm intensity transmitted through one of the high reflectance mirrors for normalization purposes. The

detector monitored the same part of the ArF laser output that was used to dissociate the C_2H_4. A sand-blasted fused silica window, used as a diffuser, was placed in front of the pyroelectric device as an attenuation source.

For xuv-vuv normalization a Pt photodiode (see Chapter II) was used to monitor the probe laser intensity after the interaction region. A 25mm diameter, 2mm thick LiF window was used to pick off a portion of the probe beam and send it directly in to the Pt P.D. (see Figure 1). This photodiode provided excellent discrimination against the uv light, which was collinear with the vuv radiation and $>10^4$ times as intense. The main source of background for the Pt P.D. was scattered 193nm photons. The energy of these photons is much closer to the 6eV work function of Pt then that of the uv photons in the probe beam. Care was taken to limit the amount of scattered 193nm radiation. A LiF window was placed in front of the photodiode when sum-frequency generation was utilized in order to filter out any residual straight tripled radiation that might be present.

For the measurements of D atom elimination it was necessary to generate Lyman-alpha radiation. The D atoms are then ionized via (1+1) REMPI in a similar fashion to the H_2 ionization. The radiation was generated by (2+2+1) sum-frequency mixing in a pulsed jet of Kr. This process has been previously reported in a low pressure gas cell.[22] The line center for the D atom Lyman-alpha transition is

≈82,282.65cm^{-1}. This requires making visible light at 16,456.53cm^{-1} (≈607.7nm) for the mixing processes. Using neutral R640 in the dye amplifier chain gave an output of approximately 90mJ at 608nm. This light was then doubled, giving >25mJ of uv light, and the collinear uv and visible radiation were focused by a 30cm achromat beneath the pulsed valve for the four-wave mixing process. The D^+ signal strength was >100 times greater than the strongest H_2^+ signals seen when resonantly ionizing background H_2 gas in the main chamber. Assuming 1% H_2 in the 10^{-6} torr of background gas in the main chamber, an upper limit on the detection sensitivity of the experiment for D atoms can be estimated to be ≈10^4 atoms/cm^3.

The normal ethylene was ultra-high purity grade (>99.995%) from Matheson. The 1,1-d_2 ethylene was obtained from MSD Isotopes and was 98% pure. The C_2D_4 was also obtained from MSD and was 99% pure. All gases were used neat and without any other purification.

For the determination of population distributions of H_2 products 800 mbar of C_2H_4 was expanded through the 0.5mm nozzle of a pulsed valve.[23] The pulse duration was ≈150μsec. The laser was timed to intersect the molecular beam 80μsec from the start of the pulse. A 1.02mm diameter skimmer (Gentry electroplate model) was located 1.5cm from the nozzle separating the source chamber from the differentially pumped main chamber. The distance from the

skimmer to the interaction region was 5cm. The source chamber pressure was 2 x 10^{-4}torr and the main chamber pressure was <2 x 10^{-6}torr when the valve was in operation. For the long photolysis/probe time delay studies the skimmer was changed to a low profile 2mm diameter model located 2cm from the nozzle and 4.5cm from the interaction region. When using the deuterated compounds the backing pressures were typically around 200mbar and the molecular beam pulse duration was reduced to 100μsec (to reduce gas consumption).

The ion extraction optics were the same as described previously and the voltage settings (1500V across the interaction region with the ions being accelerated to 2500eV) were similar. The molecular beam diameter was ≈5mm in the interaction region and the probe beam spot size was ≈100μm. The delay between the photolysis and probe beams was 20ns for the population scans. All H_2^+ generated by the probed beam was assumed to be collected.

The H_2^+ signal from the Daly ion detector was normalized to the vuv dependent signal from the Pt. P.D. and to the 193nm dependent signal from the pyroelectric detector. All signals acquired were processed by boxcars (SRS 250) and averaged slightly (1/3 of the data collection time constant) before being divided by analog processors (SRS 225/235). This was done to prevent overloading of the dividing circuits by the large fluctuations in the vuv intensity. The averaged output from the final analog

processor was then recorded by the 699-29 computer (Apple II). All data was transferred from the 699-29 to a PC computer for analysis.

III. RESULTS AND ANALYSIS

A. POPULATIONS

The vibrational distribution of the H_2 product from the dissociation of C_2H_4 at 193nm is shown in Figure 2. The rotational distributions of the same product for the vibrational levels v"=0 through v"=3 are shown in Figure 3. The population of each quantum state was measured a number of times ($n \geq 4$) using different transitions. The error bars in Figure 3 indicate the standard deviations of these measurements.

The lineshape of each transition was fit by a non-linear least squares method to the function:[24]

$$I \propto \frac{C}{v_D} * [1+\beta * P_2(\cos\theta) * P_2(\chi)] \qquad (5)$$

where v_D=maximum doppler shift, β=effective anisotropy parameter, P2=second order Legendre polynomial, θ=angle between the electric field vector of the linearly polarized photolysis laser and the direction of the probe laser, χ=Doppler shift/v_D, and C is proportional to the line intensity. This function was convoluted with a normalized Gaussian H_2 velocity distribution of a variable width. For

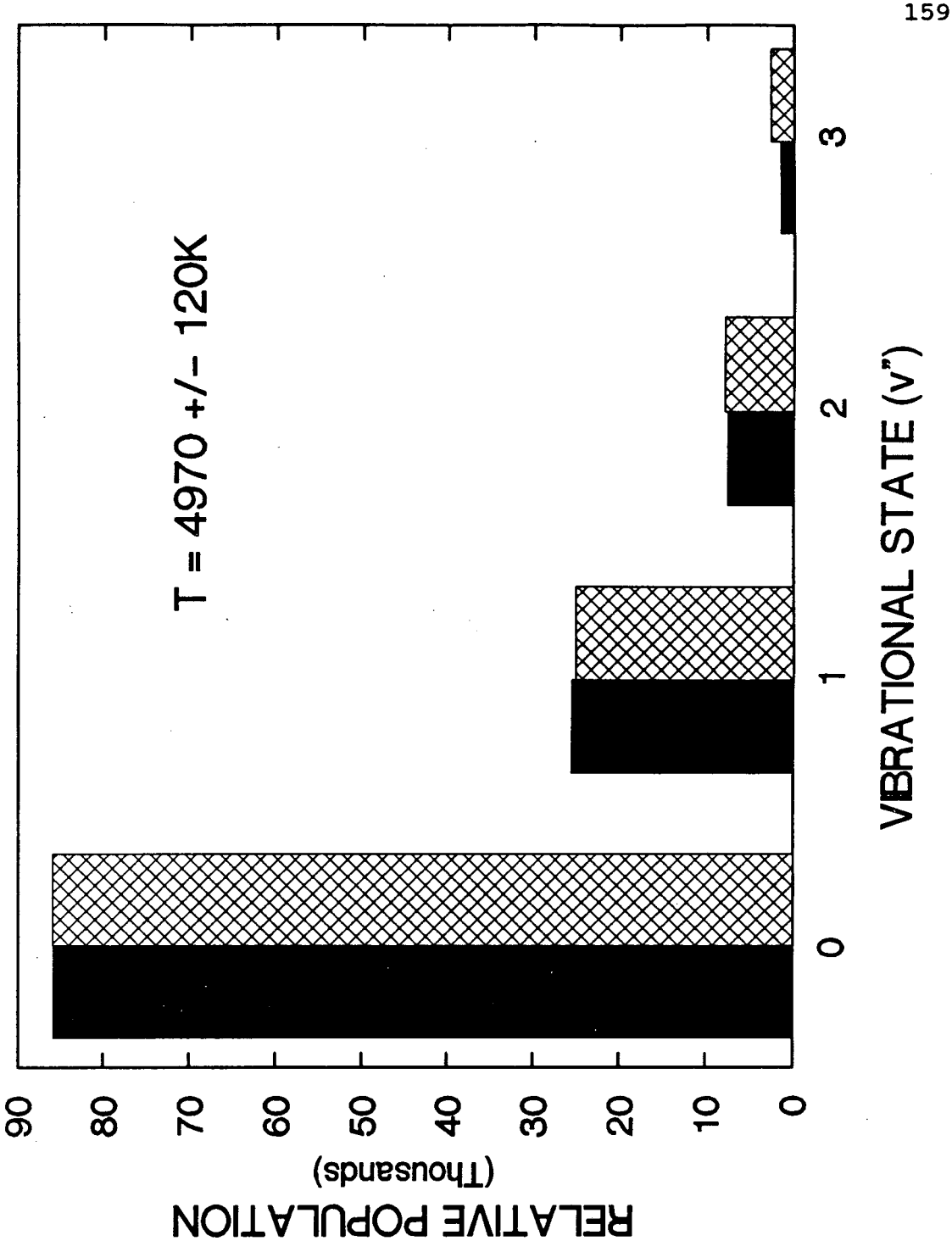

Figure 2. Distribution of vibrational energy in H_2 product from the dissociation of C_2H_4 (solid bars). A statistical fit to the distribution (T = 4970 ± 120K) is also shown (hatched bars).

Figure 3. Distribution of rotational energy in H_2 product from the dissociation of C_2H_4 for the vibrational levels v"=0 to v"=3. The various rotational distributions as well as the vibrational distribution (Fig. 2) have the same relative scale. The error bars represent ± one standard deviation of the measurements.

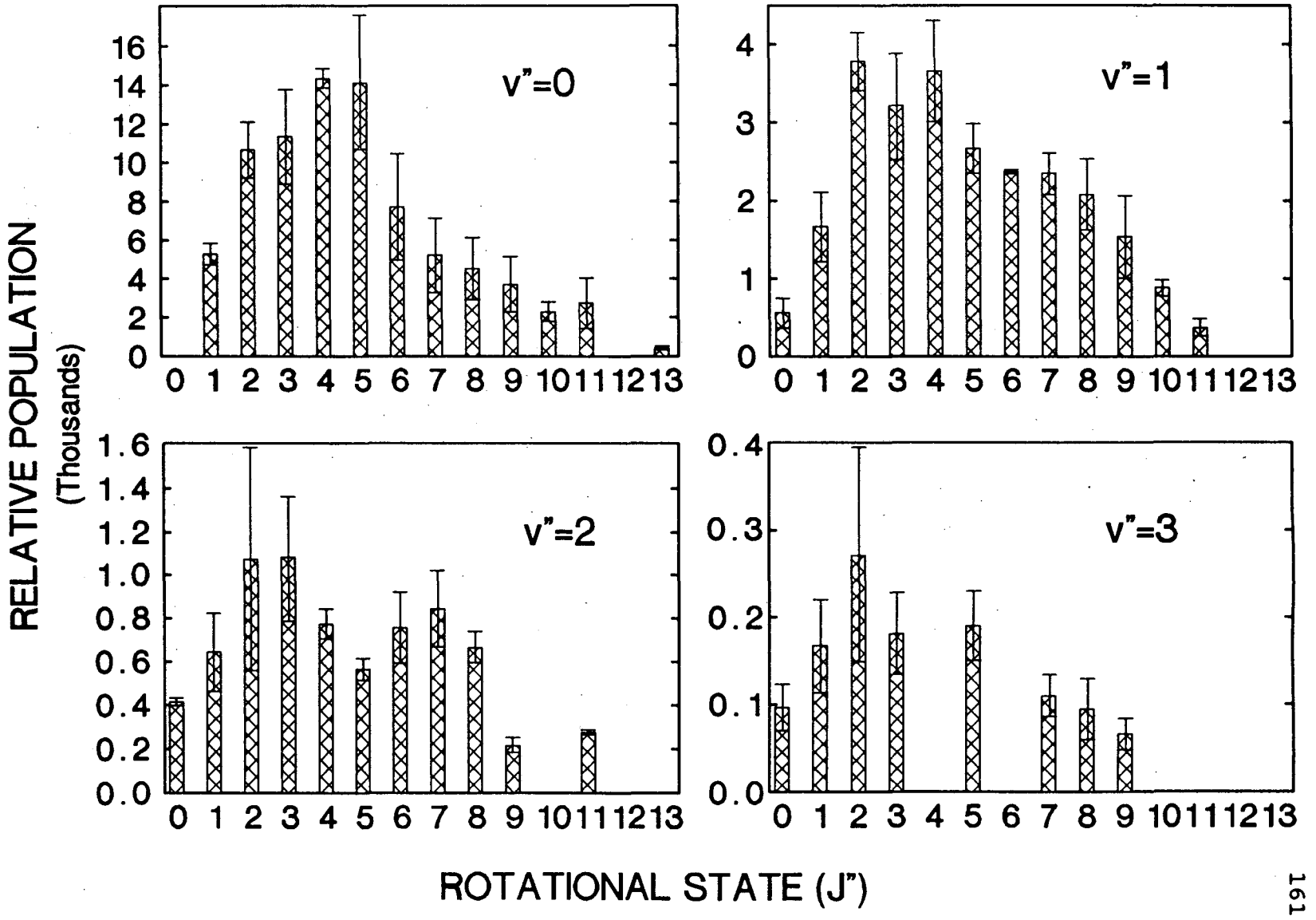
RELATIVE POPULATION
(Thousands)
v"=0
v"=1
v"=2
v"=3
ROTATIONAL STATE (J")

Figure 3

overlapping transitions partial fits were done to that part of the lineshape that exhibited no interference. Line intensity measurements from these partial fits were used in the population distributions but the doppler widths and anisotropy parameters were not considered reliable.

The relative H_2 populations were calculated from the measured line intensities in the same manner described previously.[20] When comparing populations for a given H_2 quantum state that were measured from different transitions (e.g. P-branch versus R-branch) significant discrepancies were noted. The large error bars seen for some of the H_2 quantum states in Figure 3 are a result of these discrepancies. Such differences had been seen previously when comparing the ratio of calculated H_2 emission probabilities to measured values.[25] The difficulty in calculating accurate linestrengths arises from perturbation of the energy levels due to rotational coupling between the $B^1\Sigma_u^+$ and $C^1\Pi_u$ electronic states of H_2. Reproducability for a given transition was very good attesting to the effectiveness of the normalization techniques used.

The rotational population distributions of H_2 product from 1,1-d_2 ethylene for the vibrational levels v"=0 and v"=1 are shown in Figure 4. The error bars for the v"=0 levels represent the standard deviations of the various population measurements. No vibrational distribution was measured for this product. A statistical non-linear least

squares fit to each of the vibrational levels[20] is also presented in Figure 4. The rotational temperatures calculated are 2500 ± 200K for v"=0 and 2000 ± 160K for v"=1. These temperatures are significantly less than those for the rotational distributions of H_2 product from normal ethylene.

The H_2 distributions from C_2H_4 were analyzed in the following manner. First the ratio of the amount H_2 product from the 3-centered channel (reaction (3)) to the 4-centered channel (reaction (4)) was taken (from previous measurements using deuterated compounds)[1,6,14] as 3:2. The total amount of energy available to the H_2 formed from reaction (3) is only 50-60 kcal/mole because of the high ΔH_f° of vinylidene (≈100 kcal/mole). The energy available to H_2 from reaction (4) is approximately twice as large at 106.3kcal/mole. (The ΔH_f°'s for all pertinent species in the dissociation of C_2H_4 are given in Figure 5.) Based on our observed experimental results it is assumed, for the purpose of fitting the rotational distributions, that the distribution of energy among the internal degrees of freedom for both channels is specified by a given temperature and that the vibrational temperature of H_2 from reaction (3) is half that of the other channel or, $T_v(1,1) = \frac{1}{2} * T_v(1,2)$. With the above two parameters and the total H_2 vibrational energy distribution it is possible to calculate a bimodal vibrational distribution and to assign a percent composition of the

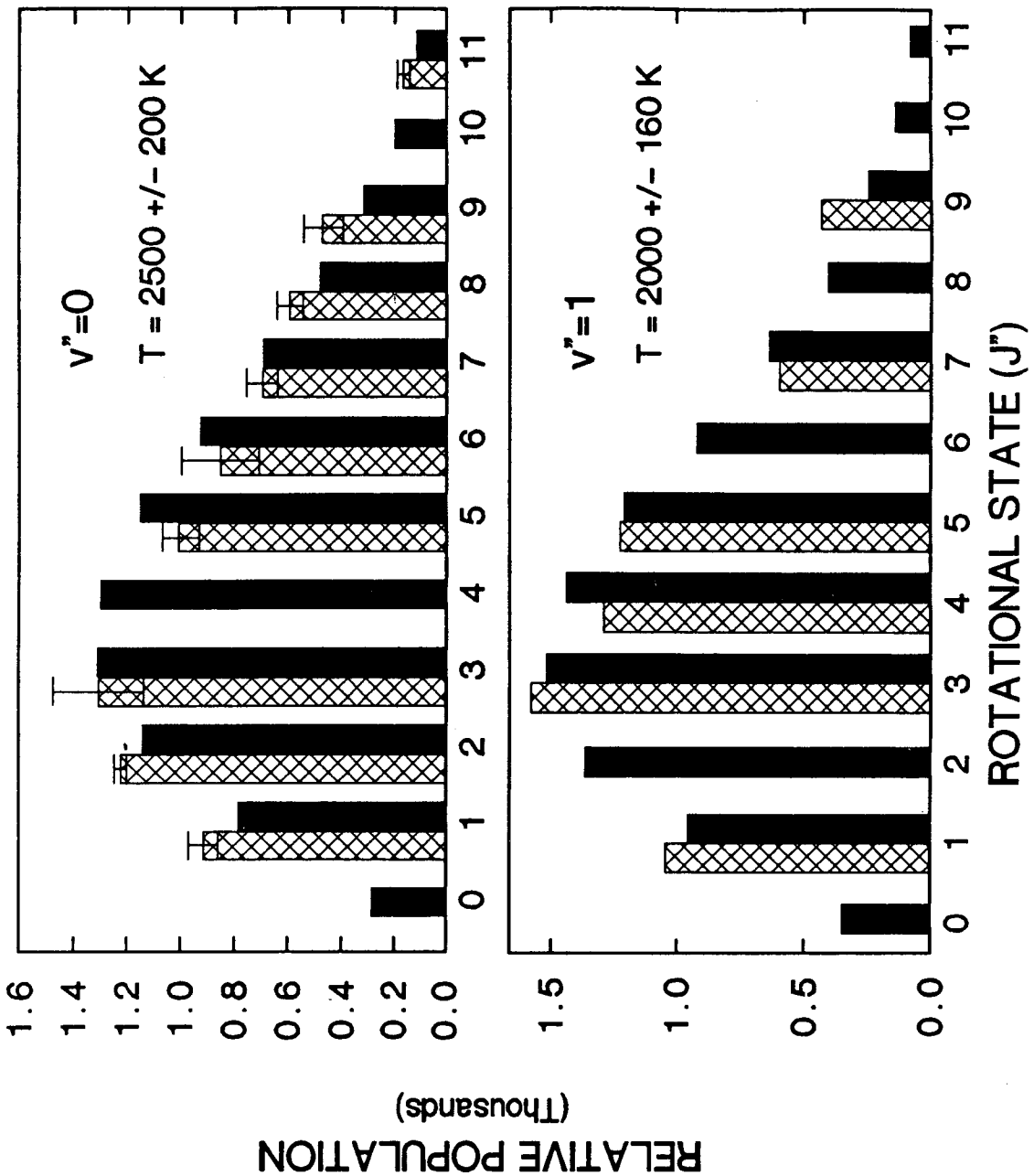

Figure 4. Distribution of rotational energy in H_2 product from the dissociation of 1,1-d_2 ethylene for the vibrational levels v"=0 and v"=1 (hatched bars). Statistical fits to the distributions (T_R(v"=0) = 2500 ± 200K, T_R(v"=1) = 2000 ± 160K) are also shown (solid bars). The error bars represent ± one standard deviation of the measurements. The distributions are not scaled to each other.

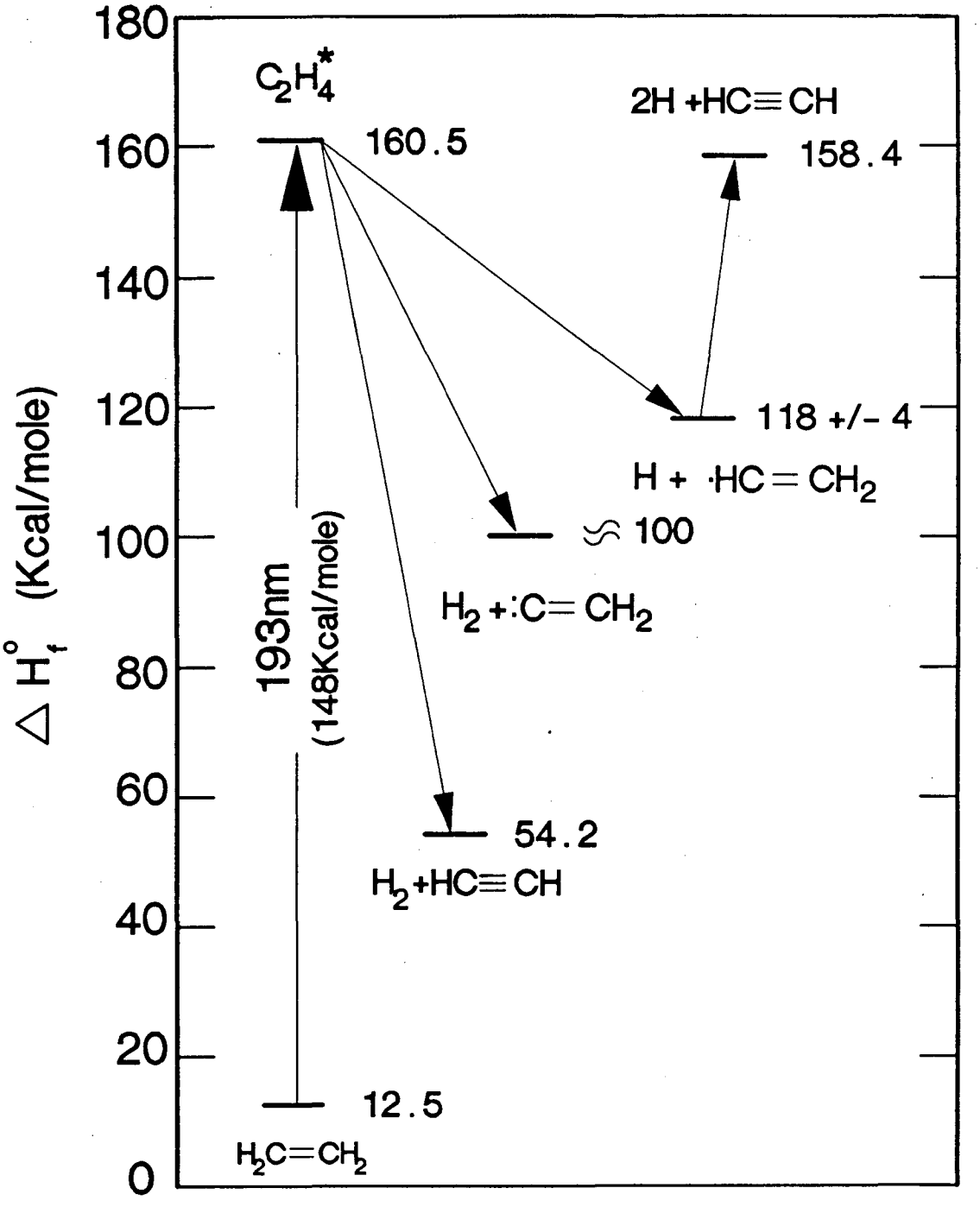

Figure 5. Standard heat of formations of the pertinent species involved in the dissociation of C_2H_4 at 193nm. Energies are given in kcal/mole.

different reaction products to each vibrational level. The vibrational energy distributions for the two H_2 elimination channels are shown in Figure 6 along with the total distribution from Figure 2. The percent compositions of the vibrational levels is given in Table I.

For the v"=0 and v"=1 levels the rotational temperature of H_2 product from reaction (3) is known from the deuterated ethylene study. The contribution to the population distribution for those vibrational levels from the 1,1 elimination channel was calculated from the measured temperatures and the percent of total population of that level derived above. The rotational distribution of H_2 product from the 1,2 elimination channel, reaction (4), for the v"=0 and v"=1 levels was then estimated by making a non-linear least squared fit to the difference between the total H_2 distribution and the calculated reaction (3) distribution. The measured and calculated rotational distributions for the v"=0 and v"=1 levels are shown in Figures 7 and 8 respectively. The rotational temperatures are given in Table I.

For the v"=2 and v"=3 levels the rotational distributions were not measured for H_2 from reaction (3). The total rotational distributions for these two vibrational levels were fit by varying the temperatures of the distributions from the two channels while minimizing the standard deviation of the fit from the measured

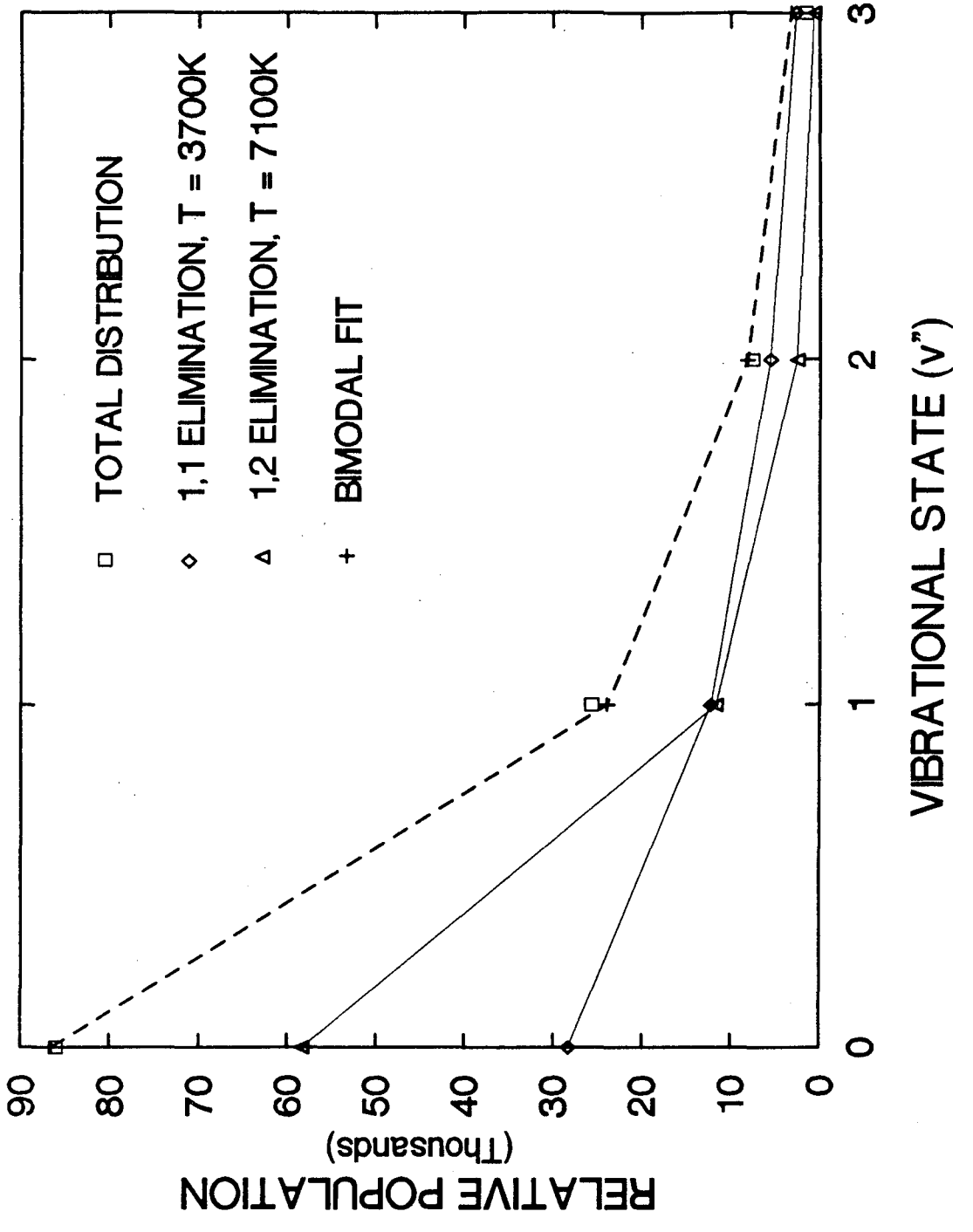

Figure 6. Calculated bimodal distribution fit to the vibrational energy distribution in H_2 from the dissociation of C_2H_4. (□)=measured H_2 distribution, (△)=calculated distribution for reaction (3), (◇)=calculated distribution for reaction (4), (+)=bimodal fit (sum of (3) and (4)).

distributions within the constraints of the relative populations given in Table I. The rotational temperatures for the distributions from reaction (3) were estimated at 1200K and 600K respectively. The best fit rotational temperatures for the distributions from reaction (4) are 4000K and 2700K respectively. The results of these calculations are shown in Figures 9 and 10 respectively and the measured temperatures are given in Table I.

TABLE I: BIMODAL FIT PARAMETERS TO THE H_2 ROTATIONAL DISTRIBUTIONS

VIBRATIONAL STATE	% 1,1 ELIMINATION	$T_R(1,1)$ (K)	$T_R(1,2)$ (K)
0	67	2500 ± 200	3500 ± 940
1	49	2000 ± 160	4200 ± 800
2	32	1200	4000 ± 1200
3	19	600	2700 ± 350

The measured H_2 rotational distributions from the dissociation of 1,1-d_2 ethylene, which eliminates H_2 only by reaction (3), clearly show that the amount of energy imparted into H_2 rotation in this channel is less than the total amount of rotational energy measured in the H_2 product from the dissociation of C_2H_4 for the v"=0 and v"=1 vibrational levels. The rotational energy imparted also decreases significantly from v"=0 to v"=1 which supports the

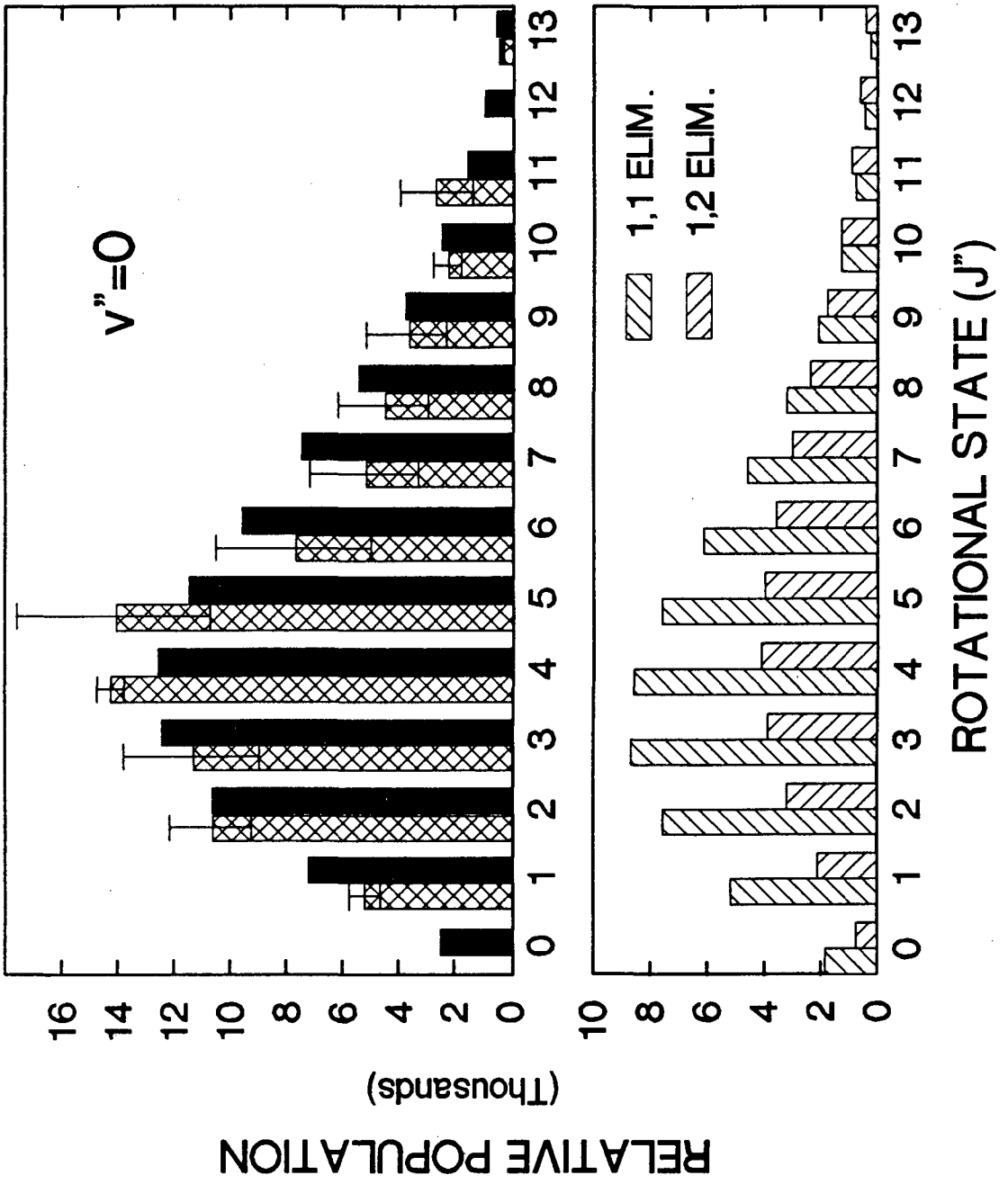

Figure 7. (Top): Bimodal fit to the H_2 rotational distribution for v"=0 (solid bars) shown with the measured distribution from Figure 3 (hatched bars). (Bottom): Calculated rotational distributions for reactions (3) and (4) used to generate the bimodal fit.

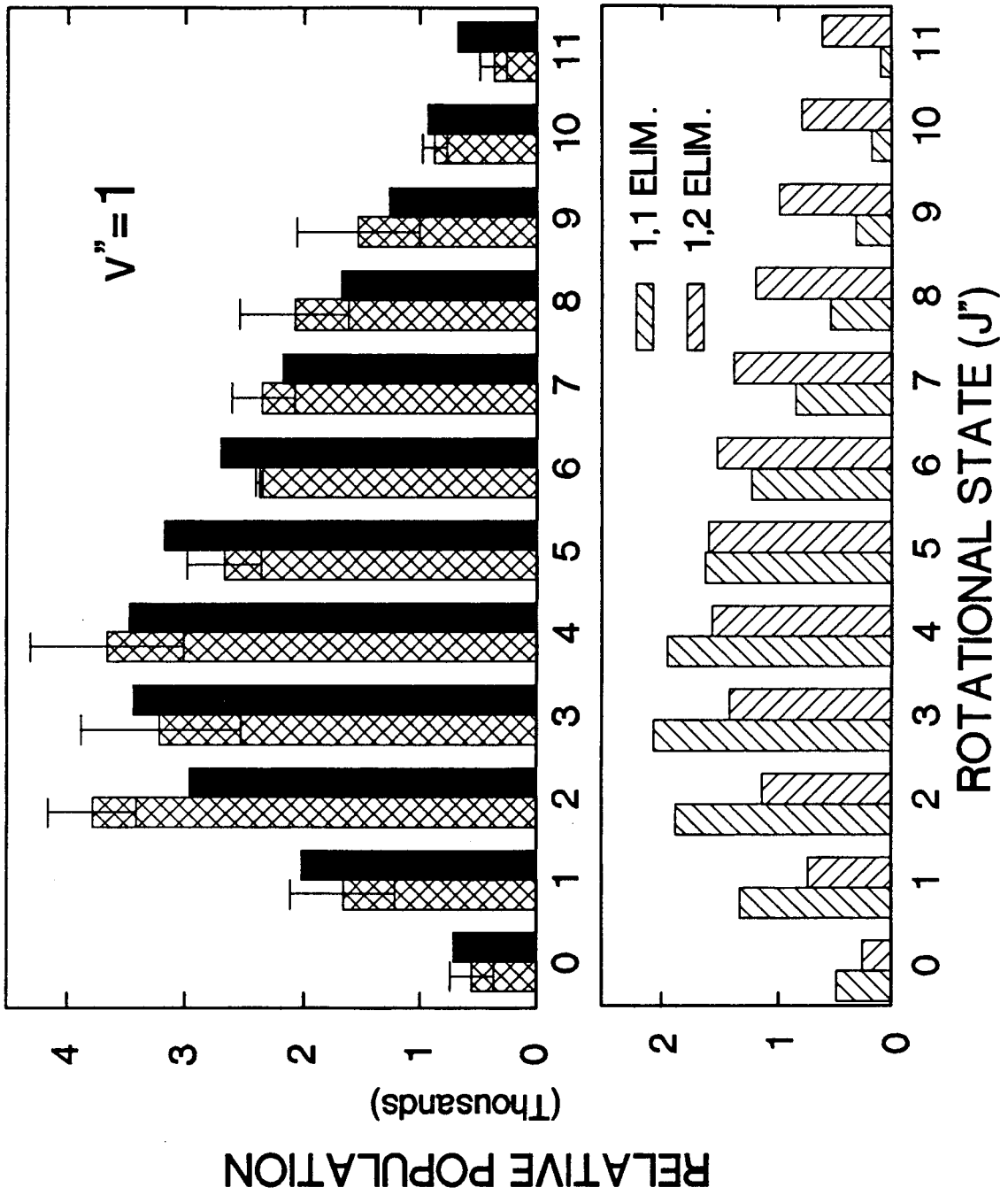

Figure 8. (Top): Bimodal fit to the H_2 rotational distribution for v"=1 (solid bars) shown with the measured distribution from Figure 3 (hatched bars). (Bottom): Calculated rotational distributions for reactions (3) and (4) used to generate the bimodal fit.

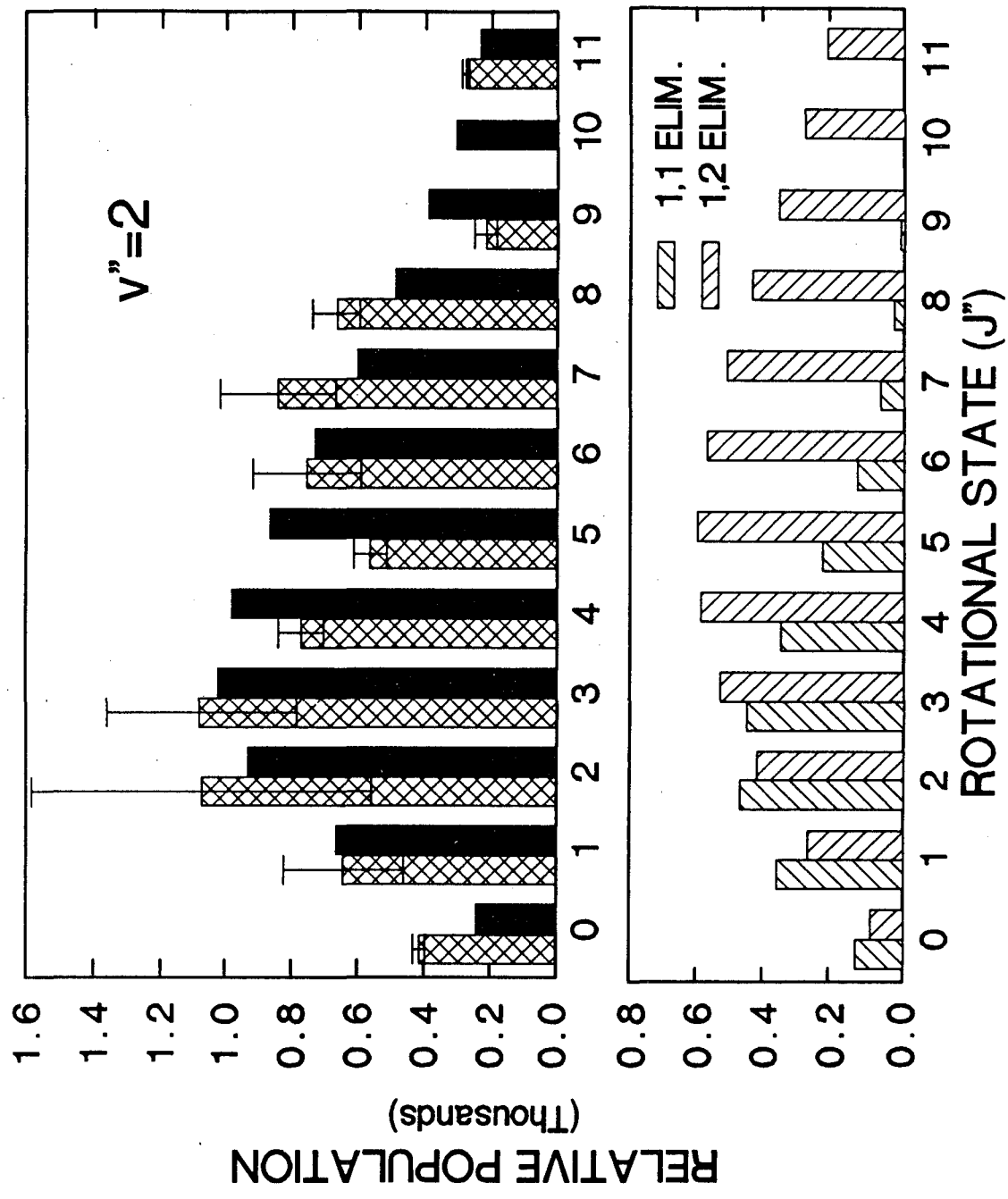

Figure 9. (Top): Bimodal fit to the H_2 rotational distribution for v"=2 (solid bars) shown with the measured distribution from Figure 3 (hatched bars). (Bottom): Calculated rotational distributions for reactions (3) and (4) used to generate the bimodal fit.

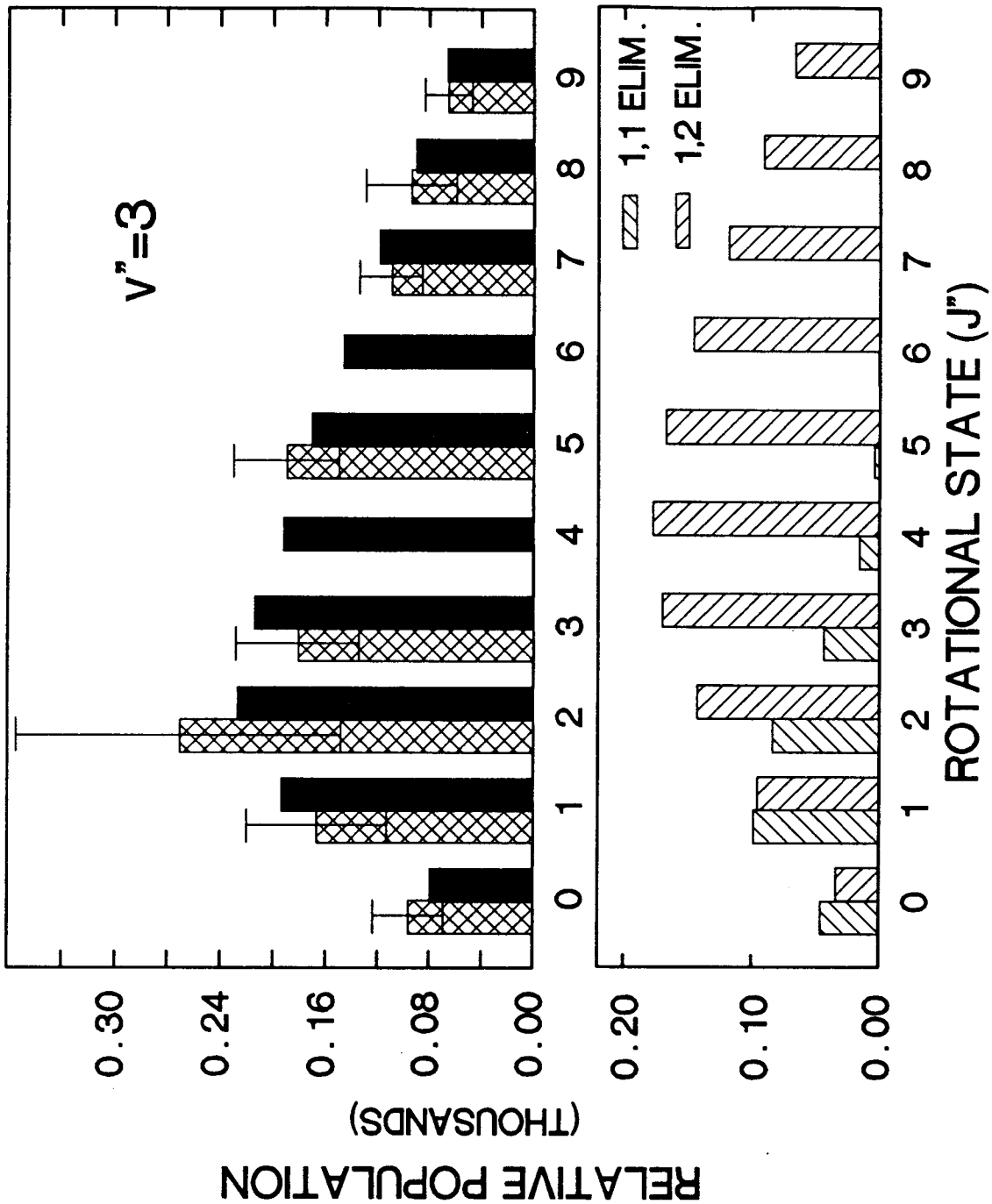

Figure 10. (Top): Bimodal fit to the H_2 rotational distribution for v"=3 (solid bars) shown with the measured distribution from Figure 3 (hatched bars). (Bottom): Calculated rotational distributions for reactions (3) and (4) used to generate the bimodal fit.

lower rotational temperatures measured for this channel in the v"=2 and v"=3 levels.

The repulsive energy release determines the translational and rotational energies of the H_2 product. If the repulsive energy release depends on the vibrational coordinate of H_2 then it is understandable that higher v" levels, with a corresponding larger H-H distance, will have smaller repulsion and hence exhibit smaller rotational excitation. In addition, one should see some correlation between the rotational and translational energy of H_2, unless one dominates over the other. Energetically, one can also understand the decrease in rotational energy by considering that for v"=3 the H_2 vibrational energy is 33.6kcal/mole. This leaves much less energy available for H_2 rotation and translation at this level then at the lower vibrational levels.

The transition state for the 1,1 elimination channel should be similar to that for H_2 elimination from formaldehyde. H_2 rotational distributions for this reaction have been measured at a number of different excitation energies.[26] There are significant differences between the two reactions: formaldehyde excitation is resonant and dissociation occurs on the ground electronic state potential surface while it is not known whether or not the ethylene dissociation is an excited or ground state process. None the less, the total amount of energy available to the H_2

products is close (≈86kcal/mole for H_2CO) so a comparison is worthwhile. The rotational temperatures measured by Butenhoff et. al. for H_2 dissociated from H_2CO are 1730K for the v"=1 level and 1240K for the v"=3 level. The amount of rotational energy imparted to H_2 in the two different dissociative processes is comparable as are the initial geometries. Thus, the position of the H atoms at the critical configuration in the transition state region and the anisotropy in the repulsion of those H atoms must also be comparable.

The main difference between the 3-centered H_2 elimination channel and the 4-centered elimination channel in the dissociation of ethylene is the amount of energy available to the H_2 product. As mentioned above, the 4-centered channel has ≈106kcal/mole of energy available to products. This makes twice as much energy available to the H_2 formed as the other channel. One of the results of this is that the H_2 rotational energy should be much higher. While there is a fair amount of uncertainty in the measurements and the analysis (especially for the v"=0 and v"=2 levels) it is clear that there is a large component of highly rotationally excited H_2 in the rotational distributions that cannot be fit by the 1,1 elimination channel. This component can be accounted for by H_2 coming from reaction (4). This is confirmed by the temperatures measured for this channel in the bimodal fit to the

rotational distributions.

There are geometrical reasons to expect the 1,2 elimination channel to cause a higher degree of rotational excitation in the H_2 product. In the ground state of C_2H_4 the distance between the two H-atoms attached to the same carbon center is ≈1.8Å while for two H-atoms on different carbons the distance is ≈2.5Å. In the excited electronic state this discrepancy increases due to a lengthening of the C=C bond distance. An increase in the H-H distance can account for higher vibrational excitation but cannot solely account for higher rotational excitation. For rotational excitation to occur there must be an anisotropy in the potential energy surface in the exit channel of the reaction.

There are two arguments for a large amount of anisotropy to be present in the 1,2 elimination exit channel. The first is connected to the configuration of C_2H_4 in its first electronic excited state. In the V state an electron is promoted from a bonding orbital in the double bond to an anti-bonding orbital. A consequence of this is that the methylene groups twist 90° with respect to one another.[21] It has also been shown that the torsion motion about the C-C bond is excited by 193nm radiation.[27] While direct coupling from this motion to H_2 rotation should be small the position of the 1 and 2 H atoms, and any symmetry at the transition state for H_2 elimination, would be greatly

affected by this motion. Anisotropic repulsion of the H's is most likely coming from differences in the C-H bond lengths. The H-H distance must be short in order to reach the transition state because of the need for significant overlap between the electronic orbitals associated with those H's before bonding can occur. Apparently, one of the H's in the 1,2 elimination is moving over towards the neighboring carbon and elongating its C-H bond. The size of this movement is accentuated by the C_2H_4 structure discussed above leading to larger anisotropy in the repulsive energy release.

The role of ethylidene (CH_3CH) must also be considered in this reaction. As the 1 and 2 hydrogens move about between the two carbon atoms one might consider ethylidene to be a limiting case of this movement where both H-atoms are located next to a single carbon atom. While at certain energies ethylidene might be a stable structure the energy imparted by the 193nm photon to the C_2H_4 molecule will certainly be above any barrier to isomerization between C_2H_4 and CH_3CH. It does not seem likely that if the second H_2 elimination channel involved CH_3CH as an intermediate that one would observe as much rotational and vibrational excitation as is indicated by the measurements reported here. However, a transition state structure with one hydrogen atom "rocking" over towards the other carbon atom in a position somewhere between C_2H_4 and CH_3CH is entirely

consistent with the data presented here. This structure would cause a large anisotropy in the repulsion between the two leaving H atoms and the "acetylene" fragment, in a similar fashion as discussed above, leading to high rotational excitation.

B. AVERAGE TRANSLATIONAL ENERGY

The average H_2 velocity associated with each quantum state was calculated from the Doppler shifts fit to the individual line shapes by the procedure described above. From these velocities the average H_2 translational energy ($E_{tr}=\frac{1}{2}mv^2$) was calculated. A plot of E_{tr} for H_2 versus the internal energy of the molecule is shown in Figure 11 along with a linear least squares fit to the data. Only those transitions which exhibited no interference from other nearby lines were used in this analysis.

As can be seen, the amount of translational energy the H_2 fragment gains when it is repelled away from the transition state configuration decreases as its internal energy increases. This is expected because as the amount of energy in rotational and vibration motions gets larger there is less energy available for the translational degree of freedom. However, there is not a one-to-one correspondence between translational and internal energy. This indicates, as in the case of 1,4-cyclohexadiene discussed in the

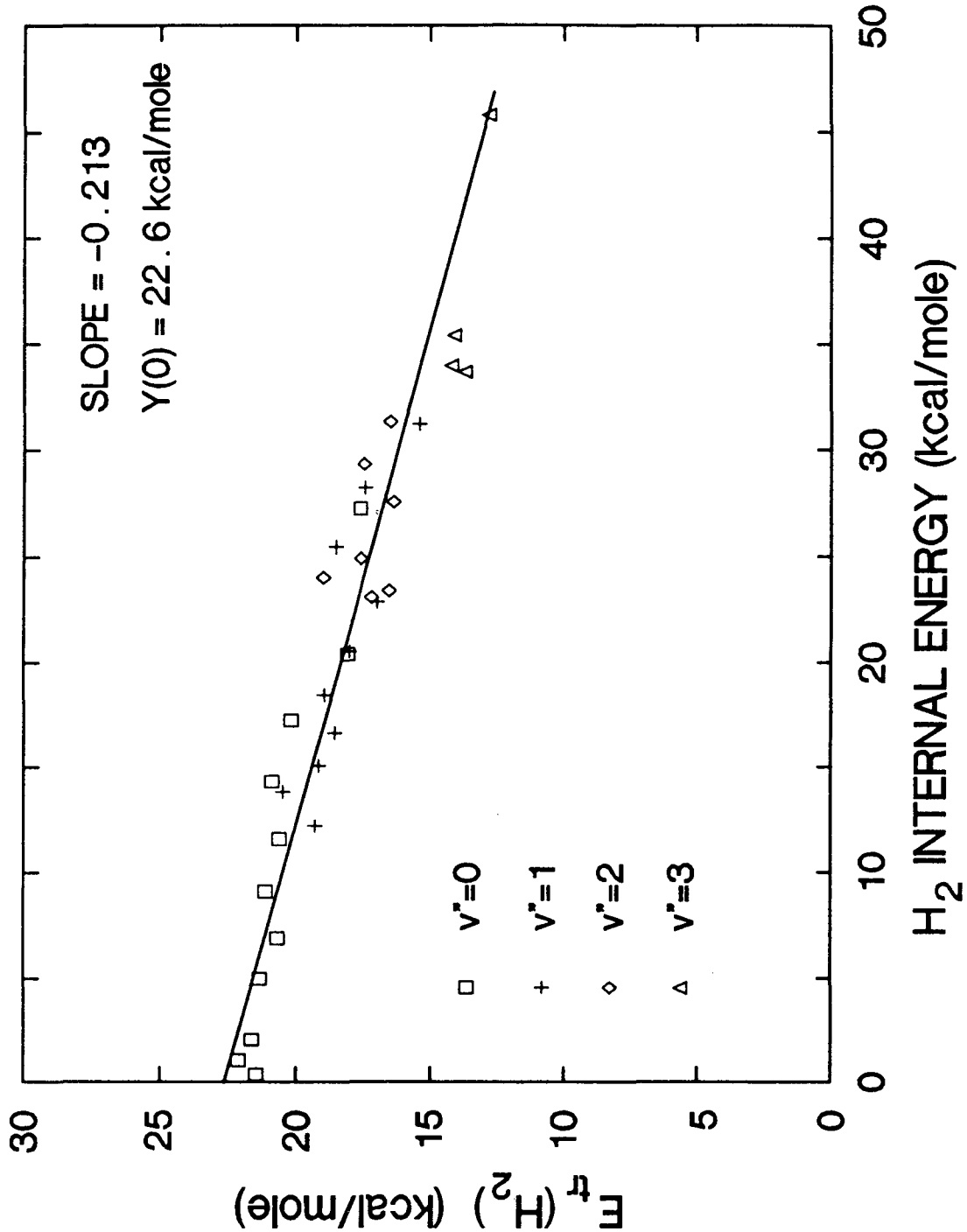

Figure 11. Plot of translational energy versus internal energy for H_2 product from the dissociation of C_2H_4. The various vibrational quantum states of the H_2 product are indicated.

previous chapter, that the amount of translational energy imparted into the H_2 is dominated by the repulsive nature of the closely placed product molecules at the critical configuration in the transition state region and the repulsive energy release could depend significantly on the H-H coordinates.

The H_2 translation energy falls off faster with increasing internal energy in the case of C_2H_4 than in the case of 1,4-CHDN. The reason for this stems from the fact that there are many fewer degrees of freedom in the ethylene molecule. Product translation energy can be gained from potential energy, as mentioned above, and from motion along the reaction coordinate which is coupled into the product molecules. The energy per mode will be much higher in C_2H_4 than in 1,4-CHDN (because of the fewer degrees of freedom) so this secondary effect will play a more important role in the dissociation of C_2H_4. As the H_2 internal energy increases the excess energy along the reaction coordinate will decrease and lower the amount of energy coupled into translation motion.

It is also instructive to analyze the amount of H_2 translational energy as a function of rotational energy. The distribution of translational energies plotted this way for the vibrational levels v"=0 to v"=3 is shown in Figure 12. For each vibrational level the translational energy decreases with increasing rotational energy, as expected,

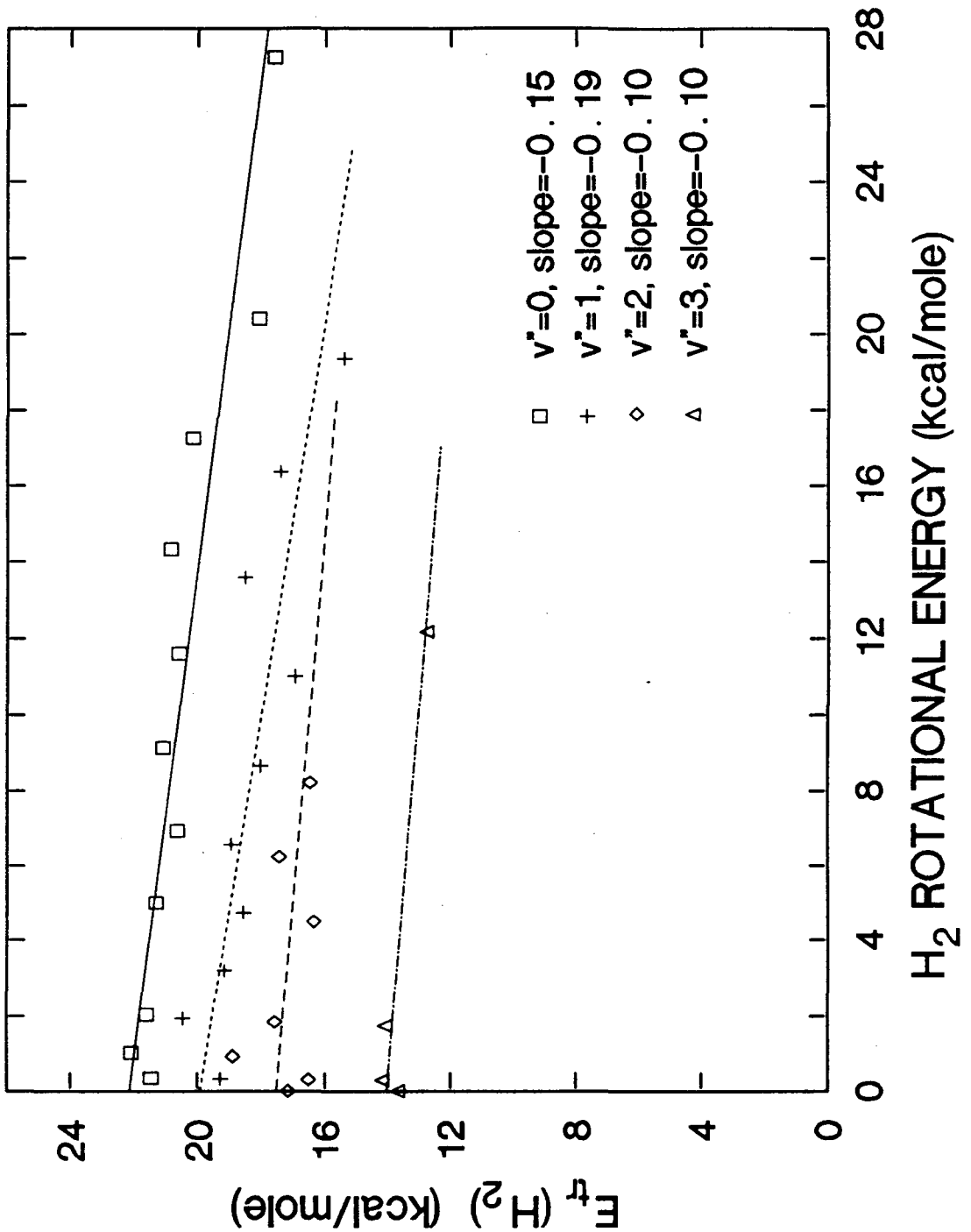

Figure 12. Plot of translation energy versus rotational energy for the vibrational levels v"=0 (□), v"=1 (+), v"=2 (◇), and v"=3 (△) for H_2 product from the dissociation of C_2H_4. The various lines represent linear least squares fits to each vibrational level with the indicated slopes.

confirming the existence of a correlation between H_2 rotational and translational energy. The behavior of each v" level is somewhat linear. Deviations from linearity are most likely an effect of the presence of two H_2 elimination channels which complicates any analysis. In order to get a sense of the magnitude of the rotational-translational correlation for each vibrational level least squares fits were made to the data points. These fits, with their indicated slopes, are shown in Figure 12.

If one considers two H_2 elimination channels with equal repulsive anisotropy then if more translational energy is released in one of those channels more rotational excitation will also be realized. One way to tell if greater rotational energy is due to higher released energy or larger anisotropy is to observe the correlation between rotation and translation. If the anisotropy is the dominating factor, namely the repulsion is mainly between individual C and H atoms, there should be less correlation and conversely if potential energy release dominates, namely repulsion is between H_2 and the remaining part of the molecule, then there should be a larger degree of correlation. Clearly, the correlation between H_2 rotational and translational energy is not very strong with the translational energy only decreasing ≈1/10th as much as the rotational energy increases. Therefore, anisotropic repulsion of the eliminating H's is the dominating factor in determining the

amount of rotational excitation of the H_2 product in the dissociation of C_2H_4.

The H_2 translational energy decreases more than twice as fast with increasing vibrational energy than with increasing rotational energy. A reason for this, as mentioned previously when discussing the correlation between vibrational and rotational energy, is that the H-H coordinates in the transition state leading to vibrationally excited H_2 place the product molecules farther apart and lower the amount of potential energy release. Furthermore, H_2 rotational energy falls off faster with increasing vibrational levels than translational energy ($E_R(v''=3) \approx 0.2 * E_R(v''=0)$, $E_T(v''=3) \approx 0.6 * E_T(v''=0)$ for 1,1 elimination). This suggests that anisotropy in the repulsive potential is less when the H-H bond is longer.

In addition to the full Doppler profiles an attempt was made to measure the maximum amount of translational energy imparted into the H_2 product. The maximum available energy for translation occurs for H_2 formed in the v"=0, J"=0 quantum state. With this in mind the wings of the H_2 C-X (1,0) R(0) transition were scanned at high signal gain and the fastest H_2 product was measured. This scan is shown in Figure 13. The component in the scan due to background H_2 gas in the vacuum chamber has been subtracted from the trace in Figure 13. The maximum Doppler shift of this component was significantly less than that of the product H_2

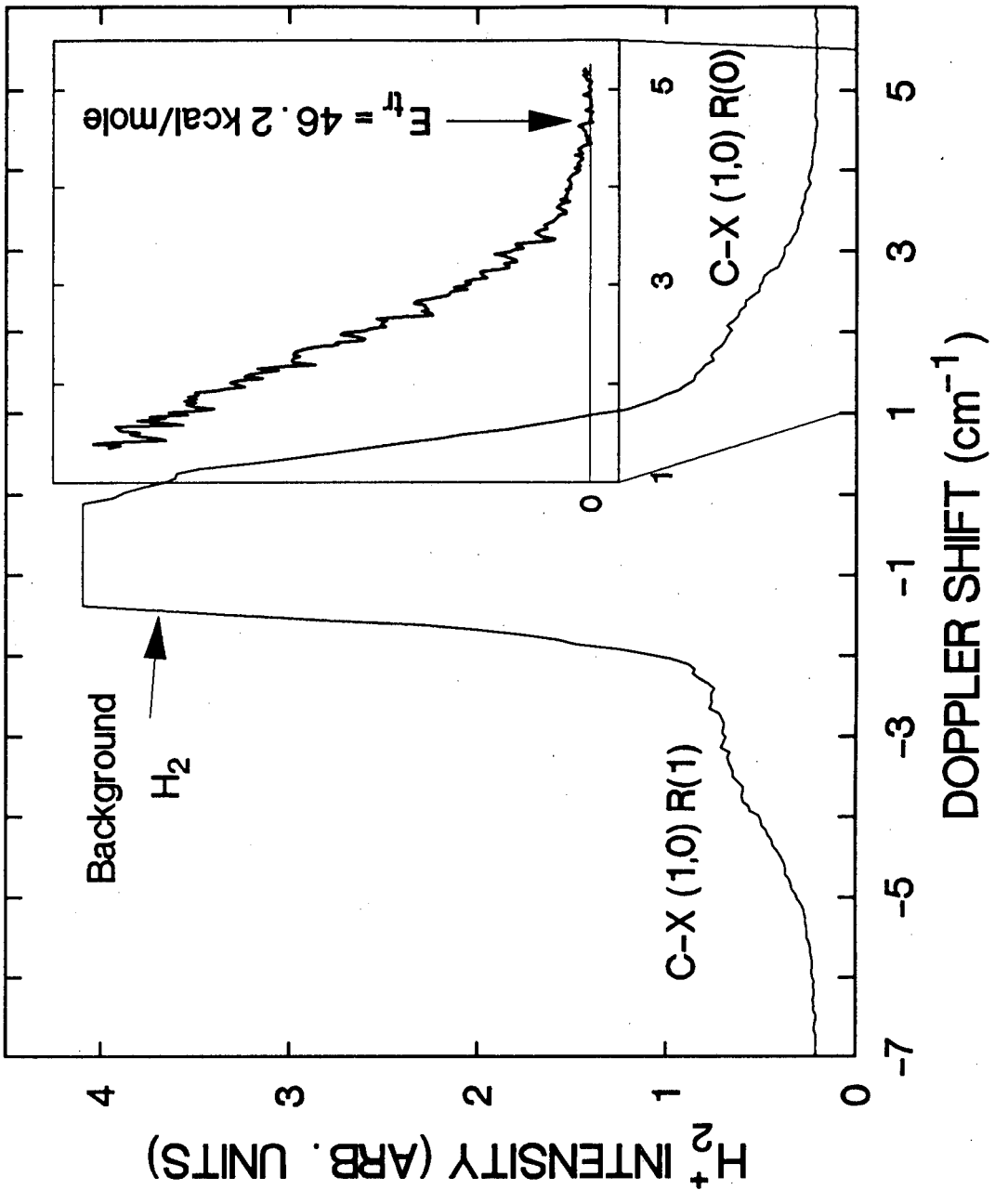

Figure 13. H_2 C←X (1,0) R(1) (ν_0=101455.8cm^{-1}) and C←X (1,0) R(0) (ν_0=101457.6cm^{-1}) transitions showing enhanced scan of the blue edge of the R(0) line. The position of maximum H_2 translational energy is indicated. The saturated features at the line centers are due to background H_2 gas in the chamber. The Doppler shift is relative to the R(0) transition center frequency.

molecules. The maximum H_2 translation energy that was observed was $E_{tr}(H_2)$=46.2kcal/mole. The corresponding translation energy of the acetylene molecule is $E_{tr}(C_2H_2)$=3.55kcal/mole which means only ≈50kcal/mole of energy is imparted into product translation.

A possible explanation of this seemingly low maximum translational energy can be found in the relative importance of the two reaction channels in forming H_2 in the v"=0, J"=0 quantum state. From the distributions derived above the 1,1 elimination channel dominates the population in this state by almost 3:1. Thus, the amount of product from the 1,2 channel that is Doppler shifted to the frequency region in question might be below the detection limit of the experiment. If the E_{tr} value above represents the maximum energy released in reaction (3) then it puts an upper limit on the heat of formation of vinylidene. Theoretical values for this heat of formation are around 100kcal/mole. In this experiment it is measured to be <110.8kcal/mole.

C. H_2 VELOCITY DISTRIBUTION

One of the interests of this experiment was to determine if a difference in translational energy of the H_2 product from the two elimination channels of C_2H_4 could be measured. Although the distribution of the H_2 energies by quantum state suggests a bimodal distribution there is no

clear evidence of this in the Doppler profiles themselves even though the instrument resolution was $<0.06cm^{-1}$. The technique of velocity aligned Doppler Spectroscopy (VADS) first noted by Wittig[28] was used to improve the translational energy resolution of the experiment. The results of these experiments will be described below.

In a "normal" Doppler profile one measures not only species directed towards and away from the probe beam but also those molecules that are directed perpendicular to the probe beam. The resulting profile is a filled in lineshape with the resolution of the product velocity degraded by the angular distribution of that product. In VADS, a long time delay is introduced between the formation of the product and its measurement. In addition, the diameter of the probe and photolysis beams are kept as small as possible. Under these conditions any product with a velocity component directed perpendicular to the probe beam will have moved out of the region that is interrogated by the probe beam during the time between when the photolysis and probe beams are fired. This effectively discriminates against those molecules so the only product molecules that are detected are those directed at or away from the probe beam. The product velocity resolution of the experiment is then greatly enhanced and one can obtain a true speed distribution of the product. A diagram showing this effect is given in Figure 14.

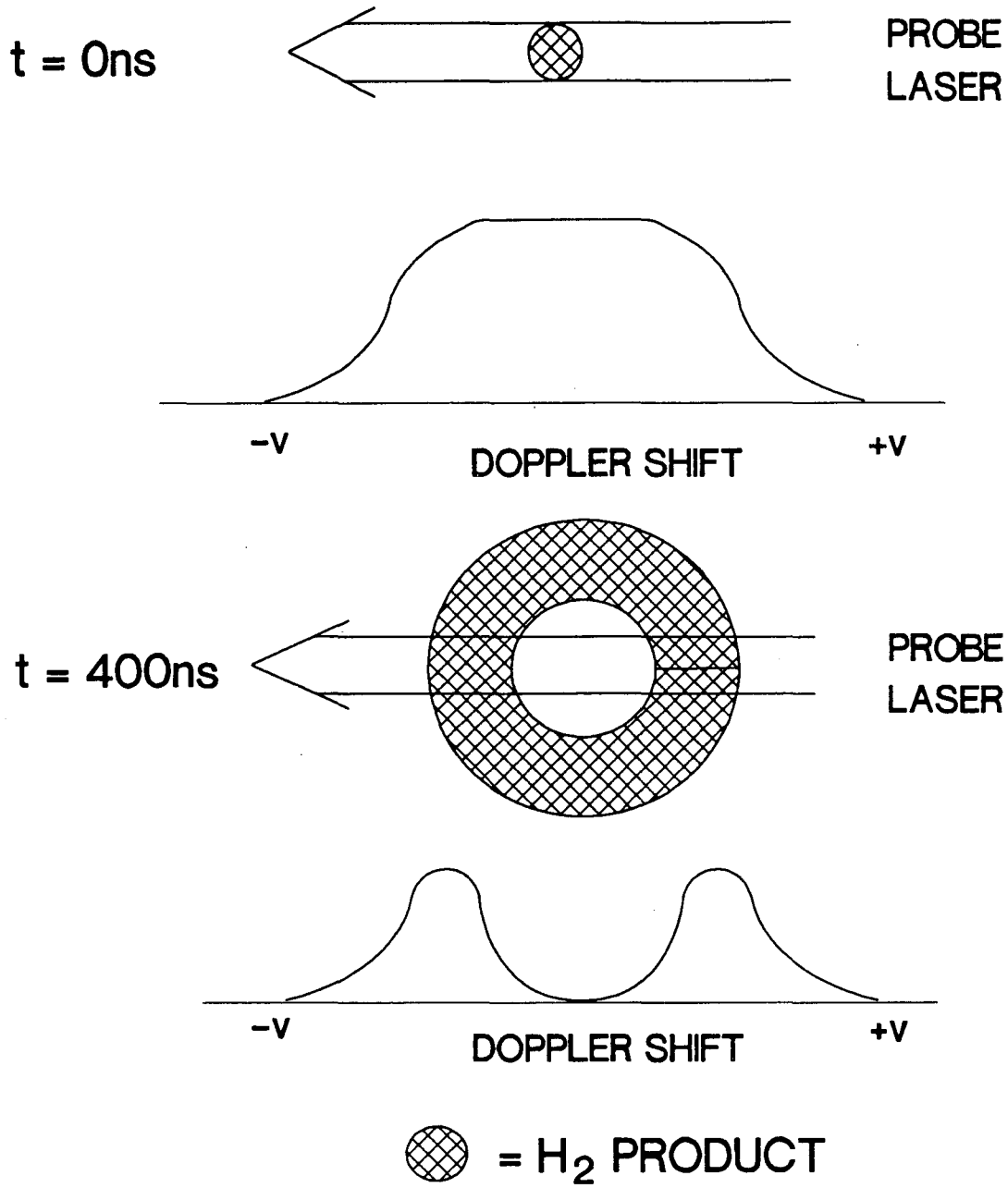

Figure 14. Pictorial representation of the time delay effect used in Velocity Aligned Doppler Spectroscopy (VADS). Shown are (Top) probe beam/H_2 product overlap and expected line profile at zero time delay and (Bottom) probe beam/H_2 product overlap and expected line profile at a long time delay (400ns). The cross hatched areas represent the spatial distribution of the H_2 dissociated from C_2H_4.

A number of transitions for the v"=1 and v"=2 levels were measured under long time delay, or VADS, conditions. Those transitions which exhibited no interference from other lines and had large signals (the signal is significantly reduced under the VADS conditions) produced the best results. The delay between the photolysis and probe lasers needed to observe a VADS profile was dependent on the experimental parameters. The most critical of these was the size of the photolysis beam in the interaction region. The timing varied between 100ns for a small photolysis beam to 400ns for a larger beam. The delay was set at the point where no further depletion in signal at the line center could be observed.

For the v"=1 level the following H_2 transitions were observed under VADS conditions: B-X (1,1) R(1), B-X (2,1) P(3), and B-X (2,1) R(5). These VADS profiles along with the corresponding line shapes measured under normal conditions are shown in Figure 15. For the v"=2 VADS profiles were measured for the following transitions: B-X (2,2) R(0), B-X (2,2) R(1), and B-X (3,2) P(5). These transitions are shown in the same manner in Figure 16. For each profile the peak Doppler shift and FWHM of the H_2 velocity distribution was measured. These values are given in Table II.

Figure 15. H_2 Doppler profiles measured under VADS conditions for the v"=1 level. (Top): H_2 B←X (2,1) R(5) transition (ν_0=87710.0cm^{-1}). (Middle): H_2 B←X (2,1) P(3) transition (ν_0=88077.1cm^{-1}). (Bottom): H_2 B←X (1,1) R(1) transition (ν_0=87358.2cm^{-1}). The VADS profiles are shown with a heavy line while the normal Doppler profiles are shown with a light line. The intensity scales are not related.

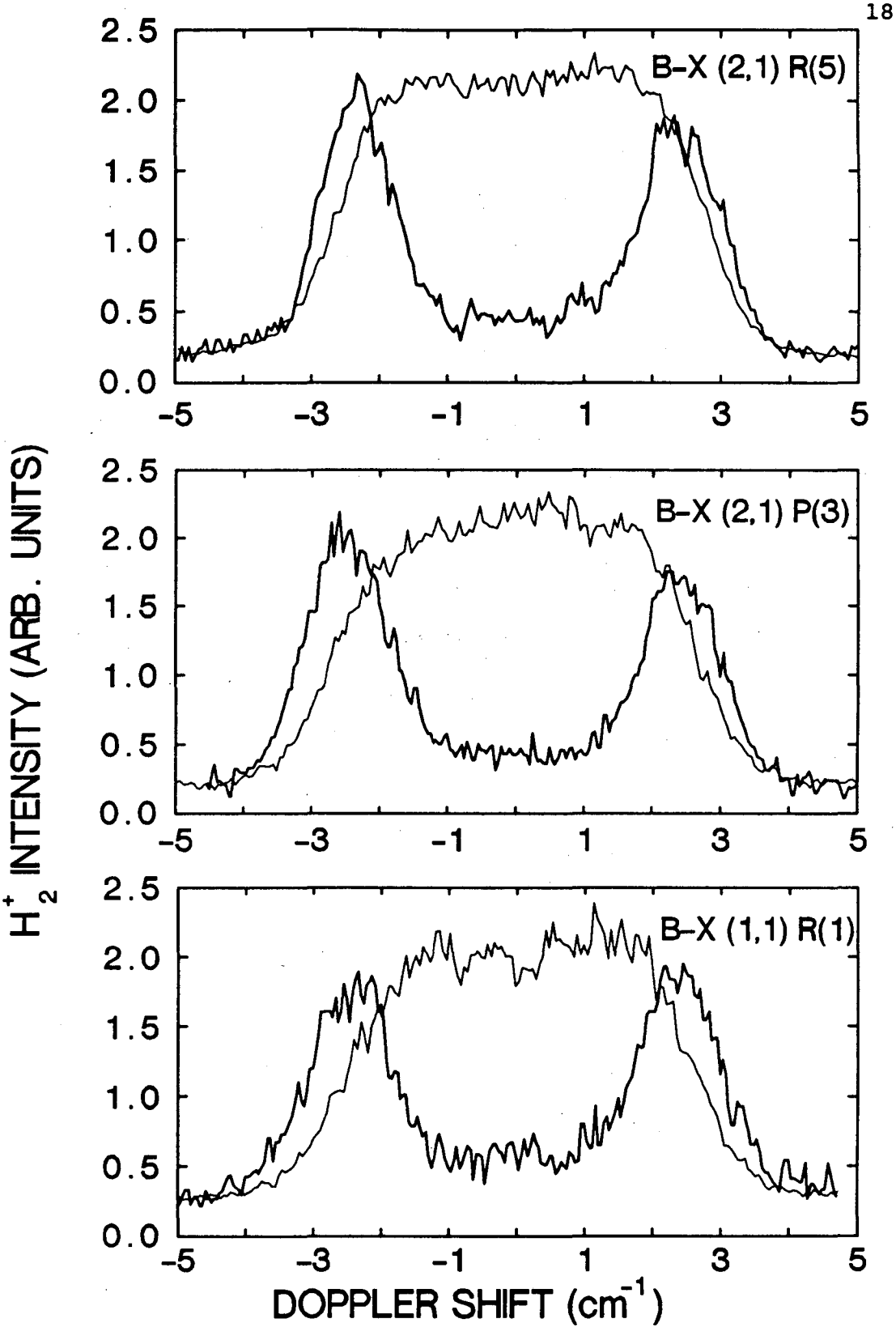
B–X (2,1) R(5)
B–X (2,1) P(3)
B–X (1,1) R(1)
2.5
2.0
1.5
1.0
0.5
0.0
-5
-3
-1
1
3
5
H_2^+ INTENSITY (ARB. UNITS)
DOPPLER SHIFT (cm^{-1})

Figure 15

Figure 16. H_2 Doppler profiles measured under VADS conditions for the v"=2 level. (Top): H_2 B←X (3,2) P(5) transition (ν_0=84729.8cm^{-1}). (Middle): H_2 B←X (2,2) R(1) transition (ν_0=84714.9cm^{-1}). (Bottom): H_2 B←X (2,2) R(0) transition (ν_0=84751.3cm^{-1}) (only the red-shifted peak was measured for the R(0) transition). The VADS profiles are shown with a heavy line while the normal Doppler profiles are shown with a light line. The intensity scales are not related.

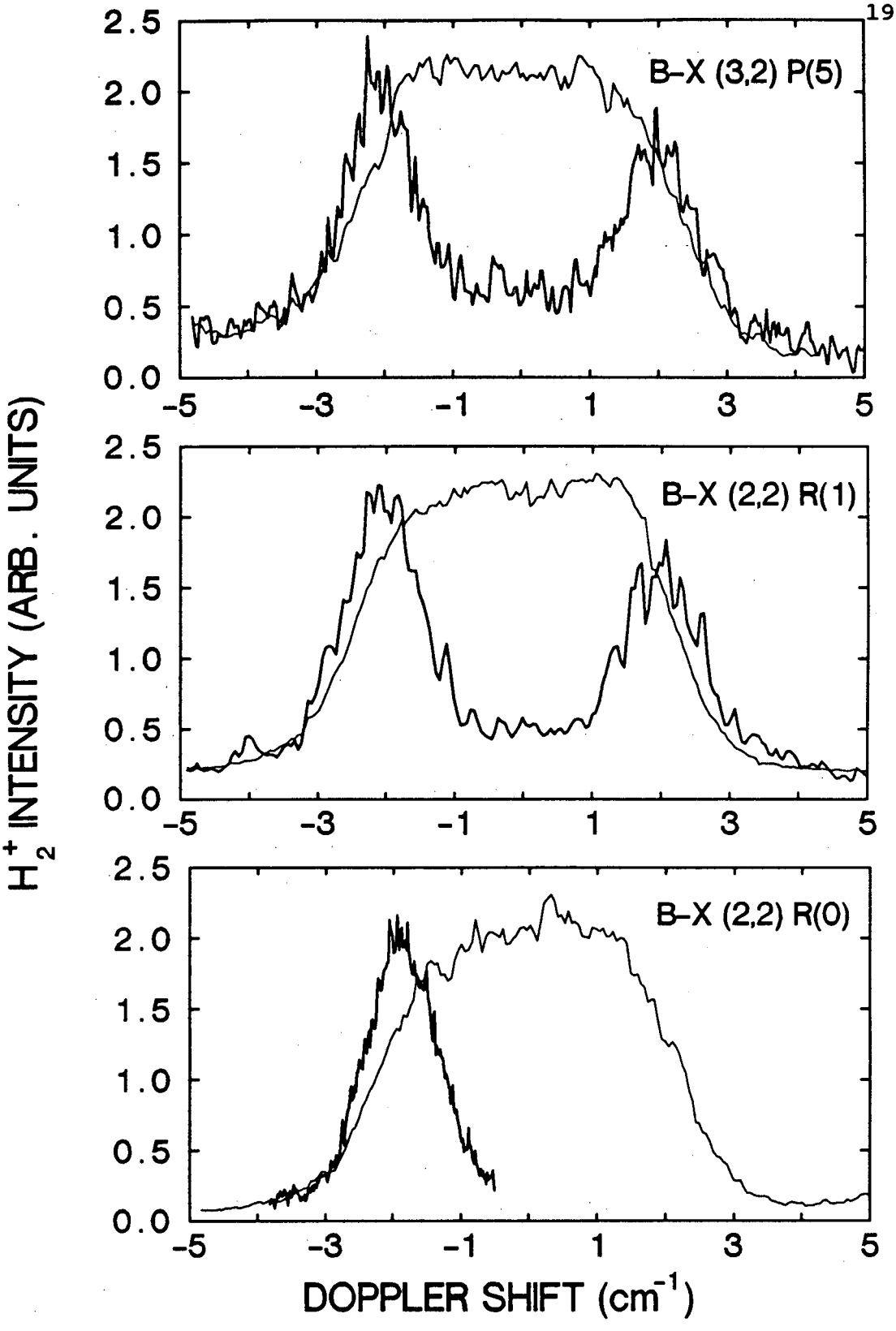
B–X (3,2) P(5)
B–X (2,2) R(1)
B–X (2,2) R(0)
H_2^+ INTENSITY (ARB. UNITS)
DOPPLER SHIFT (cm^{-1})
2.5
2.0
1.5
1.0
0.5
0.0
-5
-3
-1
1
3
5

Figure 16

TABLE II: H_2 DOPPLER SHIFT DISTRIBUTIONS AS MEASURED BY VADS				
H_2 TRANSITION	V(0) (cm^{-1})	PEAK V_D (cm^{-1})	FWHM (cm^{-1})	PEAK E_{tr} (kcal/mole)
B-X(1,1)R(1)	87358.22	2.35	1.44	15.6
B-X(2,1)P(3)	88077.07	2.45	1.38	16.6
B-X(2,1)R(5)	87709.96	2.37	1.44	15.7
B-X(2,2)R(0)	84751.31	1.96	1.14	11.5
B-X(2,2)R(1)	84714.90	2.06	1.27	12.7
B-X(3,2)P(5)	84729.84	2.05	1.30	12.5

A comparison of the peak H_2 translational energies, as measured by VADS, and the average E_{tr} energies calculated from the fits to the normal Doppler profiles reveals that the VADS values are lower. The following explanation is given for this observation. When scanning a transition under VADS conditions there is a $1/v^2$ intensity weighting that results from the fact that for faster product one samples a smaller solid angle from any given photolysis volume element. This will tend to make the VADS profile peak at a lower Doppler shift than a normal Doppler profile. The full analysis of a VADS profile is given by Xu et. al.[29] and includes the above effect as well as the initial product distribution, probe beam geometry, product velocity, photolysis/probe time delay and smaller effects due to parent motion and probe laser bandwidth.

The H_2 speed distributions were examined more carefully by scanning the red-shifted H_2 peaks in the VADS profiles at higher resolution. Scans of red-shifted H_2 under VADS conditions for the v"=1 states are shown in Figure 17 while those of the v"=2 states are shown in Figure 18.

Within a given H_2 vibrational level the profiles shown in Figures 17 and 18 do not change noticeably. However, differences can be observed between the H_2 velocity distributions for the v"=1 and v"=2 levels. For v"=1 the fast H_2 edge is much sharper and the slower H_2 portion tails off more gradually than for v"=2. A further study of the red-shifted peak of the B-X (2,2) R(1) transition at an even longer time delay (700ns) seems to reveal a bimodal distribution. This scan, along with the 400ns time delay scan for this transition from Figure 18, is shown in Figure 19.

It appears that there is a slower and more narrow H_2 speed distribution on top of a broader H_2 distribution which extends out to much larger Doppler shifts. This broader component extends out to an $\approx 3.9 cm^{-1}$ shift which corresponds to a H_2 translational energy of 46kcal/mole. Given the internal energy of H_2 in this state (23kcal/mole) and the energetics of the reaction (Figure 5) this component of the Doppler profile must be from reaction (4), the 1,2 elimination process. These profiles yield considerable information on the spread of internal energies found in the

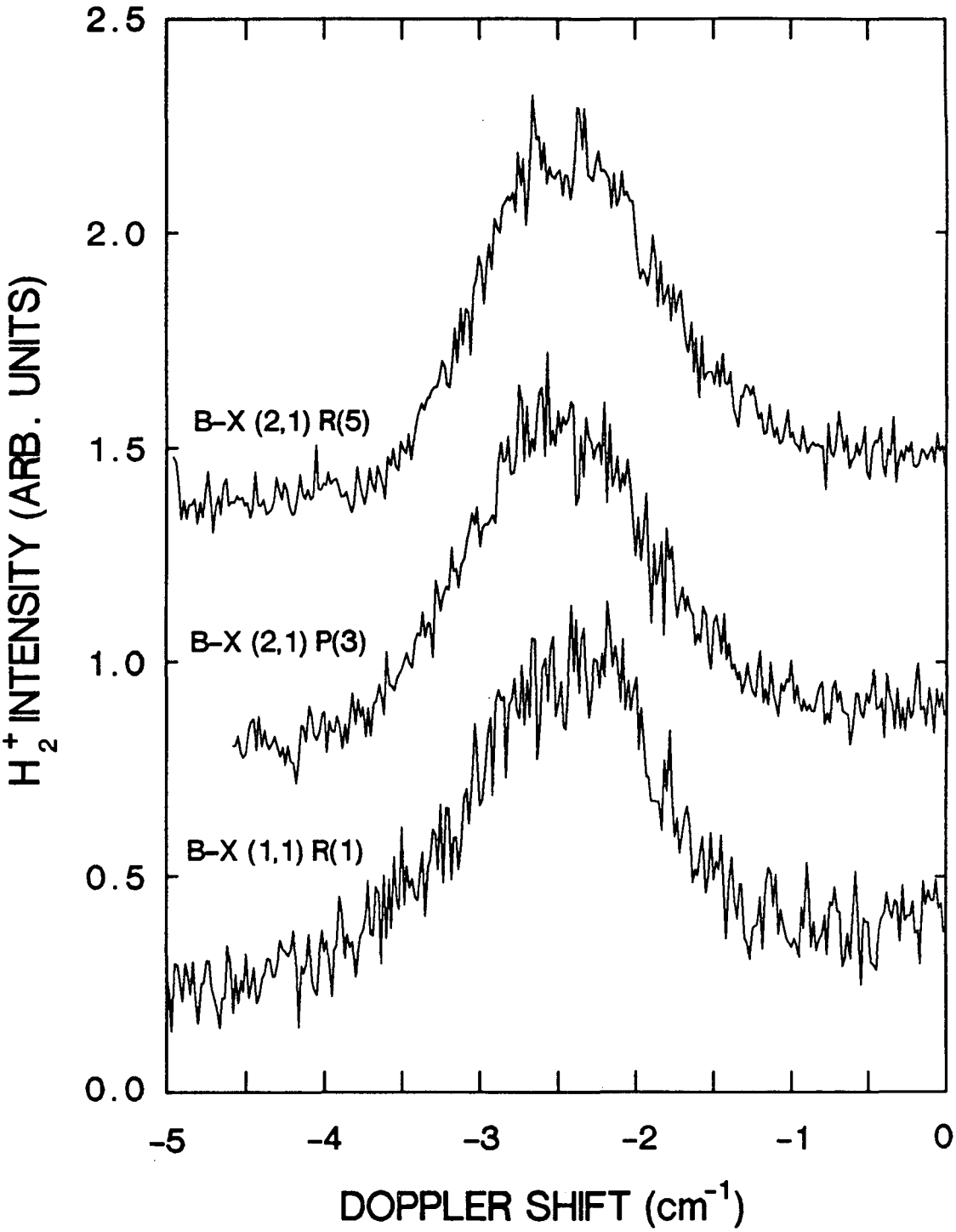

Figure 17. High resolution scans measured under VADS conditions of the red-shifted H_2 peaks for the v"=1 transitions shown in Figure 15. The step size for these scans is 250MHz. The different transitions are indicated.

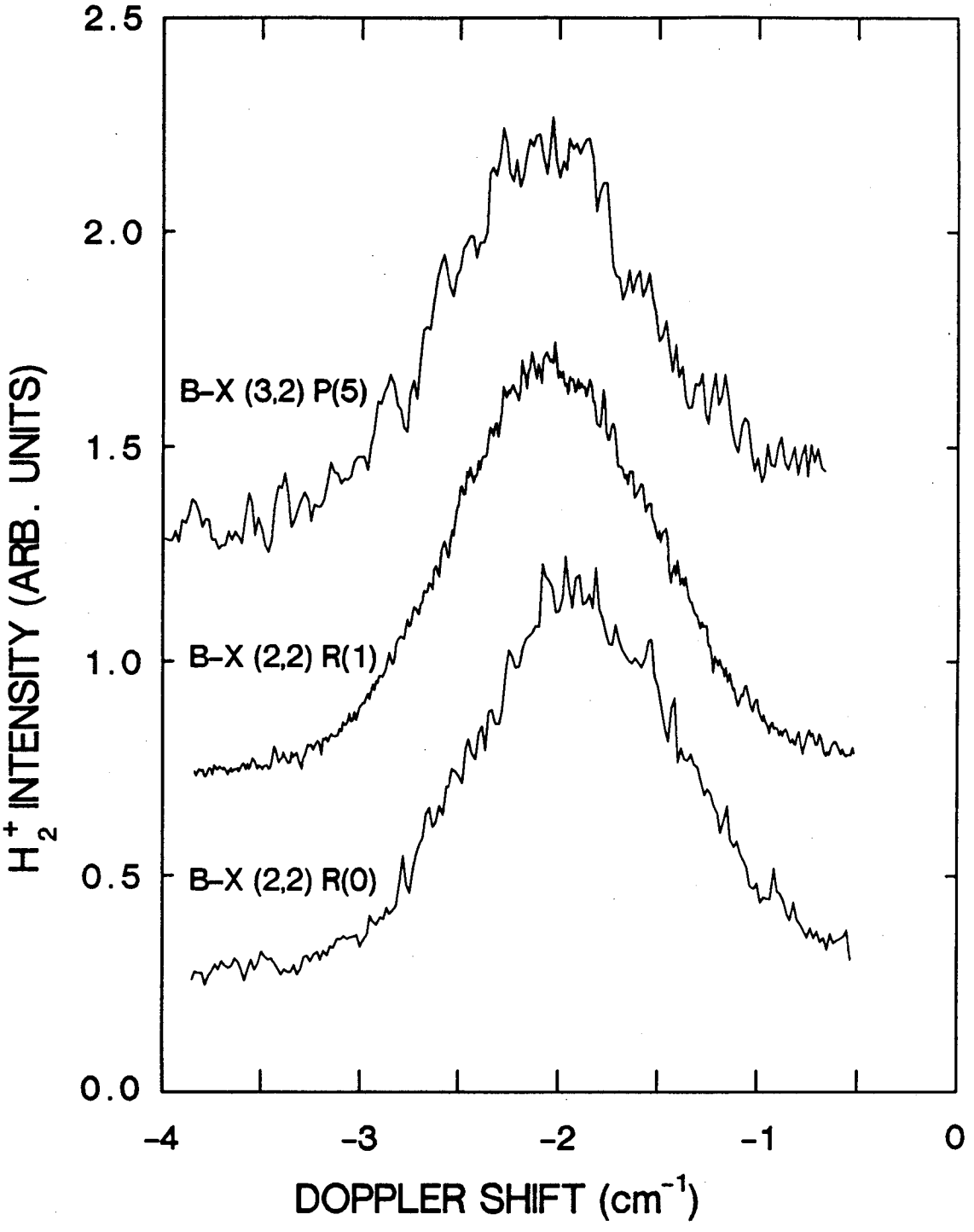

Figure 18. High resolution scans measured under VADS conditions of the red-shifted H_2 peaks for the v"=2 transitions shown in Figure 16. The step size for these scans is 250MHz. The different transitions are indicated.

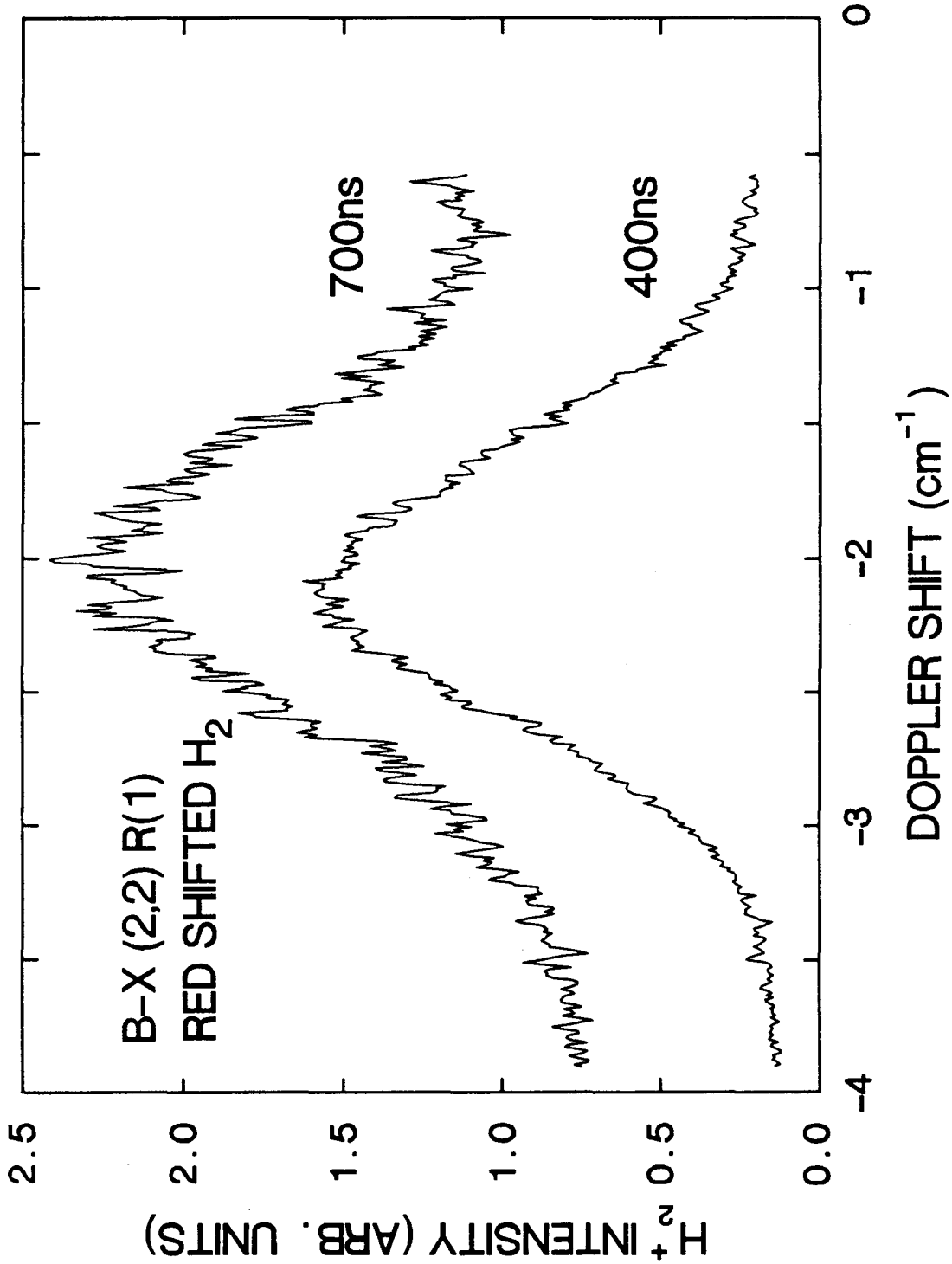

Figure 19. Red side of VADS profile for B-X (2,2) R(1) transition at 400ns (bottom trace) and 700ns (top trace) time delays. The 700ns trace is the average of 10 scans.

acetylene (or vinylidene) molecule as it recoils from the transition state structure. However, it is beyond the scope of this thesis to analyze which quantum states are actually populated in the molecules, other than H_2, that are formed in the dissociation of C_2H_4.

Given the information obtained by the VADS profiles one would expect that the Doppler shift observed for H_2 dissociating from ethylene would be larger than that for H_2 dissociating from 1,1-d_2 ethylene. A comparison of the H_2 Doppler profiles measured from these reactions for the transitions C-X (1,0) Q(5), C-X (2,0) Q(7), B-X (2,1) P(3), and B-X (2,1) R(5) are shown in Figure 20. The v"=0 transitions are shown in Figure 20A and the v"=1 transitions are shown in Figure 20B. As one proceeds to higher energy H_2 quantum states the H_2 translational energy decreases faster for product from the 1,1-d_2 ethylene than from C_2H_4. For the v"=1, J"=5 quantum state the two shifts appear to be equal. This anomaly has not yet been explained. The H_2 translational energies measured from transitions shown in Figure 20 are given in Table III.

Figure 20. Doppler profiles of H_2 product from the dissociation of C_2H_4 (□) and CH_2CD_2 (-) at 193nm. A) (top traces) H_2 C←X (1,0) Q(5) (ν_0=100510.2cm^{-1}) and (bottom traces) H_2 C←X (2,0) Q(7) (ν_0=101865.0cm^{-1}). B) (top traces) H_2 B←X (2,1) R(5) (ν_0=87710.0cm^{-1}) and (bottom traces) H_2 B←X (2,1) P(3) (ν_0=88077.1cm^{-1}).

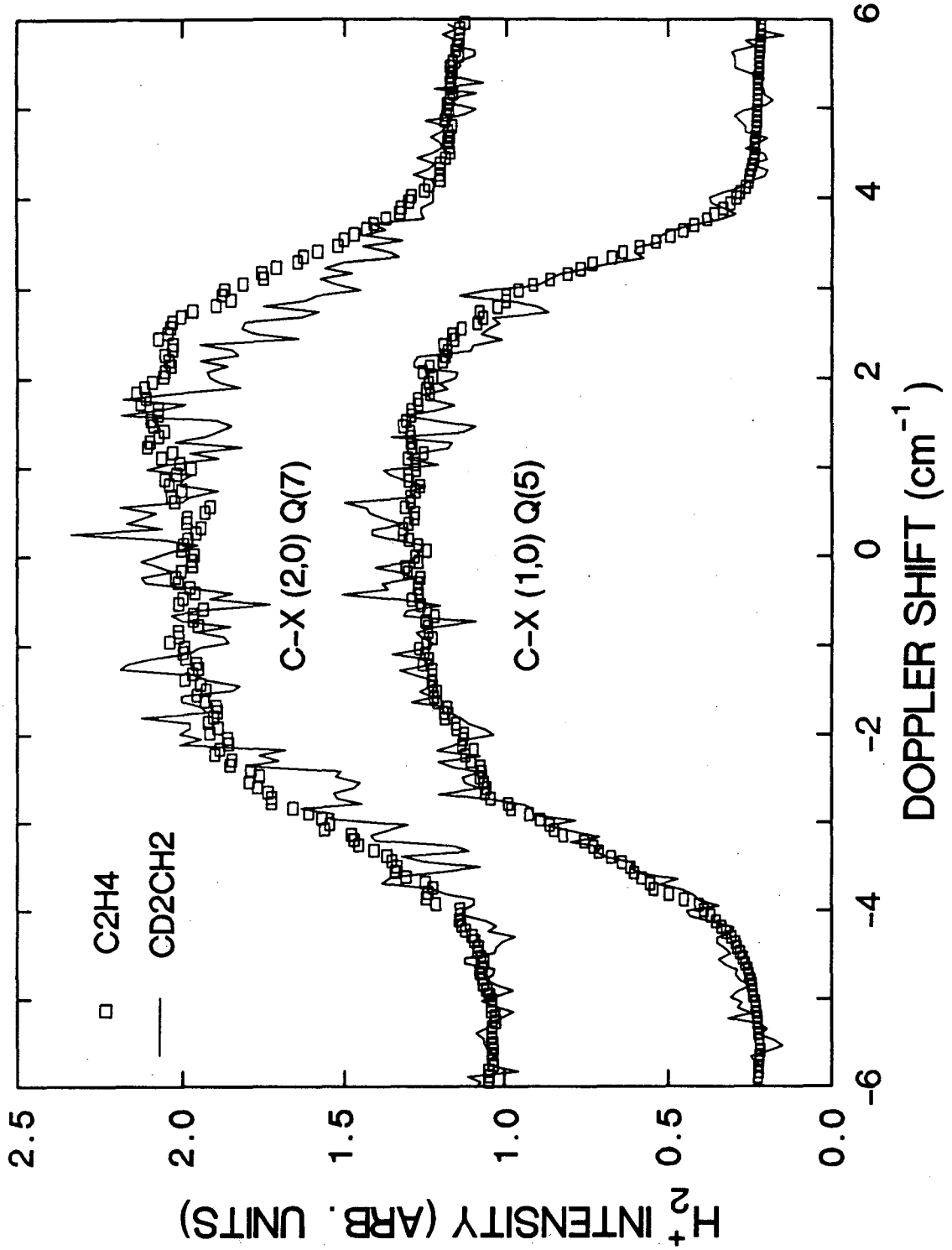
C2H4
CD2CH2
C-X (2,0) Q(7)
C-X (1,0) Q(5)
H_2^+ INTENSITY (ARB. UNITS)
DOPPLER SHIFT (cm^{-1})
2.5
2.0
1.5
1.0
0.5
0.0
-6
-4
-2
0
2
4
6

Figure 20A

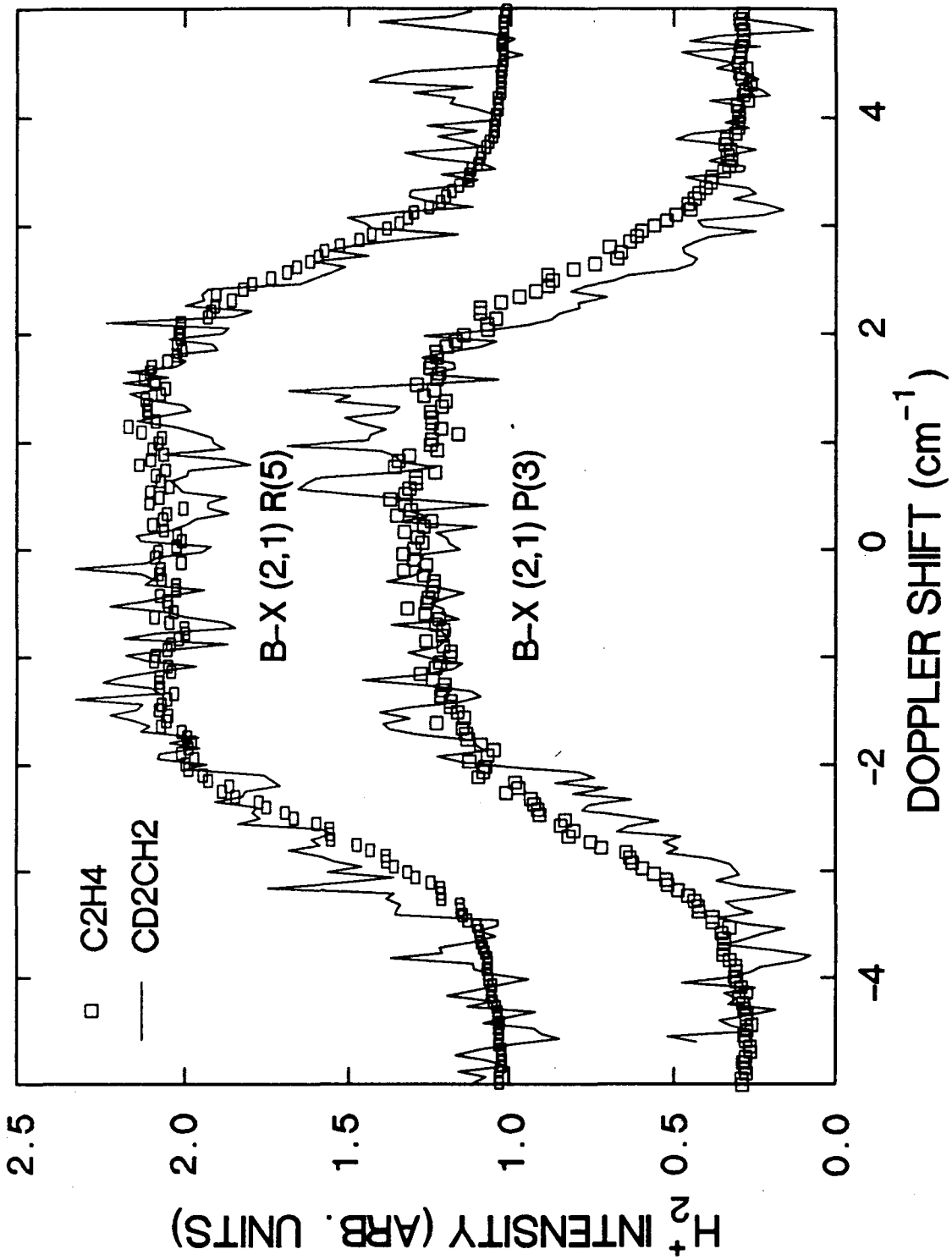
C2H4
CD2CH2
B–X (2,1) R(5)
B–X (2,1) P(3)
H_2^+ INTENSITY (ARB. UNITS)
DOPPLER SHIFT (cm^{-1})
2.5
2.0
1.5
1.0
0.5
0.0
-4
-2
0
2
4

Figure 20B

TABLE III: TRANSLATIONAL ENERGY OF H_2 DISSOCIATED FROM C_2H_4 AND CH_2CD_2 AT 193nm		
H_2 TRANSITION	$E_{tr}(H_2)$ / C_2H_4 (kcal/mole)	$E_{tr}(H_2)$ / CH_2CD_2 (kcal/mole)
C-X (1,0) Q(5)	21.8	22.1
C-X (2,0) Q(7)	21.3	19.3
B-X (2,1) P(3)	21.2	14
B-X (2,1) R(5)	18.7	21

D. D-ATOM ELIMINATION

In addition to probing the H_2 elimination channels in the dissociation of C_2H_4 experiments were performed to gain information on the H atom elimination process in this molecule. Due to the presence of large background H^+ signals it was necessary to measure D atoms eliminated from C_2D_4 photodissociated at 193nm. The elimination dynamics, including electronic states involved and distribution of energy, for both these processes should be very similar. Characterization of the D atom should thus yield information about both the D atom elimination from C_2D_4 and the H atom elimination from C_2H_4.

Scans of the D atom Lyman-alpha transition at both short and long (VADS condition) photolysis/probe time delays are shown in Figure 21. Both scans peak at zero Doppler shift and are fairly narrow compared to the H_2 translational energy. This is consistent with previous measurements of the translational energy distribution in D (and H) atoms

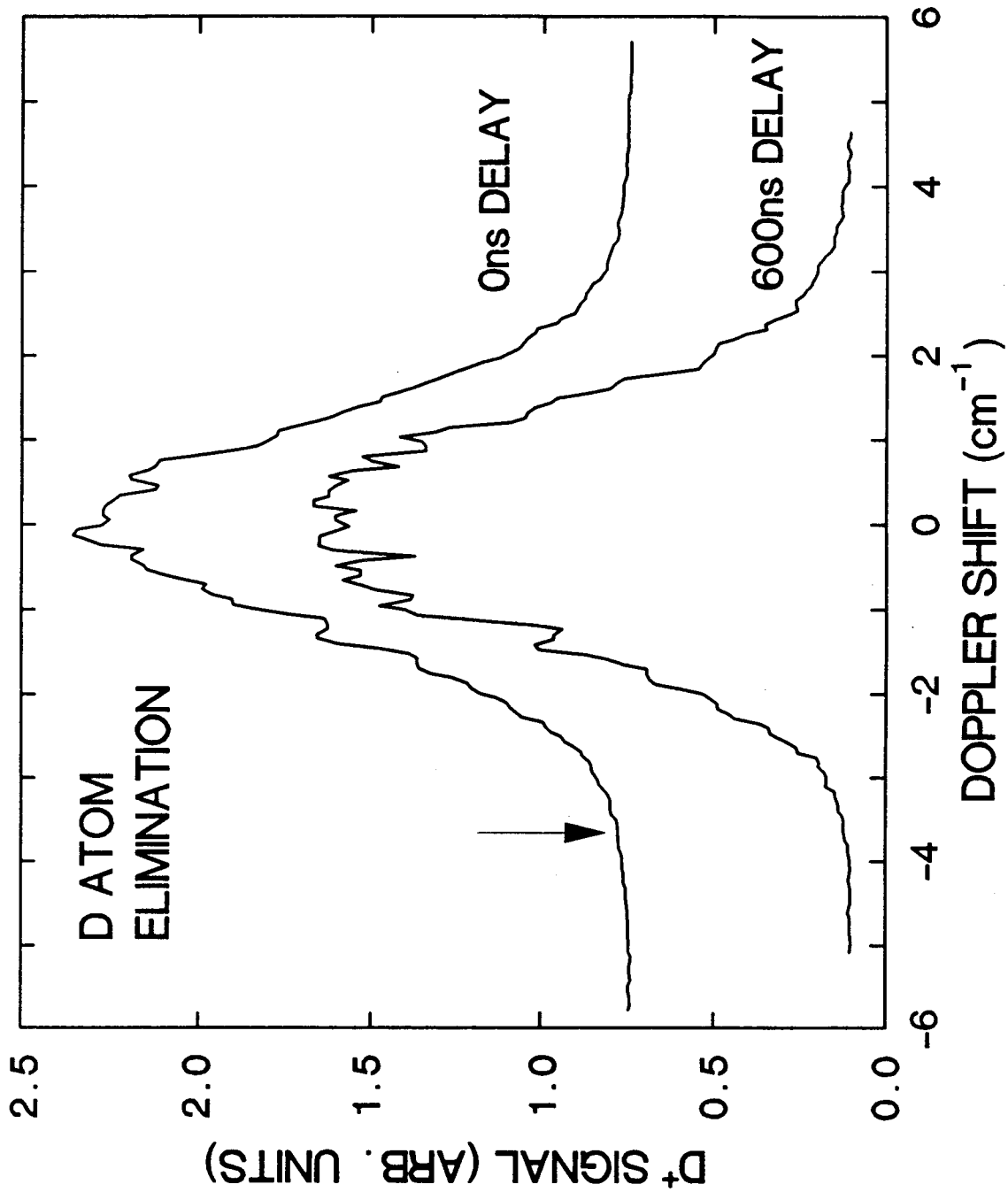

Figure 21. Scans of the Lyman-alpha transition (ν_0=82282.65 cm^{-1}) for D atoms eliminated from C_2D_4 dissociated at 193nm under normal delay (top trace) and VADS conditions (bottom trace). The arrow indicates the maximum kinetic energy expected for a single photon event.

eliminated from C_2D_4 (and C_2H_4).[14,29] The HWHM of the line profiles are 1.43cm^{-1} and 1.57cm^{-1} for the short and long time delay scans respectively which correspond to translational energies of 6.5kcal/mole and 7.8kcal/mole respectively.

The D atom line profile measured under VADS conditions has a broader top and is slightly wider. These features are even more pronounced in view of the $1/v^2$ intensity weighting associated with VADS that was discussed in the previous section. This represents the "true" D atom speed distribution. This distribution is consistent with the short time delay scan. The faster D atoms moving perpendicular to the probe beam will contribute intensity at zero Doppler shift for the 0ns delay scan, giving it a higher peak intensity and a sharper profile. However, these same atoms will not contribute any intensity at zero Doppler shift under VADS conditions.

An attempt was made to measure the maximum translation energy released in order to calculate the C-D bond strength in C_2D_4. D atoms were observed with up to ≈70kcal/mole of translational energy. This would correspond to a C-D bond strength of only ≈78kcal/mole which is well below previously reported values. Clearly these fast D atoms cannot be the result of a single photon event. Photolysis power dependence studies done on the fast D atom component showed a linear response over an order of magnitude of change in

the photolysis energy density. This does not rule out a two photon absorption process, though, as has been previously assumed in other studies of this reaction.[30] If the cross section for absorption of the second photon is much greater than that of the first photon this secondary absorption process can be saturated. If this is the case then power dependence studies will produce a more linear result with the linearity depending on the degree of saturation.

For the case of ethylene, the absorption cross section of the vinyl radical is much greater than that of ethylene.[30,31] It is possible for the vinyl radicals produced in the dissociation of ethylene to absorb a second 193nm photon before eliminating a second D (or H) atom. With this in mind the results shown in Figure 20 must be viewed with caution since the contribution to the Doppler profile from D atoms eliminated from the deuterated vinyl radical is not known.

IV. SUMMARY

The evidence presented in this chapter clearly supports the existence of two distinct channels for the elimination of H_2 from C_2H_4. The existence of these channels, the 1,1 elimination shown in reaction (3) and the 1,2 elimination shown in reaction (4), has been proposed previously and supported by numerous experiments. However, the information

presented here provides the first insight into the differences in the dissociation dynamics of the two processes. This should be of great value to anyone attempting to model the ethylene transition state complex or perform classical trajectory studies on these reactions.

For the 1,1 elimination process the amount of released energy is limited by the heat of formation of the vinylidene biradical. The average translational energy of H_2 from this channel is less than the total average H_2 translation energy observed. The amount of rotational and vibrational energy imparted into the H_2 product from this dissociation pathway is also significantly (≈50%) lower than from the other channel. The critical configuration near the transition state for this reaction should be not unlike that for H_2 elimination from formaldehyde. There is a large difference in the H_2 product's translation energy between these two (C_2H_4 and H_2CO) dissociations. The repulsion felt by the H_2 in the H_2CO transition state must be much greater than that felt by H_2 in the C_2H_4 transition state. This would imply a longer H_2-:C=CH_2 distance than H_2-CO distance at the respective critical configurations.

There is nearly twice as much energy available to H_2 product formed in the 1,2 elimination process. This larger amount of available energy is reflected in the rotational, vibrational, and translational energy of that H_2 product. The higher vibrational energy implies a longer H-H distance

at the critical configuration of the 1,2 elimination reaction than of the 1,1 elimination reaction. This is consistent with a longer distance between the respective H atoms in the ethylene molecule itself. The higher rotational energy for the 1,2 elimination is due to a greater anisotropy in the repulsive potential felt by the two H atoms which form the H_2 molecule at the transition state although some contribution from the larger kinetic energy release for this channel can not be ruled out completely. This is consistent with a critical configuration at the transition state somewhere between a C_2H_4 structure and a CH_3CH structure. Depictions of the molecular configurations in the transition state regions for the two H_2 elimination processes are shown in Figure 22.

Finally, the question of which electronic state potential surface the reaction occurs on is still unanswered. From the amount of released energy during the dissociation process the acetylene product must be formed in its ground electronic state. This is supported by other experiments and theoretical calculations.[26,32] It is known that the H atom elimination process (which accounts for ≈50% of the C_2H_4 dissociated) occurs in the ground electronic state. Is conversion to the ground state fast compared to H_2 elimination in the excited state? The energy available (148kcal/mole) to the C_2H_4 is above calculated potential

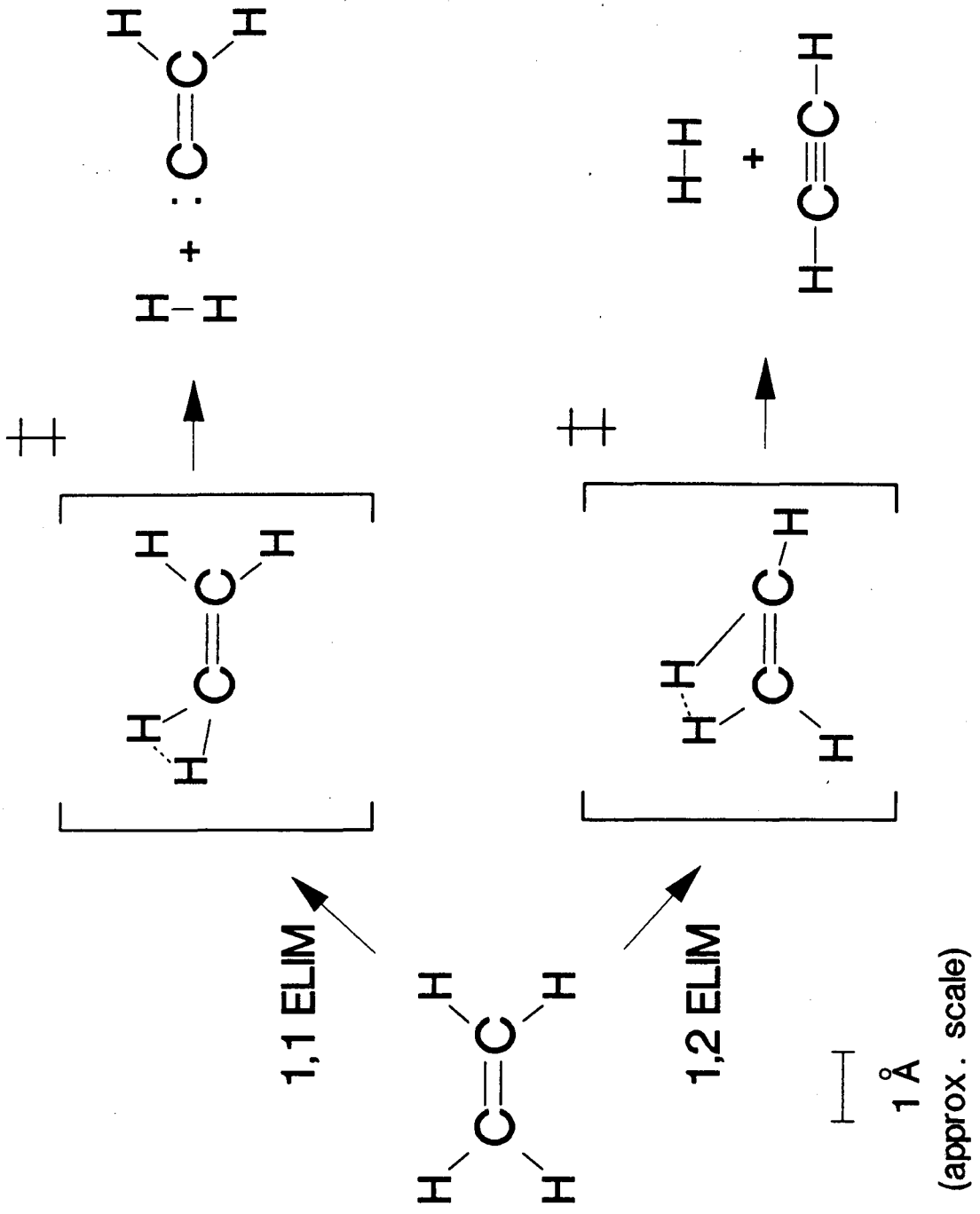

Figure 22. Authors conception of the critical configurations at the transition states of the two channels for H_2 elimination from ethylene. (top trace) 1,1 elimination channel and (bottom trace) 1,2 elimination channel.

energy barrier values for dissociation in both ground and excited electronic states. Clearly the involvement of the ground electronic state for one or both of the H_2 elimination channels cannot be ruled out. Hopefully further theoretical work will provide more insight into this complex question.

REFERENCES

1. P. Ausloos and R. Gorden, Jr., J. Chem. Phys. **36**, 5 (1961).

2. R. Gorden, Jr. and P. Ausloos, J. Res. Nat. Bur. Std. Sec. A **75A**, 141 (1971).

3. A.B. Callear and R. J. Cvetanović, J. Chem. Phys. **24**, 873 (1955).

4. R.A. Bach and D.W.L. Griffiths, J. Chem. Phys. **46**, 4839, (1967).

5. M.C. Sauer, Jr. and L.M. Dorfman, J. Chem. Phys. **35**, 497 (1961).

6. H. Okabe and J.R. McNesby, J. Chem. Phys. **36**, 601 (1961).

7. E. Tschuikow-Roux, J.R. McNesby, W.M. Jackson, and J.L. Faris, J. Phys. Chem. **71**, 1531 (1967).

8. P. Borrel, A Cervenka, and J.W. Turner, J. Chem. Soc. (B), 2293 (1971).

9. H. Hara and I Tanaka, Bull. Chem. Soc. Jpn. **46**, 3012 (1973).

10. H. Hara and I. Tanaka, Bull. Chem. Soc. Jpn. **47**, 1543 (1974).

11. A.H. Laufer, J. Photochem. **27**, 267 (1984).

12. A. Fahr and A.H. Laufer, J. Photochem. **34**, 261 (1986).

13. K.M. Ervin, S. Gronert, S.E. Barlow, M.K. Gilles, A.G. Harrison, V.M. Bierbaum, C.H. DePuy, W.C. Lineberger, and G.B. Ellison, J. Am. Chem. Soc. **112**, 5750, (1990).

14. B. Balko, J. Zhang, and Y.T. Lee (to be published).

15. G.J. Collin, Adv. Photochem. **14**, 135 (1988).

16. E.M. Evleth and A Sevin, J. Am. Chem. Soc. **103**, 7414 (1981).

17. J.D. Goddard, Chem. Phys. Lett. **83**, 312 (1981).

18. E.F. Cromwell, D.-J. Liu, M.J.J. Vrakking, A.H. Kung, and Y.T. Lee, J. Chem. Phys. **92**, 3230 (1990).

19. E.F. Cromwell, A. Stolow, M.J.J. Vrakking, and Y.T. Lee, (to be published).

20. See Chapter III of this thesis.

21. A.J. Merer and R.S. Mulliken, Chem. Rev. **69**, 639 (1969).

22. R. Hilbig and R. Wallenstein, App. Opt. **21**, 913 (1982).

23. D. Proch and T. Trickl, Rev. Sci. Inst. **90**, (1989).

24. R.N. Dixon, J. Chem. Phys. **85**, 1866 (1986).

25. H. Abgrall, F. Launay, E. Roueff, and J.-Y. Roncin, J. Chem. Phys. **87**, 2036 (1987).

26. T.J. Butenhoff, K.L. Carleton, and C.B. Moore, J. Chem. Phys. **92**, 377 (1990).

27. R.J. Sension and B.S. Hudson, J. Chem. Phys. **90**, 1377 (1989).

28. Z. Xu, B. Koplitz, and C. Wittig, J. Chem. Phys. **87**, 1062 (1987).

29. S. Satyapal, G.W. Johnston, R. Bersohn, and I. Oref, J. Chem. Phys. **93**, 6398 (1990).

30. H.E. Hunziker, H. Kneppe, A.D. McLean, P. Siegbahn, and H.R. Wendt, Can. J. Chem. **61**, 993 (1983).

31. A. Fahr and A. Laufer, J. Phys. Chem. **92**, 7229 (1988).

32. A.W. Wodtke, E.J. Hintsa, J. Somorjai, and Y.T. Lee, Israel J. Chem. **29**, 383 (1989).

LAWRENCE BERKELEY LABORATORY
UNIVERSITY OF CALIFORNIA
INFORMATION RESOURCES DEPARTMENT
BERKELEY, CALIFORNIA 94720